OPTICAL SECTIONING MICROSCOPY WITH SPATIAL MODULATED EXCITATION LASER

A Dissertation
Presented to
The Academic Faculty

By

Hao Xie

In Partial Fulfillment
of the Requirements for the Degree
Doctor of Philosophy in the
School of Engineering

Georgia Institute of Technology
Emory University

May 2017

OPTICAL SECTIONING MICROSCOPY WITH SPATIAL MODULATED EXCITATION LASER

Approved by:

Dr. Peng Xi, Advisor
School of Engineering
Peking University

Dr. Philip.J Santangelo, Co-advisor
Dept of Biomedical Engineering
Georgia Institute of Technology and Emory University

Dr. Tianyu Xie
School of Engineering
Peking University

Dr. Changhui Li
School of Engineering
Peking University

Dr. Juntao Gao
Dpartment of Automation
Tsinghua University

Date Approved: November 18, 2016

This dissertation is dedicated to my parents.

ACKNOWLEDGEMENTS

I feel so lucky to have the opportunity to work in Dr. Peng Xi's and Philip J. Santangelo's labs. Dr. Peng Xi always encouraged me to try something new. Dr. Philips J. Santangelo inspired me to set up the first optical system by myself, and gave me the chance to learn cell cultural and staining.

I am gratefully to Dr. Tianyu Xie, Dr. changthui Li and Dr. Juntao Gao for serving on my oral committee.

I would like to acknowledge every member in PKU lab: Yujia Liu, Tong Peng, Yichen Ding, Xusan Yang, Hao Zhang, Amit Lal, Zhiping Zeng, Miaoyan Wang and Kun Zhao, from whom I learned a lot. I would like to thank members in GT lab: Eric Ealonas, Daryll Vanover, Jonathan Kirschman, Sushma Bhosle, Chiara Zurla and Emmeline Blanchard. Thanks to Martin Jacobson and Andrew Shaw. Marty taught me so much in machine shop. Andrew contributed his expertise to help me on the microscope systems.

In addition, I would like to thank Shangguo Zhu and Hao Yan, who helped me a lot when I was new in Atlanta. Thanks to all my friends outside the lab, who make my graduate years enjoyable.

Finally, I would like to thank my family. My parents have made great sacrifices for me. This dissertation is dedicated to them.

TABLE OF CONTENTS

LIST OF TABLES

LIST OF FIGURES

SUMMARY

Optical microscopy is one of the most widely used tools in biomedical researches. However, in the observation of thick biological samples, conventional optical microscopes suffer from background from out-of-focus structures. For example, in conventional epi-fluorescence microscopy, the whole sample is illuminated and the out-of-focus light contributes a strong background to the image, thus obscuring the in-focus details. Confocal microscopy and light sheet microscopy are the popular techniques for sectioning imaging. In this dissertation, excitation patterns are designed to improve optical sectioning capacity for point scanning and volumetric imaging systems.

In the first part of dissertation we improved the point scanning microscopy with excitation laser modulations. We used a mirror to reflect the incident laser to produce the interference in the focal region. It is found both the sectioning capacity and peak intensity of excitation and depletion beam in STED are improved and the signal to noise ratio is enhanced. First we used diffraction theory to simulate the intensity distribution in focal region. Then we proved the improvement of sectioning capacity with a nano-particle phantom sample. We have grown Vero cells on a silicon dioxide layer above the mirror, and applied this method to those samples on conventional spinning disk and two-photon microscopy. Further, we developed spectral methods to move the interference lay inside cell, making 3D observation possible. Finally, we demonstrate the increase in intensity could be used to reduce the laser power requirement in STED microscopy.

This dissertation also developed a sectioning point scanning based phase contrast microscopy: Schlieren confocal microscopy. We found incident laser refracts due to the local gradient of sample, and the detected fluorescence intensity could quantitatively reflect the local gradient of sample. We built the model and applied it to biological measurements. We found this method could obtain similar effect as the Differential interference microscopy, keeps the optical sectioning capacity of confocal, and is fully compatible with confocal.

In the third part, this dissertation applied excitation modulation to inhibit the background in light field microscopy. light field microscopy sacrifices spatial resolution for acquisition speed, and is preferable in the observation of fast biological phenomenon. However, light field reconstruction problem is ill-defined and it would result in strong background. We combined light sheet illumination with micro lens array coupled detection. It is demonstrated this method could significantly reduce the background in conventional light field microscopy and faster speed compared to light sheet. It could be applied in samples with high label densities.

In conclusion, we applied spatial modulated excitation to point scanning and volume imaging systems, and improved their sectioning ability. Our research could provide promising tools for in-vivo observations in large specimens.

CHAPTER 1
INTRODUCTION

In this chapter, we first briefly introduce the concept of optical microscopy and the background problem in conventional epi-fluorescence microscopy. It is aimed primarily at readers who are not familiar with this field. Then we have a short review on existing 3D optical sectioning technologies. In the last section, we show the roadmap of this dissertation.

1.1 Optical microscopy

Microscopy is an invaluable tool in scientific research. In today's research, most major scientific discoveries in material and biological science are relevant to the advances in microscopy: optical microscopy [1], transmission electron microscopy [2, 3, 4, 5, 6], scanning tunneling microscopy [7, 8, 9, 10], atomic force microscopy [11, 12, 13], and so on. Optical microscopy is popular among biologists because it is fast and no ionizing to living tissues.

In optical imaging microscopy, the scattered optical rays in some directions cannot be captured, leading to the "missing cone of data" problem [14]. Consequently, the 3D structure of the sample could not be fully restored from data. In the next section, we will use a geometrical optics model in epi-fluorescence microscopy to give a straightforward illustration from a different perspective.

1.2 Background in wide-field fluorescence microscopy

Fluorescence microscopy is a special optical microscopy, which utilizes the fluorescence from the observed specimen . The idea of fluorescence microscopy originated in 1911 [15] and the first epi-fluorescence microscope prototype was designed in 1929 [16, 17]. The

source of fluorescence could be the auto-fluorescence of sample [18, 19, 20], immunofluorescence [21, 22, 23] or fluorescent proteins [24, 25, 26, 27]. Although the whole sample is illuminated, only the regions with fluorophores could emit fluorescence. With longer wavelength than its excitation laser, fluorescence could be separated with a high-pass filter. As a result, epi-fluorescence images have dark backgrounds and the detected fluorescence is expected to quantitatively reflect the number of fluorescent molecules in the detected region.

We can define signal to background ratio by $\mathrm{SBR} = \mathrm{singal}/(\mathrm{signal} + \mathrm{background})$. To understand the role of SBR, we need to look at the image acquisition process of an epi-fluorescence microscopy. First, electrons in fluorophores are excited and will stay on the excitation states for some time, then fall back to the ground state and emit fluorescence. Then the image detector could detect the fluorescence photons and each photon has the chance to excite some electrons. A Poisson process could describe these random processes. An amplifier will amplify the electrons, with heat noise induced. Finally, the analog signal will be converted into digital output, so ADC readout noise is added [28, 29, 30].

The image process could be described by equation $I(x, y, z) = S(x, y, z) \bigotimes h(x, y, z) + b(x, y, z) + e(x, y, z)$. Here $I(x, y, z)$ is the image, $S(x, y, z)$ is the sample fluorophore distribution, $h(x, y, z)$ is the point spread function of system, $\bigotimes$ is the convolution operator defined by $f(x) \bigotimes g(x) = \int f(x')g(x - x')dx'$, and $e(x, y, z)$ is the noise. Our task is to restore as much information of $S(x)$ as possible from the measured $I(x, y, z)$, $b(x, y, z)$ and $h(x, y, z)$. Here we have assumed the system is spatially invariant. The noise term of our system $e(x, y, z)$ could be further divided into signal independent noise (additive noise) and signal dependent noise (multiplicative noise). The latter, including the Poisson noise of photon detection process, increases with the square root of the overall signal level. When the background is strong, the background induced noise increases so that we are not able to extract the signal from it.

Here we use a simple model to show the divergence of background in epi-fluorescence

microscopes. For more rigid wave optics analysis, see Reference [14]. We assume our samples consist of nanobeads, and the distribution of beads is uniform in the medium. We also assume the refractive index of the media is the same as air for simplicity. Then we are able to calculate the signal we detected at position (x, y, z):

$$\text{signal}(x, y, z) = K \int \rho(x', y', z') h(x - x', y - y', z - z') dV \tag{1.1}$$

This integration is taken over the 3D object space. For an ideal imaging system we expect the intensity measured could reflect the fluorophore density at coordination (x, y, z)

$$\text{signal}(x, y, z) = K \int_{\Omega} \rho(x', y', z') h(x - x', y - y', z - z') d\text{V} \approx K\rho(x, y, z)\Delta V \tag{1.2}$$

Here Ω represents the detection region and ΔV is the volume of PSF.

Next, we need to calculate the background. The energy taken by an optical ray at angle θ is $I = I(x, y, z)\cos^4\theta$, where θ is the angle between the ray and CCD plane [31]. We assume NA of this system is not that large, so $NA = \sin\alpha \ll 1$ and the term $\cos\theta$ could be approximated as 1. If we divide the media into slices along z, we can calculate the irradiance of each layer from z to $z + \Delta z$, as shown in Figure 1.1(a)

$$\Delta I = K \frac{d^2}{4\pi z^2} \rho(x, y, z) \Delta V \tag{1.3}$$

Integrate the whole section and notice the fluorophore is uniformly distributed,

$$\mathrm{d}I(z) = K \frac{d^2}{4\pi z^2} \rho(x, y, z) * 2\pi z * \frac{\alpha^2}{2} z \mathrm{d}z = K \frac{\rho\alpha^2}{4} \mathrm{d}z \tag{1.4}$$

So $\mathrm{d}I(z)/\mathrm{d}z = K\rho\alpha^2/4$ is a constant for all layers. Here we see the problem: If we integrate the above equation over the whole space, the background intensity $I = \int \frac{\mathrm{d}I}{\mathrm{d}z} \mathrm{d}z$ will go to infinity, and it indicates a very strong background, just similar to the Olbers Paradox

in astronomy [32]. As a result, in conventional epi-fluorescence microscopy, images will be degraded severely by the out-of-focus light and information from the focal plane would be hard to restore.

Let us analyze this result. Taking a shell with radius r from the imaging point. The intensity of each shell is inversely proportional to the radius square, where the volume of the shell is proportional to the radius square. We know $I(r) = \int f(r)\mathrm{d}r$ will converge at $x = \infty$ if $f(r)$ has a scaling factor $1/r^2$. This is the case of confocal, which could be modeled in Figure 1.1(b). An excitation factor is added to make the integration convergent:

$$dI(z) = K\frac{d^2}{4\pi z^4}\rho(x,y,z) * 2\pi z * \frac{\alpha^2}{2}z\mathrm{d}z = K\frac{\rho\alpha^2}{4z^2}\mathrm{d}z \tag{1.5}$$

If we integrate this expression from d_0/α to ∞ again, background term converges. This mechanism also applies to multi-photon microscopy.

Another solution is to use selective axial illumination. Total internal reflection microscopy excites the layer with a thickness of $\sim$100 nm on the boundary of liquid and glass [33]. The sectioning capacity of TIRF is extremely high, but it could only image one layer on the glass surface. On the other hand, light sheet microscopy uses another objective to illuminate one layer in the sample from the side. In this case,

$$\mathrm{d}I(z) = \frac{Kd_0^2\rho}{4}\mathrm{sinc}^2(\mathrm{z/t})\mathrm{d}z \tag{1.6}$$

Where t is the thickness of the light sheet. Using a cylindrical lens we can focus almost all the energy on the focal plane.

Here is a simple experimental validation of our analysis, as shown in Figure 1.2. We used a single layer of fluorophore to show the average intensity of each image does not change with its axial position. We diluted Cy 5 (1:1000) into PBS and transferred 10 µl on a slide. We covered the solution with a piece of cover glass, stored it in darkness for days until it was dried. Then we sealed it with nail polish and took it to a Nikon Ti-E microscope.

First, we observed it under 40X/0.95 objective. By moving the sample axially, we could estimate the thickness of this fluorophore layer is less than $10\,\mu\mathrm{m}$, as shown in Figure 1.3. Then we used 10X/0.45 objective to measure the average intensity along z. The z resolution of this objective is $d = 2\lambda/NA^2 = 6\ \mu\mathrm{m}$. However, when we scanned along the z-axis, we found the average image average remains constant from $z = 0$ to $z = 1000\,\mu\mathrm{m}$. This indicates fluorophores from different layers contribute equally to the intensity on the image plane. Consequently, epi-fluorescence microscopy has poor performance in thick samples. We further show that under 20X/0.6 and 40X/0.95 objectives, the intensity still remains constant in a range of $800\,\mu\mathrm{m}$ and $1600\,\mu\mathrm{m}$, respectively, as shown in Figure 1.4

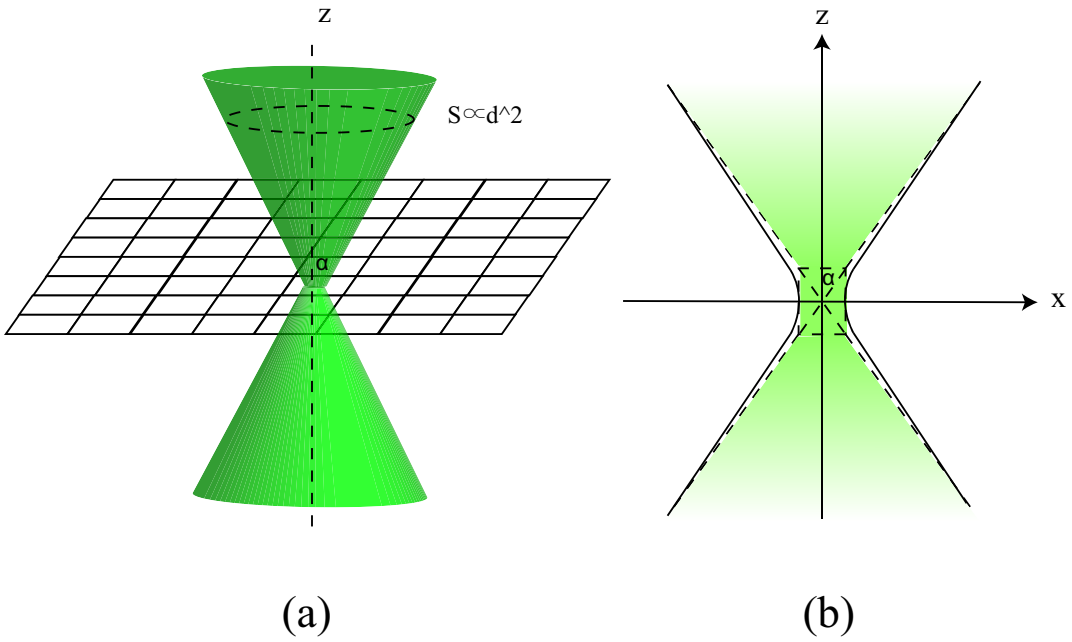

Figure 1.1: (a) Light cone detected by one pixel on the CCD. (b) A cross section of (a) in the XZ-plane.

1.3 Review of current 3D sectioning microscopy

1.3.1 Deconvolution microscopy

Deconvolution microscopy is often used in fluorescence microscopy to remove the out-out-focus background [34, 35, 36, 37, 38]. As described before, in an epi-fluorescence

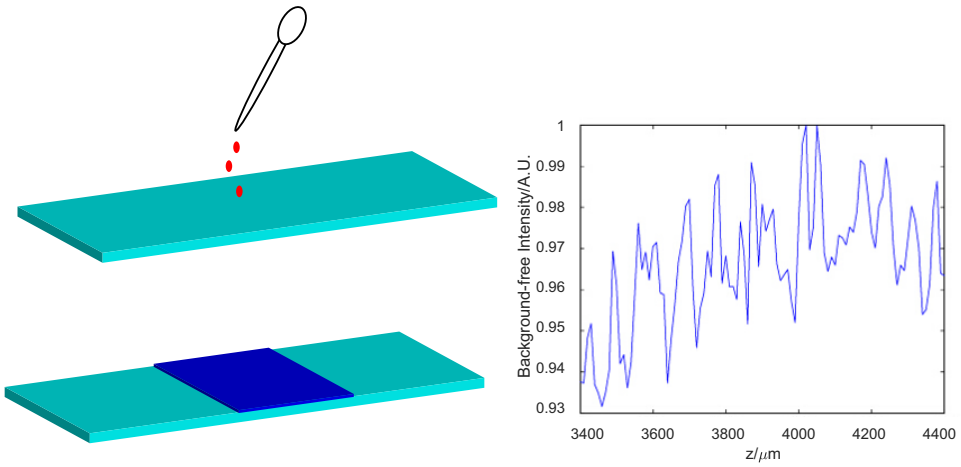

(a) (b)

Figure 1.2: (a) Preparing the single fluorophore layer specimen. We diluted Cy 5 (1:1000) into PBS and transferred 10 µl on a slide. We covered the solution with a piece of cover glass, stored it in darkness for days until it is dried. Then we sealed it with nail polish and took it to a Nikon Ti-E microscope. (b) Measuring the background change with distance under a 10X/0.45 objective.

microscope, out-of-focus stacks are blurred, but they still contribute a strong background because they are also detected by the sensor. The imaging process could be described as $I = O \bigotimes H + B + N$, where I is the detected image, O is the original image, H is the 3D point spread function of the optical system, B is the offset from the image background and the dark current from the detector, and N is the noise. Detector shot noise is a major source of noise, and its intensity is proportional to the square of signal level [39].

An intuitive way to remove the background is to solve the reverse problem in the Fourier domain $O = H^T I / H^T H$. In practice, a Wiener filter is often used to remove the ill-condition of the reverse problem with a kernel $O(u, v, \omega) = \frac{H^*(u,v,\omega)}{|H(u.v.\omega)|^2 + K} I(u, v, \omega)$, where K is the noise power spectra [40]. This method is fast with reasonable accuracy and also works in problems without nonnegative constraint.

Statistical algorithms take the noise distribution into account. For example, the maximum likelihood estimation method uses the image with maximum likelihood to estimate the original object. A log-likelihood function is calculated and optimized with it-

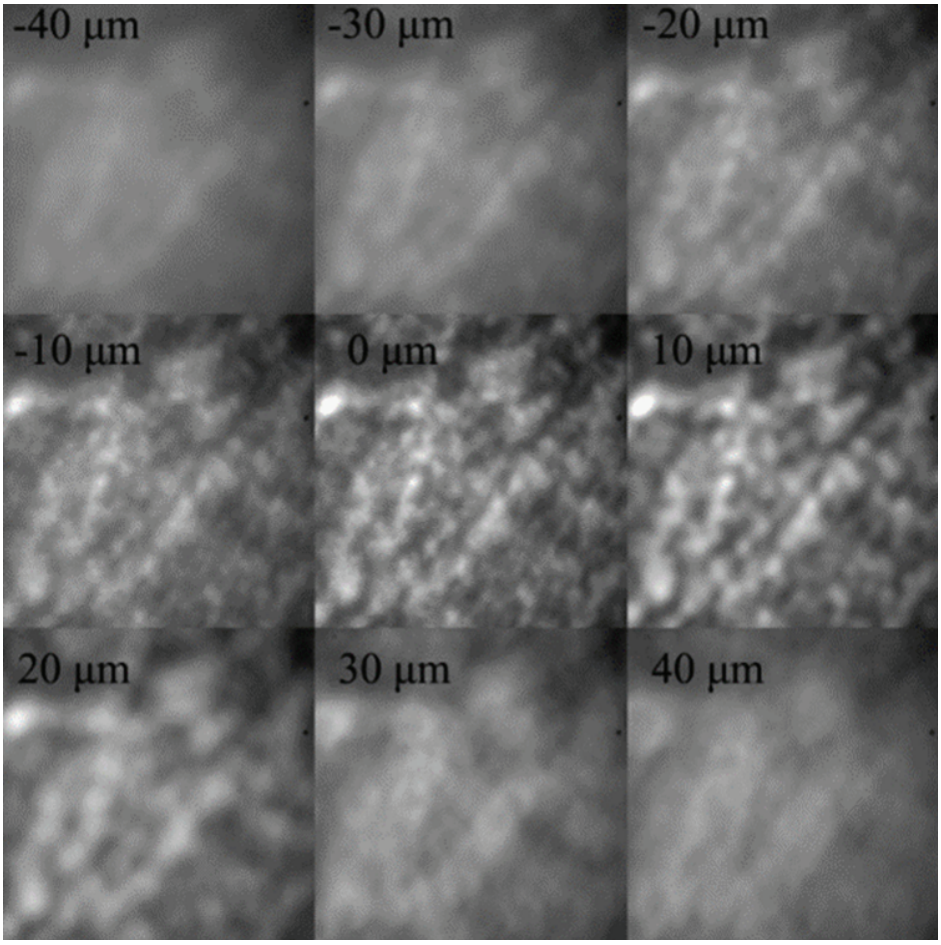

Figure 1.3: Fluorophore layer under a 40X/0.95 objective.

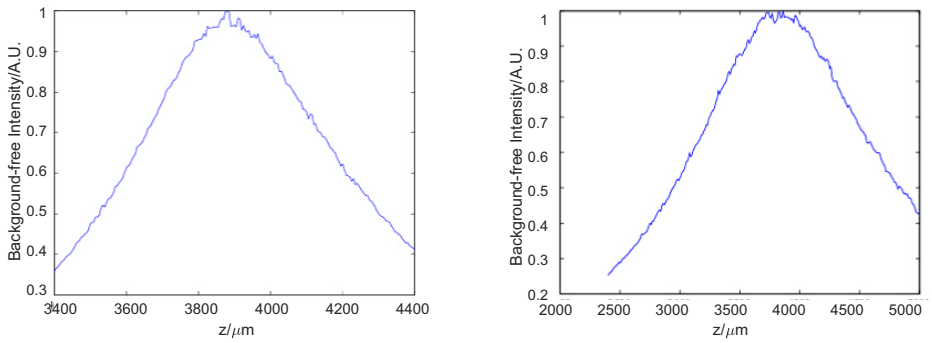

(a) (b)

Figure 1.4: Detected fluorophore layer intensity changes with its axial position. (a) FWHM under a 40X objective is about $800\,\mu\mathrm{m}$. (b) FWHM under a 20X objective is about $1600\,\mu\mathrm{m}$.

erations [41]. A penalty function is often added to ensure the convergence of problem.

Constrained iterative algorithms use the constraint of nonnegative intensity of each pixel. An initial guess of the object intensity should be provided. The value of each pixel is updated from the image formation equation in each iteration, and negative values are set to zero. Jansson Van-Cittert algorithm [42, 43] and Gold algorithm [44] are two typical ways to update the object function in each iteration.

In Blind deconvolution algorithms, it is assumed that both the object distribution and PSF are unknown and they use MLE estimation to update both. An initial guess of the object and PSF function must be provided. First, the object function is updated from PSF function, and then the PSF function is updated from the new object function. This process is repeated interactively until a stop criterion is satisfied [45, 46, 47]. Through actual system point spread function is not required in Blind deconvolution algorithms, they have the limitation of unstable and slow divergence.

There are also 2D deconvolution algorithms. For example, a variant of the nearest neighbor method uses the 2D image itself as an estimation of the neighbor stacks [14]. By iteration, contrast of 2D images could be enhanced. These algorithms have fast speed but at the cost of efficiency.

Deconvolution microscopy has better performance for samples with low fluorescence density. Several factors limit its wider application: first, an actual shift-invariant point spread function can hardly be measured [48]. Second, artifacts may be induced by the ill-conditional nature of problems. So deconvolution microscopy is used as an economical alternative to confocal microscopy.

1.3.2 Structured illumination microscopy

Structured illumination microscopy (SIM) could enhance the resolution by a factor of 2 [49, 50]. It needs low illumination intensity, is compatible with live cell imaging and does not require any special sample preparation. Further, the imaging speed is fast enough to

record the dynamic processes inside cells. As a result, SIM is widely used in biological researches [51, 52, 53, 54, 55]. 3D structured illumination microscopy also has sectioning capacity.

In structured illumination microscopy, laser incidents through a grating before it illuminates on the sample. Only +1 and -1 order diffraction light passes the objective, so this two coherent beams will form a pattern as shown in Figure 1.6. The imaging process could be written as [56, 57]

$$D(x) = Em(x) \bigotimes P(x) \tag{1.7}$$

Where $D(x)$ is the detected intensity, $P(x)$ is the PSF of microscope and $Em(x)$ is the fluorescence emission distribution:

$$Em(x) = I(x)S(x) \tag{1.8}$$

where $I(x)$ is the illumination intensity distribution, $S(x)$ is the fluorophore density distribution. In the frequency domain this equation is

$$\tilde{D}(k) = (\tilde{I} \bigotimes \tilde{S})(k)\mathrm{OTF}(k) \tag{1.9}$$

where $\tilde{D}(k)$, $\tilde{I}(k)$ and $\tilde{S}(k)$ are the Fourier Transforms of $D(k)$ $I(x)$ and $s(x)$, and $\mathrm{OTF}(k)$ is the system's optical transmission function. In linear SIM, illumination results from the $+1$ and -1 order laser interference

$$I(x) = \frac{I_0}{2}(1 - \cos(2\pi k_0 x + \phi)) \tag{1.10}$$

Then the detected image could be written in the Fourier domain as

$$\tilde{D}(k) = \frac{I_0}{2}[\tilde{S}(k) - \frac{1}{2}\tilde{S}(k - k_0)e^{-i\phi} - \frac{1}{2}\tilde{S}(k + k_0)e^{+i\phi}] \tag{1.11}$$

By changing 3 different ϕ, all three terms on the right could be separated, each corresponding to a circle in the frequency domain as shown in Figure 1.5. Then with 3 rotations, isotropic frequency expansion could be achieved. Mechanism of 3D SIM is similar, but the 0th order diffraction pattern after grating should also be kept [58]. The illumination pattern of 3D SIM is drawn in Figure 1.6(b).

Later nonlinear SIM is developed to further improve the resolution [59]. The mechanism of nonlinear SIM is similar with STED introduced later in this chapter. The problem of SIM lies in its deconvolution algorithm. When the background canceled out in the calculation, their noise terms will accumulate and result in artifacts in reconstruction [60].

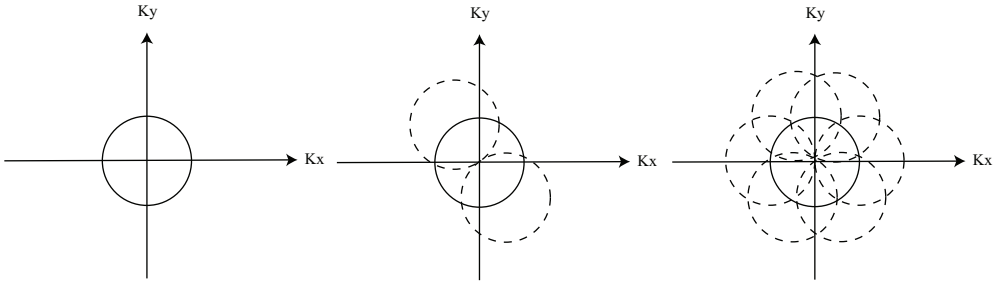

Figure 1.5: 2D SIM reconstruction in the frequency domain. Left: conventional epifluorescence microscopy only resolves frequency in a central circle. Middle: three frames in structure illumination resolve frequency in three circles. Right: after rotation of illumination patterns, an isotropic frequency pattern is obtained.

1.3.3 Confocal microscopy and two-photon microscopy

Confocal microscopy [61] uses a pinhole in front of the detector, and the pinhole is conjugate to the detection point [62]. Usually, laser is used to focus on this point [63], and the system point spread function is the product of the excitation and detection point spread functions. Theoretically, its lateral resolution is $\sqrt{2}$ times better than wide-field microscopy, but to improve the signal level, we often sacrifice this enhancement in resolution. Confocal is chosen for its excellent sectioning capacity [64, 65, 66, 67, 68].

Image Scanning Microscopy (ISM) [69, 70] is an improved version of conventional

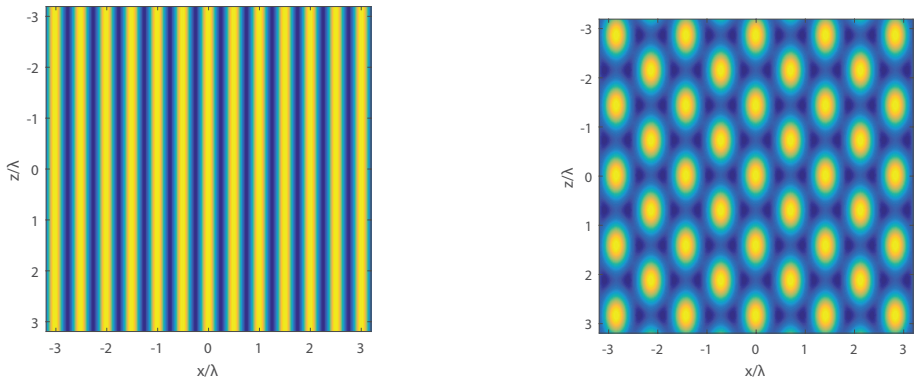

(a) (b)

Figure 1.6: SIM reconstruction patterns. (a) 2D SIM. (b) 3D SIM.

confocal microscopy. ISM replaces the PMT pinhole with a CCD and by deconvolution it could improve the resolution by a factor of 2. The image detected by detector at CCD pixel s and at scanning point r is

$$I(r,s) = \int \mathrm{d}r' U(r - r' + s) E(r - r') c(r') \tag{1.12}$$

Where U(r) is the wide field detection PSF, $E(r)$ is the excitation intensity density, and $c(r)$ is the spatial density of fluorescence emitters. The rearrangement of pixel step replaces $s = r_d$ and $r = r_r - \alpha r_d$, and integrate over r_d

$$I_{eff}(r_r) = \iint \mathrm{dr'dr_d U(r_r - (\alpha - 1)r_d - r')E(r_r - \alpha r_d - r')c(r')} \tag{1.13}$$

When $\alpha = 0$, this intensity gives a wide field image and when $\alpha = 1$ this result gives a no-confocal scanning image. Image scanning microscopy requires $\alpha = 0.5$.

That is $I_{eff}(r_r) = c(r_r) \bigotimes U_{eff}(r_r)$ where

$$U_{eff}(r_r) = \int dr_d U(r_r + \frac{1}{2} r_d) E(r_r - \frac{1}{2} r_d) \tag{1.14}$$

Alternatively,

$$\tilde{U}_{eff}(m) = \tilde{U}(\frac{m}{2})\tilde{E}(\frac{m}{2}) \tag{1.15}$$

Finally, the spectrum of the effective point spread function is broadened by a factor of 2, which is similar to the structured illumination. A Wiener filter could be used for deconvolution [40] $\tilde{c}(k) = \tilde{w}(k)\tilde{I}_{eff}(k)$ where

$$\tilde{w}(k) = \frac{U(\frac{k}{2})}{\epsilon + U(\frac{k}{2})E(\frac{k}{2})} \tag{1.16}$$

Here ϵ is a small constant, and a simplified assumption is made that the detection PSF and the EID have the same support in the Fourier domain.

The recent development of image scanning microscopy includes spinning disk image scanning microscopy and two-photon image scanning microscopy. In spinning disk image scanning microscopy, multiple focal points are scanned in parallel with the help of a microlens array, so the image speed could be significantly enhanced [71]. Two-photon image scanning microscopy uses longer wavelength excitation for better sectioning capacity [72].

1.3.4 Stimulated emission depletion microscopy

Stimulated emission depletion microscopy could be thought as an improved version of confocal microscopy. In confocal, only a small region around the scanning point is illuminated so that the excitation area could be confined to a diffraction-limited volume. STED could further reduce this volume by inducing a stimulated emission process with a second depletion beam. Electrons on the excitation state will jump back to the ground state if they are illuminated by a second light with a longer wavelength, and the remaining excited electrons numbers would be roughly inversely proportional to the depletion intensity. As a result, if the scan point has zero depletion intensity and the adjacent area has non-zero depletion intensity, the point spread function would be sharper.

In 1994 Hell et al. assumed the depletion beam is Gaussian, and derived a square root

law $d = d_0/\sqrt{1 + I/I_{dep}}$ [73]. In 1999 he used a $0 - 2\pi$ phase plate to validate his idea in experiment [74, 75]. 3D STED could also be realized by adding another phase plate [76, 77]. Ground State Depletion(GSD) [78], another derivation of STED, uses the depletion of the ground state and sometimes they are generalized as Reversible Saturable/Switchable Optical Transitions (RESOLFT) [79]. With this kind of techniques, 20 nm lateral resolution has been achieved in biological samples.

The first roadblock of further increasing the resolution is re-excitation of depletion beam. The second is high-intensity laser result in quick bleaching of sample [80, 81]. Finally, imaging speed is limited in point-scanning schemes.

1.3.5 Selective plane illumination microscopy

Selective plane illumination microscopy/Light sheet microscopy has the advantages of deeper penetration depth and less photobleaching. It has been applied to various samples, ranging from RNA polymerase to zebra embryos [82, 83, 84]. The recent development of light sheet microscopy includes Selective Plane Illumination Microscopy (SPIM) [84], Individual Molecule Localization-Selective Plane Illumination Microscopy(IML-SPIM) [85], inverted SPIM (iSPIM), Reflected Light Sheet Microscopy and Prism Coupled Light Sheet Microscopy [86]. Based on these setups, other microscopy techniques, like localization microscopy [85], structural illumination [87], two-photon [88] and Bayesian microscopy [89], Bessel beam and Airy beam [90] are implanted to improve the axial and lateral resolution. Among those setups, SPIM uses a sample chamber with two long-working-distance objectives. iSPIM uses the microscope stage to mount the sample, and two additional objectives are added for the excitation and detection light path. Reflected Light Sheet Microscopy and Prism Coupled Light Sheet Microscopy use a reflecting AFM tip or a prism to form a light sheet for higher NA objectives with short working distances.

There are two classes of light sheet microscopy: the first one uses a static light sheet spread over the whole field of view, and the second uses a thin light beam to scan the

entire focal plane. The static light sheet can use a single cylindrical lens, or a conjugated cylindrical lens and objective pair. The static light sheet is simple to set up because there are no movement parts in optical elements; however, it is not so flexible as a line-scanned light sheet. A line-scanned light sheet has higher peak intensity so that it might induce more photobleaching. However, with the help of two-photo excitation, it has superior penetration and low damage to the sample. Structured illumination could also be combined with a line-scanned light sheet to improve the 3D resolution. Further, Bessel beam and Airy beam could be used to extend the length of the line-scanned light sheet.

The biggest problem of light sheet microscopy is the trade-off between light sheet thickness and length. The field of view decreased dramatically with the reduction of the light sheet thickness. Second, reflective index mismatch and scattering would impair the light sheet shape in large samples. Third, high numerical aperture objective lenses usually have short working distance and large diameter, so the installation of two objective lenses would be difficult.

1.4 Research overview

This dissertation focuses on improving the sectioning microscopy: for better sectioning capacity, more information and faster speed.

In Chapter 2, I introduce the physics background of this dissertation. I modulate the spatial fluorescence distribution with excitation patterns. In the first section, I have a short review of different diffraction theories, and in the second section, I quantitatively calculate the excitation intensity under different conditions. Then a useful relationship in STED between depletion power and resolution is derived as an example. Readers may skip this chapter if mathematical details are not the primary concern.

In Chapter 3, we improve the point-scanning microscopy with excitation laser modulations. We use a mirror to reflect the incident laser to produce interference patterns in the focal volume. We found both the sectioning capacity and the peak intensity of the excitation

and depletion beams in STED are improved and the signal-to-noise ratio is enhanced. First, we proved the improvement of sectioning capacity with a nano-particle phantom sample. We grew Vero cells on a silicon dioxide layer above the mirror and applied this method to samples on conventional spinning disk and two-photon microscopy. Further, we developed spectral methods to move the interference lay inside cell, making 3D observation possible. Finally, we demonstrated that the increase in intensity could be applied to reduce the required laser power in STED microscopy.

This dissertation also develops a point-scanning based phase contrast microscopy in Chapter 4: Schlieren Confocal microscopy. We found the incident laser refracts due to the local gradient of the sample, and the unblocked part of fluorescence could quantitatively reflect the local gradient of the sample. We applied this model to biological specimen measurements and found this method could obtain a similar effect as the Differential Interference Contrast microscopy, keep the optical sectioning capacity of confocal, and is fully compatible with confocal.

In Chapter 5, we applied excitation modulation to inhibit the background in light field microscopy. Light field microscopy sacrifices spatial resolution for speed and is preferable in fast biological phenomena. However, light field reconstruction problem is ill-defined, and it would cause a strong background. We combined selective plane illumination with microlens array coupled detection. This method can significantly reduce the background in conventional light field microscopy and has faster speed compared to the light sheet. It could be applied in samples with high label densities.

In chapter 6 I conclude the dissertation. The structure of this dissertation is shown in Figure 1.7.

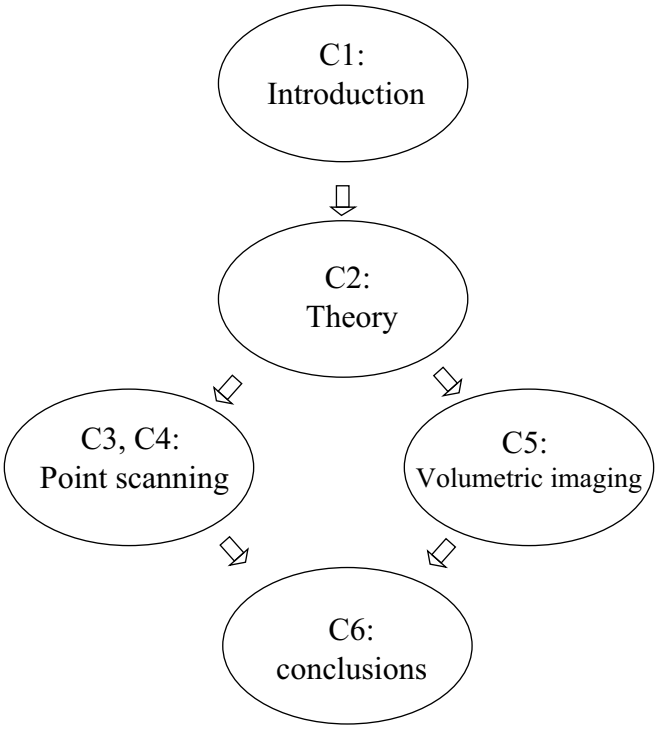

Figure 1.7: Roadmap of this dissertation.

CHAPTER 2

EXCITATION INTENSITY DISTRIBUTION IN THE FOCAL VOLUME

In this chapter, I present the mathematics and physics foundations of this dissertation. In this section, we are trying to answer the following question: What is the laser intensity distribution in the focal volume of the objective. Fluorescence is excited by the excitation laser, so the fluorescence spatial distribution could be modulated by excitation laser patterns. In the first section I have a short review of different diffraction theories, and in the second section, I quantitatively calculate the excitation intensity under different conditions.

2.1 Diffraction theories

2.1.1 Helmholtz equation, Kirchhoff scalar diffraction, and Rayleigh-Sommerfeld diffraction

Generally speaking, light is an electromagnetic wave, and all optical phenomena could be explained with the Maxwell equations [91, 31]. Let's consider a scalar wave first. The field of a monochromatic beam of light at point P and time t could be represented by $\tilde{U}(P,t) = \mathrm{Re}\{U(P)\exp(-\mathrm{i}2\pi f_v t)\}$. Here $U(P)$ should satisfy the Helmholtz equation

$$(\nabla^2 + k^2)U(P) = 0 \tag{2.1}$$

Kirchhoff used the Green function method to solve this equation [92]

$$U(P) = \frac{1}{4\pi}\iint_S [U\frac{\partial}{\partial n}(\frac{\exp(\mathrm{i}kr)}{r}) - \frac{\exp(\mathrm{i}kr)}{r}\frac{\partial U}{\partial n}]\mathrm{d}S \tag{2.2}$$

He further made two simple but inconsistent assumptions on the boundary conditions:

$$\begin{cases} U = 0 \\ \dfrac{\partial U}{\partial n} = 0 \end{cases} \tag{2.3}$$

Then the solution could be given when the detection point is not too close to the aperture

$$U(P) = \frac{\mathrm{i}U_0}{\lambda} \iint_{\Sigma} \frac{\exp[\mathrm{i}k(r+s)]}{rs} \frac{[\cos(n,s) - \cos(n,r)]}{2} \tag{2.4}$$

Rayleigh-Sommerfeld diffraction theory removes the assumptions in Equation 2.3 and gives an expression similar to the Huygens-Fresnel principle [93]:

$$\begin{cases} U_1(P) = -\dfrac{\mathrm{i}U_0}{\lambda} \iint_{\Sigma} \dfrac{\exp(\mathrm{i}kr + \mathrm{i}ks)}{rs} \cos(n,r)\mathrm{d}S \\ U_2(P) = \dfrac{\mathrm{i}U_0}{\lambda} \iint_{\Sigma} \dfrac{\exp(\mathrm{i}kr + \mathrm{i}ks)}{rs} \cos(n,s)\mathrm{d}S \\ U(P) = \dfrac{1}{2}[U_1(P) + U_2(P)] \end{cases} \tag{2.5}$$

Equation 2.4 and 2.5 are important in theory. But to simulate of the light intensity in the focal volume, Debye theory is more practical.

2.1.2 Vectorial diffraction theory with high numerical aperture objectives

Wolf in 1959 developed vectorial diffraction theory [94, 95] that the semi-aperture α on the image side is considered. He showed that the electric and magnetic vectors could be written as

$$\begin{cases} \boldsymbol{E}(x,y,z,t) = \mathrm{Re}\{\boldsymbol{e}(x,y,z)\mathrm{e}^{-\mathrm{i}\omega t}\} \\ \boldsymbol{H}(x,y,z,t) = \mathrm{Re}\{\boldsymbol{h}(x,y,z)\mathrm{e}^{-\mathrm{i}\omega t}\} \end{cases} \tag{2.6}$$

At coordination P(x,y,z) in the image space away from the exit pupil, the vectorial electric and magnetic fields are in the form

$$\begin{cases} \boldsymbol{e}(x,y,z) = -\dfrac{\mathrm{i}k}{2\pi}\iint_{\Omega}\dfrac{\boldsymbol{a}(s_x,s_y)}{s_z}\mathrm{e}^{\mathrm{i}k\Phi(s_x,s_y)+(s_xx+s_yy+s_zz)}\mathrm{d}s_x\mathrm{d}s_y \\ \boldsymbol{h}(x,y,z) = -\dfrac{\mathrm{i}k}{2\pi}\iint_{\Omega}\dfrac{\boldsymbol{b}(s_x,s_y)}{s_z}\mathrm{e}^{\mathrm{i}k\Phi(s_x,s_y)+(s_xx+s_yy+s_zz)}\mathrm{d}s_x\mathrm{d}s_y \end{cases} \tag{2.7}$$

Here a and b are strength vectors of the electric and magnetic fields on the exit pupil and $\boldsymbol{b} = \hat{s} \times \boldsymbol{a}$. To calculate $\boldsymbol{a}$ and $\boldsymbol{b}$, two factors need to be considered:

1. Energy is conserved along each ray.

2. Electric fields in the meridional plane and sagittal plane propagate independently.

If we assume the incident light intensity is l_0 and the refracted light intensity is l_1 along this ray, the first factor gives

$$l_0^2\delta S_0 = l_1^2\delta S_1 \tag{2.8}$$

Where S_0 and S_1 are the areas of the rays on the boundary. The Abbe sine condition requires $\delta S_0 = \delta S_1 \cos\theta$, so we have

$$l_1 = l_0 \cos^{\frac{1}{2}}\theta \tag{2.9}$$

Next we consider the direction. If the electric field is in the meridional plane and its direction is $\hat{g}_0$, its direction after refraction is $\hat{g}_1$, given by the Snell refraction law. Similarly, for light polarized in the sagittal plane, the new directional vector is $\hat{g_1} \times \hat{s}$. So we have

$$\boldsymbol{a} = l_0\cos^{\frac{1}{2}}\theta[(\hat{g}_0 \cdot \vec{i})\hat{g}_1 + (\hat{g}_0 \cdot \vec{j})(\hat{g}_1 \times \hat{s})] \tag{2.10}$$

In order to numerically calculate this expression, spherical coordinate (r, θ, ϕ) is induced

with $r \geq 0, 0 < \theta < \pi$, $0 < \phi < 2\pi$ and its transformation from (x, y, z) is

$$\begin{cases} s_x = \sin\theta\cos\phi \\ s_y = \sin\theta\sin\phi \\ s_z = \cos\theta \end{cases} \tag{2.11}$$

$$\begin{cases} x = r_p\sin\theta_P\cos\phi_P \\ y = r_p\sin\theta_P\sin\phi_P \\ z = r_p\cos\theta_P \end{cases} \tag{2.12}$$

It could then be derived

$$\begin{cases} a_x = l_0\cos^{\frac{1}{2}}\theta[\cos\theta + \sin^2\phi(1-\cos\theta)] \\ a_y = l_0\cos^{\frac{1}{2}}\theta[(\cos\theta - 1)\cos\phi\sin\phi] \\ a_z = -l_0\cos^{\frac{1}{2}}\theta\sin\theta\cos\phi \\ b_x = l_0\cos^{\frac{1}{2}}\theta[(\cos\theta - 1)\cos\phi\sin\phi] \\ b_y = l_0\cos^{\frac{1}{2}}\theta[1 - \sin^2\phi(1-\cos\theta)] \\ b_z = l_0\cos^{\frac{1}{2}}\theta\sin\theta\cos\phi \end{cases} \tag{2.13}$$

The last step is to transform the term $\mathrm{d}s_x\mathrm{d}s_y$. Since $\frac{\partial s_x}{\partial\theta} = \cos\theta\cos\phi$, $\frac{\partial s_x}{\partial\phi} = -\sin\theta\sin\phi$, $\frac{\partial s_y}{\partial\theta} = \cos\theta\sin\phi$, $\frac{\partial s_x}{\partial\phi} = \sin\theta\sin\phi$, the Jacobian matrix is

$$\begin{vmatrix} \frac{\partial s_x}{\partial\theta} & \frac{\partial s_x}{\partial\phi} \\ \frac{\partial s_y}{\partial\theta} & \frac{\partial s_y}{\partial\phi} \end{vmatrix} = \sin\theta\cos\theta \tag{2.14}$$

So we have

$$\begin{cases} e_x = -\dfrac{\mathrm{i}A}{\pi}\displaystyle\int_0^{\alpha}\int_0^{2\pi} \cos^{\frac{1}{2}}\theta \sin\theta\{\cos\theta + (1-\cos\theta)\sin^2\phi\}\mathrm{e}^{\mathrm{i}kr_p\cos\epsilon+\mathrm{i}k\Phi(\theta,\phi)}\mathrm{d}\theta\mathrm{d}\phi \\ e_y = \dfrac{\mathrm{i}A}{\pi}\displaystyle\int_0^{\alpha}\int_0^{2\pi} \cos^{\frac{1}{2}}\theta \sin\theta(1-\cos\theta)\sin\phi\cos\phi\mathrm{e}^{\mathrm{i}kr_p\cos\epsilon+\mathrm{i}k\Phi(\theta,\phi)}\mathrm{d}\theta\mathrm{d}\phi \\ e_z = \dfrac{\mathrm{i}A}{\pi}\displaystyle\int_0^{\alpha}\int_0^{2\pi} \cos^{\frac{1}{2}}\theta\sin^2\theta\cos\phi\mathrm{e}^{\mathrm{i}kr_p\cos\epsilon+\mathrm{i}k\Phi(\theta,\phi)}\mathrm{d}\theta\mathrm{d}\phi \\ h_x = -\dfrac{\mathrm{i}A}{\pi}\displaystyle\int_0^{\alpha}\int_0^{2\pi} \cos^{\frac{1}{2}}\theta \sin\theta(1-\cos\theta)\cos\phi\sin\phi\mathrm{e}^{\mathrm{i}kr_p\cos\epsilon+\mathrm{i}k\Phi(\theta,\phi)}\mathrm{d}\theta\mathrm{d}\phi \\ h_y = -\dfrac{\mathrm{i}A}{\pi}\displaystyle\int_0^{\alpha}\int_0^{2\pi} \cos^{\frac{1}{2}}\theta \sin\theta\{1-(1-\cos\theta)\sin^2\phi\}\mathrm{e}^{\mathrm{i}kr_p\cos\epsilon+\mathrm{i}k\Phi(\theta,\phi)}\mathrm{d}\theta\mathrm{d}\phi \\ h_z = \dfrac{\mathrm{i}A}{\pi}\displaystyle\int_0^{\alpha}\int_0^{2\pi} \cos^{\frac{1}{2}}\theta\sin^2\theta\sin\phi\mathrm{e}^{\mathrm{i}kr_p\cos\epsilon+\mathrm{i}k\Phi(\theta,\phi)}\mathrm{d}\theta\mathrm{d}\phi \end{cases} \tag{2.15}$$

where $A = kfl_0/2$, $\cos\epsilon = \cos\theta\cos\theta_P + \sin\theta\sin\theta_P\cos(\phi-\phi_P)$ and $\Phi(\theta,\phi)$ is the aberration function of the system.

2.1.3 Scalar diffraction theory with high numerical aperture objectives

When the polarization of light is not important, Debye approximation could be used in the focal volume [92]. This theory also assumes the incident wave could be expanded as a series of plane waves:

$$U(\boldsymbol{R}) = \frac{\mathrm{i}}{\lambda}\iint_{\Omega}\exp(\mathrm{i}k\boldsymbol{s}\cdot\boldsymbol{R})\mathrm{d}\Omega \tag{2.16}$$

Here $U(\boldsymbol{R})$ is the field distribution on the spherical wavefront. Transform it into spherical coordinates,

$$U(\nu,\mu) = \frac{2\pi\mathrm{i}}{\lambda}\exp(\mathrm{i}kz_2)\int_0^{\alpha}P(\theta)J_0(\frac{\nu\sin\theta}{\sin\alpha})\exp(-\frac{\mathrm{i}\mu\sin^2(\theta/2)}{2\sin^2(\alpha/2)})\sin\theta\mathrm{d}\theta \tag{2.17}$$

Under the Sine condition, $P(\theta) = \sqrt{\cos\theta}$. And μ, ν are normalized coordinates

$$\begin{cases} \nu = kr_2\sin\alpha \\ \mu = 4kz_2\sin^2(\alpha/2) \end{cases} \tag{2.18}$$

This approximation is accurate enough when the Fresnel number $N = \pi a^2/(\lambda z) \gg 1$.

2.1.4 Fresnel approximation

When the paraxial approximation $\sin\theta = \theta$ is applied to Equation 2.17, it gives

$$U(\nu,\mu) = 2\frac{N\mathrm{i}}{f}\exp(\mathrm{i}kz_2)\int_0^1 P(\rho)\exp(\frac{-\mathrm{i}\mu\rho^2}{2})J_0(\rho\nu)\rho\mathrm{d}\rho \tag{2.19}$$

where $\rho = r_2/a$ and a is the radius of the objective aperture. Usually it gives a very good approximation of Equation 2.17 [92].

2.2 Excitation intensity modulation applications

2.2.1 Focal intensity distribution with a spiral phase plate

In this example, we calculate the excitation and depletion laser field in STED, which would be applied in Chapter 3. First, we use the vectorial diffraction theory to calculate the excitation and depletion intensity. Then the residue fluorescence is calculated, and connection among the resolution, the depletion power and the saturation power measured in experiments is established.

Intensity of the excitation and the depletion beams

There are at least two laser beams in a STED system. One is a diffraction limited Gaussian excitation beam, and the other is a donut-shaped depletion beam. In an idealistic Gaussian image system, $\Phi(\theta,\phi) = 0$ in Equation 2.15 yields

$$\begin{cases} e_x(P) = -\mathrm{i}A_{1x}(I_0 + I_2\cos 2\phi_p) \\ e_y(P) = -\mathrm{i}A_{1x}I_2\sin 2\phi_p \\ e_z(P) = -2A_{1x}I_1\cos\phi_p \end{cases} \tag{2.20}$$

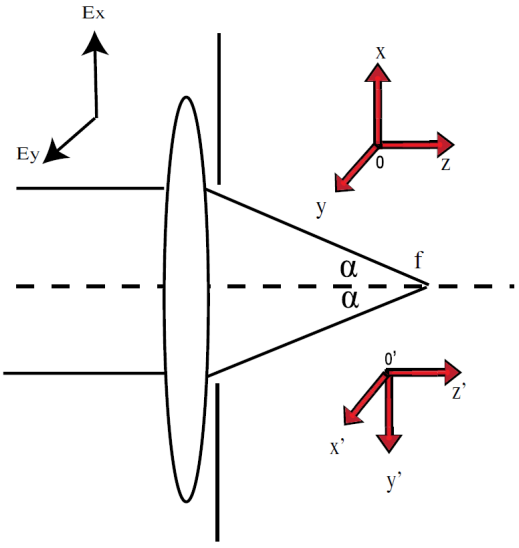

Figure 2.1: Coordinate systems of a high NA microscopic objective [96].

where $A_{1x} = k_1 f e_{1x}/2$, $k_1 = 2\pi/\lambda_{ex}$ and e_{1x} is the linear excitation electric field along the x-axis, and on the focal plane integration I_0, I_1, I_2 are given by

$$\begin{cases} I_0 = \int_0^{\alpha} \cos^{\frac{1}{2}}\theta \sin\theta(1+\cos\theta) J_0(k_1\rho_p \sin\theta) \exp(\mathrm{i}k_1 z_p \cos\theta)\mathrm{d}\theta \\ I_1 = \int_0^{\alpha} \cos^{\frac{1}{2}}\theta \sin^2\theta J_1(k_1\rho_p \sin\theta) \exp(\mathrm{i}k_1 z_p \cos\theta)\mathrm{d}\theta \\ I_2 = \int_0^{\alpha} \cos^{\frac{1}{2}}\theta \sin\theta(1-\cos\theta) J_2(k_1\rho_p \sin\theta) \exp(\mathrm{i}k_1 z_p \cos\theta)\mathrm{d}\theta \end{cases}$$

where $\rho_p = (x_p^2 + y_p^2)^{1/2}$.

In STED a 0-2π phase mask is generally used, as it can generate the most efficient inhibition pattern for fluorescence depletion [97]. The electric fields of a depletion beam with distinct polarization states can be calculated [98]. Notice $\int_0^{2\pi} \exp\{\mathrm{i}n\phi + \rho\cos\phi\}\mathrm{d}\phi = 2\pi\mathrm{i}^n J_n(\rho)$, and substitute $\exp(\mathrm{i}kr_p\cos\epsilon) = \mathrm{e}^{\mathrm{i}kz_p\cos\theta}\mathrm{e}^{\mathrm{i}k\rho_p\sin\theta\cos(\phi-\phi_p)}\mathrm{e}^{\mathrm{i}k\Phi(\theta,\phi)}$ into Equation

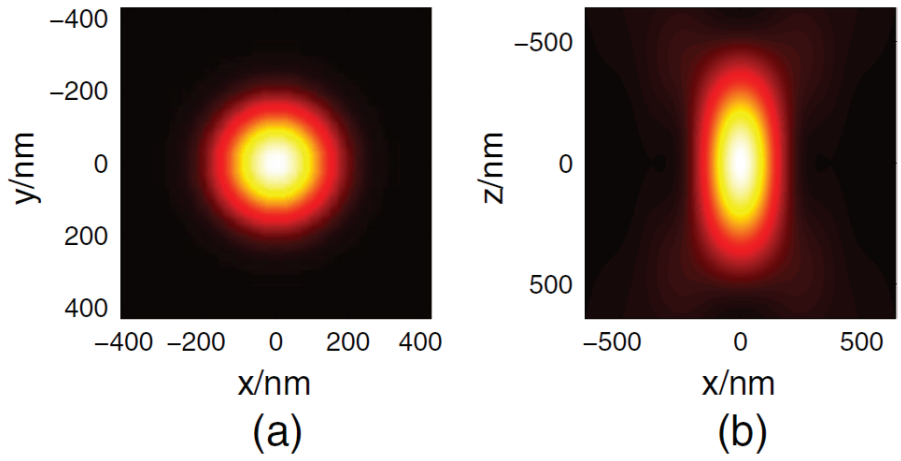

Figure 2.2: Excitation intensity on (a)the XY plane and (b) the XZ plane [96].

2.15, where the phase function of the 0-2π phase plate is $\mathrm{e}^{\mathrm{i}k\Phi(\theta,\phi)} = \mathrm{e}^{\mathrm{i}\phi}$, we derive:

$$\begin{cases} e_x = A_{2x}[\mathcal{I}_1 \exp(\mathrm{i}\phi_p) - \dfrac{1}{2}\mathcal{I}_2 \exp(-\mathrm{i}\phi_p) + \dfrac{1}{2}\mathcal{I}_3 \exp(\mathrm{i}3\phi_p)] \\ e_y = -\dfrac{\mathrm{i}A_{2x}}{2}[\mathcal{I}_2 \exp(-\mathrm{i}\phi_p) + \mathcal{I}_3 \exp(\mathrm{i}3\phi_p)] \\ e_z = \mathrm{i}A_{2x}[\mathcal{I}_4 - \mathcal{I}_5 \exp(\mathrm{i}2\phi_p)] \end{cases} \tag{2.21}$$

Here $A_{2x} = k_2 f e_{2x}/2$ is proportional to the linear depletion electric field, and $k_2 = 2\pi/\lambda_{de}$. The angular integrations $\mathcal{I}_1 - \mathcal{I}_5$ are defined as

$$\begin{cases} \mathcal{I}_1 = \displaystyle\int_0^\alpha \mathrm{d}\theta \cos^{\frac{1}{2}}\theta \sin\theta J_1(k_2\rho_p \sin\theta)(1+\cos\theta)\mathrm{e}^{\mathrm{i}k_1 z_p \cos\theta} \\ \mathcal{I}_2 = \displaystyle\int_0^\alpha \mathrm{d}\theta \cos^{\frac{1}{2}}\theta \sin\theta J_1(k_2\rho_p \sin\theta)(1-\cos\theta)\mathrm{e}^{\mathrm{i}k_1 z_p \cos\theta} \\ \mathcal{I}_3 = \displaystyle\int_0^\alpha \mathrm{d}\theta \cos^{\frac{1}{2}}\theta \sin\theta J_3(k_2\rho_p \sin\theta)(1-\cos\theta)\mathrm{e}^{\mathrm{i}k_1 z_p \cos\theta} \\ \mathcal{I}_4 = \displaystyle\int_0^\alpha \mathrm{d}\theta \cos^{\frac{1}{2}}\theta \sin\theta J_0(k_2\rho_p \sin\theta)\sin\theta\mathrm{e}^{\mathrm{i}k_1 z_p \cos\theta} \\ \mathcal{I}_5 = \displaystyle\int_0^\alpha \mathrm{d}\theta \cos^{\frac{1}{2}}\theta \sin\theta J_2(k_2\rho_p \sin\theta)\sin\theta\mathrm{e}^{\mathrm{i}k_1 z_p \cos\theta} \end{cases}$$

For circular polarization incidence, the electric field can be obtained by a coordinate rotation [99]. The electromagnetic fields now consist of contributions of two linear polarized

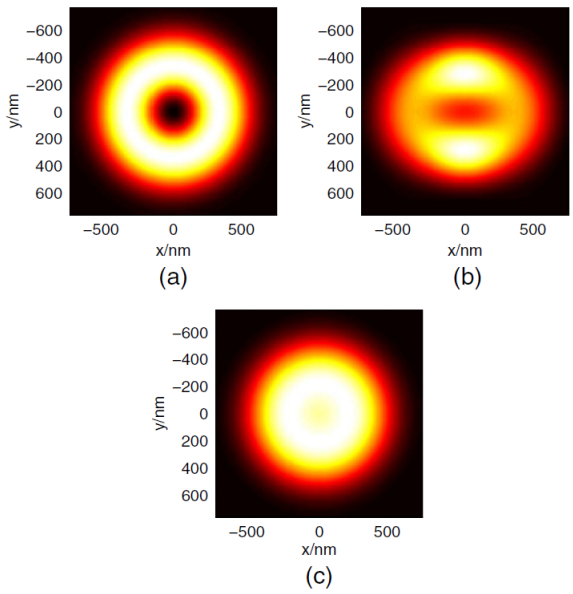

Figure 2.3: Intensity on the XY plane of the focus for the depletion laser with (a) left-circular polarized, (b) linear polarized, and (c) right-circular polarized laser [96].

incident fields along the x-axis and the y-axis:

$$\begin{cases} E_x(r_p, \theta_p, \phi_p) = e_x(r_p, \theta_p, \phi_p) - e'_{y'}(r'_p, \theta'_p, \phi'_p) \\ E_y(r_p, \theta_p, \phi_p) = e_y(r_p, \theta_p, \phi_p) + e'_{x'}(r'_p, \theta'_p, \phi'_p) \\ E_z(r_p, \theta_p, \phi_p) = e_z(r_p, \theta_p, \phi_p) + e'_{z'}(r'_p, \theta'_p, \phi'_p) \end{cases} \tag{2.22}$$

where $r'_p = r_p$, $\theta'_p = \theta_p$, $\phi'_p = \phi_p - \frac{\pi}{2}$. Then the intensity of the laser field could be calculated by $I = E_x E_x^* + E_y E_y^* + E_z E_z^*$ for both the excitation and depletion beams. The excitation and depletion intensity distributions are drawn in Figure 2.2 and Figure 2.3. It should be noticed that the center of the vortex is zero only when the incident laser is left-circular; otherwise, a non-zero electric component exists. That is because in left-circular case, two orthogonal electric fields have two $\pi/2$ phase difference from the circular polarization and the phase plate, so their z component canceled out at the focal point.

Intensity of the residue fluorescence

To calculate the residue fluorescence after the depletion process, we need to make a further assumption on the laser trigger mode. We investigate two extreme cases. If both the excitation and depletion lasers are continues, the portion of electrons remaining on the excitation state is $\eta(I_{de}) = 1/(1 + I_{de}/I_s)$ according to equilibrium equation; if the depletion laser is pulsed, this extinction efficiency could be written as $\eta(I_{de}) = \exp(-\ln 2(I_{de}/I_s))$. These two expressions give very close results when $I_{de} < I_s$.

With this assumption we are able to calculate the illumination PSF after depletion $h_{illum} = I_{ex}(x, y, z)\eta(I_{ex}(x, y, z))$. We use STED3D (`https://github.com/Crazyonxh/STED3D.git`), a Matlab GUI program to automate this process. For more details, see the software manual.

Using the depletion power to predict system resolution

Now all parameters could be directly measured in experiments except the saturation intensity I_s. In reality, single fluorophore are easy to bleach, so the measurement of I_s is often replaced by the measurement of saturation power P_s in solutions [100, 101]:

1. Measure the average fluorescence intensity of the excitation beam by scanning the focus across the fluorescent solution (a uniform function);

2. Introduce the depletion beam without phase modulation, whose PSF should be overlapped with the PSF of the excitation;

3. Adjust the depletion power until the total fluorescence intensity is depleted to its half.

Therefore, it is more convenient to express the resolution of STED with the relationship of $P/\mathcal{P}_s$, where P is the depletion power and $\mathcal{P}_s$ is defined by the depletion power when the detected integrated fluorescence intensity (scanning across solution) is reduced by half. The detected integrated fluorescence could calculated by $I = \iiint i_{illum}(x, y, z)h_{det}(x, y, z)\mathrm{d}V$,

where $h_{det}(x, y, z)$ is the detection PSF. Assuming we use a point detector and omit the Stokes shift of fluorescence, numerical evaluation of the factor reveals $P = \mathcal{P}_s$ approximately corresponds to $I = 2I_s$. Then the resolution vs. STED power relationship becomes [100, 102]

$$FWHM = \frac{\lambda_{ex}}{\alpha NA\sqrt{1 + \chi P/\mathcal{P}_s}} \tag{2.23}$$

where P is the depletion power, $\mathcal{P}_s$ is the saturation power when the fluorescence is reduced by half. Our representation of the resolution then becomes $FWHM = \lambda_{ex}/(1.82NA\sqrt{1 + 0.45P/\mathcal{P}_s})$. In the derivation of this equation, we have assumed both the excitation and depletion lasers are left-circular and expand their expression of intensity into series of radius r. For details, see Appendix B.

2.2.2 Intensity distribution with a mirror

In this example, we use the scalar Debye theory to calculate the interfered laser pattern with a mirror placed near the focal plane. This result would be applied in Chapter 3. We further assume the samples have uniform refractive index $n = 1.5$ and the mirror is composed of silver. For a detection point $P(x, y, z)$ near the focal point, the wave field could be written as

$$U_{ex}(x, y, z,) = U_{in}(x, y, z) + U_{ref}(x, y, z) \tag{2.24}$$

The field could be calculated with optical ray tracing. We draw the mirror image of the incident laser aperture in Figure 2.4. The reflected optical light path length for each optical ray could be calculated by its mirror image: $U_{ref}(x, y, z) = U'_{in}(x', y', z')$ where (x', y', z') is the mirror image of this detection coordination. Further, a phase shift from reflection needs to be taken into account [31]:

$$n_1 \sin\theta_1 = n_2 \sin\theta_2 \tag{2.25}$$

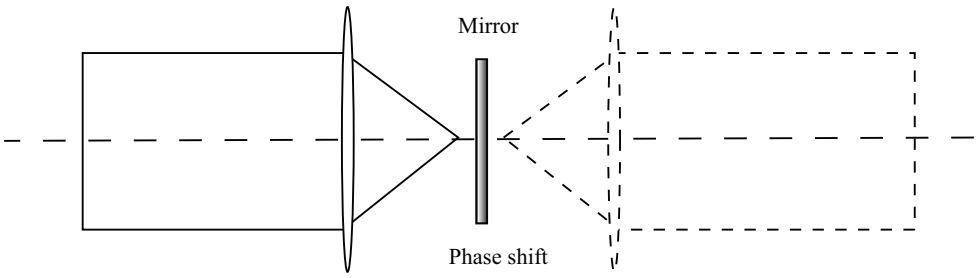

Figure 2.4: Model for intensity calculation with a mirror.

And

$$\begin{cases} r_1 = \dfrac{\tan(\theta_1 - \theta_2)}{\tan(\theta_1 + \theta_2)} \\ r_2 = \dfrac{\sin(\theta_1 - \theta_2)}{\sin(\theta_1 + \theta_2)} \end{cases} \tag{2.26}$$

Here r_1 and r_2 are the reflective rates of the electric fields parallel or orthogonal to the meridional plane. They are very close when the incident angle θ_1 is not very large, and we use $r = (r_1 + r_2)/2$ as an average. The reflective index of the medium is $n_1 = 1.5$, and for silver it is wavelength dependent [103, 104]. The amplitude of the reflected rates is close to 1, but phase shifts exist due to the imaginary part of the refractive index $n = n_0 + ik$. Finally, the field strength could be written as

$$U_{in}(\nu, \mu) = \frac{2\pi \mathrm{i}}{\lambda} \exp(\mathrm{i}kz_2) \int_0^\alpha P(\theta) J_0(\frac{\nu \sin\theta}{\sin\alpha}) \exp(\frac{-\mathrm{i}\mu \sin^2(\theta/2)}{2\sin^2(\alpha/2)}) \sin\theta \mathrm{d}\theta \tag{2.27}$$

for the incident laser and

$$U_{ref}(\nu, \mu) = U_{in}(\nu', \mu') = \frac{2\pi \mathrm{i}}{\lambda} \exp(\mathrm{i}kz_2') \int_0^\alpha P(\theta) r(\theta) J_0(\frac{\nu' \sin\theta}{\sin\alpha}) \exp(-\frac{\mathrm{i}\mu' \sin^2(\theta/2)}{2\sin^2(\alpha/2)}) \sin\theta \mathrm{d}\theta \tag{2.28}$$

for the reflected laser.

The last step is to establish a connection between (x, y, z) and (x', y', z'). we can assume the equation of the mirror plane is $ax + z + c = 0$, and the mirror image of $P(x, y, z)$ is $P'(x', y', z')$. PP' should be normal to the plane and their midpoint is on the plane. So

we have

$$\begin{cases} x - x' = a(z - z') \\ a(x + x') + (z + z') + 2c = 0 \end{cases} \tag{2.29}$$

The solution is

$$\begin{cases} x' = \dfrac{(1 - a^2)x - (a^2 + a)z - 2ca}{a^2 + 1} \\ z' = \dfrac{-2ax + (a^2 - a)z - 2c}{a^2 + 1} \end{cases} \tag{2.30}$$

$a = 0$ corresponds to the mirror is normal to the optical axis. The source code is available at `https://github.com/Crazyonxh/MEANS`.

2.2.3 Intensity distribution with circular and cylindrical lenses

This example is to estimate the FWHM with spherical and cylindrical lenses under the paraxial approximation. This conclusion would be applicable to the estimation of the light sheet parameters in Chapter 5. According to the Fresnel diffraction theory, the diffraction field amplitude U at the position (x, y) is

$$U(x, y, z) \propto \iint \mathrm{d}S' U_0(x', y') \exp\{\mathrm{i}kl(x, y, z, x', y')\} \tag{2.31}$$

The cylindrical lens could be modeled as a modulation function
$U(x', y') = A_0 \exp(-\mathrm{i}kx'^2/2f)$, so the integration over the area could be degenerated to integration over x'. Under paraxial approximation, the distance between each point on the exit pupil and the detection point is

$$l(x, x', z) = \sqrt{(x - x')^2 + z^2} \approx z + (x^2 + x'^2 - 2xx')/2z \tag{2.32}$$

On the focal plane $z = f$, quadratic terms cancel out. If we define $NA = a/f$, we have

$$I(x, z = 0) = I_0 \mathrm{sinc}^2(\frac{kxa}{f}) \tag{2.33}$$

And the FWHM is approximately given by

$$d_{LS} = 0.44\frac{\lambda}{NA} \tag{2.34}$$

On the optical axis $x = 0$. With $\delta z = |z - f|$, and $S(x) = \int_0^x \sin^2(\pi t/2)\mathrm{d}t$, $C(x) = \int_0^x \cos^2(\pi t/2)\mathrm{d}t$, we have

$$I(0,z) = \frac{I_0}{k\delta z}(S^2(\sqrt{\frac{2\delta z}{\lambda}}NA) + C^2(\sqrt{\frac{2\delta z}{\lambda}}NA)) \tag{2.35}$$

And the FWHM is given approximately by $L_{LS} = 1.73n\lambda/NA^2$.

Next, we consider the modulation of the detection objective's PSF. A point light source is located on the optical axis, and its distance to the center of the objective is z_0. The objective lens could be modeled as a modulation function $A(x') = A_0\exp(-\mathrm{i}k(x^2+y^2)/2f) = A_0\exp(-\mathrm{i}kr'^2/2f)$. Under paraxial approximation, distance between each point on the exit pupil and the detection point is
$l(\vec{x}', \vec{x}) = \sqrt{z_0^2 + r^2 + r'^2 - 2rr'\cos\theta} \approx z_0 + (r^2 + r'^2 - 2rr'\cos\theta)/2z_0$, where r and θ are the polar coordinates. On the focal plane, we have

$$I(r', 0) = I_0(\frac{J_1(\frac{kr'a}{f})}{\frac{kr'a}{f}})^2 \tag{2.36}$$

Where J_n is the n-th Bessel function and the FWHM is given approximately by

$$d_{LS} = 0.51\lambda/NA \tag{2.37}$$

On the optical axis $x = 0$. With $\delta z = |z - f|$,

$$I(0,z) = I_0\mathrm{sinc}^2(\frac{kx'a}{4f}) \tag{2.38}$$

And the FWHM is given approximately by $L_{LS} = 1.76n\lambda/NA^2$

A light sheet system uses a cylindrical lens for illumination and an objective for detection. The system PSF is the product of the excitation PSF and the detection PSF. Usually, lateral resolution is smaller than the axial resolution. So when these two lenses are orthogonally installed and their focal points are overlapped, both the lateral and axial resolution of the system are inversely proportional to the NA of the lenses.

CHAPTER 3
ENHANCING THE SECTIONING CAPACITY IN POINT-SCANNING MICROSCOPY

In this chapter, we propose a method to further enhance the sectioning of the point-scanning microscopy. As we have discussed in Chapter 1, a point-scanning system has a sectioning capacity with the help of its point excitation and point detection. However, point-scanning systems also have anisotropic point spread function, and their axial resolutions are not as good as their lateral resolutions. In this work, we report a practical approach to achieving axial super-resolution on the base of the point-scanning confocal and STED systems. We found that when a mirror is placed behind the specimen, the interference between the excitation point spread function (PSF) and its reflection creates an axially narrowed PSF, approximately 100 nm in thickness, positioned about 100 nm away from the mirror surface. Therefore, this Mirror Enhanced Axial Narrowing Super-resolution (MEANS) technique enables higher axial resolution than the optical diffraction limit. With the axial sectioning capability and improvement of MEANS-STED super-resolution, fine structures of the nuclear pore complexes and filamentous virions have been successfully revealed with optical microscopy.

In the first section, we review the previous interference microscopy. Then we show the simulation of the excitation field as discussed in Chapter 2. Section 3.3 is about how to cultivate cells on the mirror surfaces, and in section 3.4 we present the experimental results. First, we designed a signal-to-background experiment to validate our claim on optical sectioning. Then we applied MEANS to confocal, spinning disk and two-photon microscopy. Further, We changed the coating thickness on mirrors and the excitation laser wavelength to alter the position of the interference layer. Finally, we implemented our MEANS technology with STED. This work is accomplished in cooperation with Xusan

Yang from Peking University and Eric Alonas from Georgia Institute of Technology. Part of section 3.3-3.4 has been published in Reference [105].

3.1 Introduction and previous work

The confinement of the excitation light is the key optical microscopy to resolve fine sub-cellular structures against background [106]. Optical interference has been used to enhance the axial resolution by generating different types of excitation modulation in wide-field fluorescence microscopy [107, 108, 109, 110, 111, 112, 113]. Here we have a short review on these previous works in Figure 3.3:

3.1.1 4pi microscopy

The first practical 4pi microscope was set up by Stefan Hell in 1992 [102]. In his work, he reduced the axial extent of the confocal point spread function with the help of constructive interference. He used two microscope objectives with high numerical apertures. A fluorescent sample can be illuminated coherently from both sides, and the fluorescence emission could also be detected from both sides. This results in a point spread function determined by the interference of two wave fronts in a common focal volume.

Three types of 4pi microscopy are discussed in his paper. Type A uses the illumination interference; Type B uses the detection interference, and type C utilizes the interference of both the illumination and the detection. It was demonstrated that the axial FWHM of his PSF is 110 nm, compared to the original FWHM 540 nm of confocal.

The schematic diagram of 4pi microscopy is shown in Figure 3.1. One problem of 4pi microscopy is the alignment of the system is difficult because sub-wavelength accuracy is required for those two arms [114].

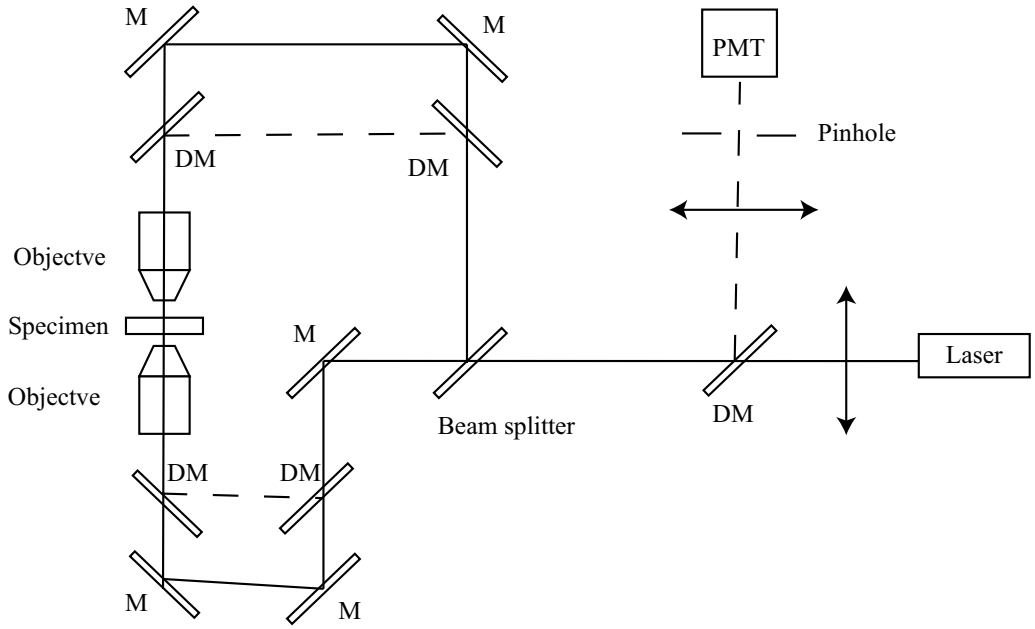

Figure 3.1: Schematic diagram of 4pi confocal fluorescence microscopy [102]. Solid lines: laser, dashed lines: fluorescence, M: mirrors, DM: dichroic mirrors.

3.1.2 I^5M microscopy

I^5M microscopy was developed by Gustafsson in 1995 [115]. The schematic diagram of I^5M is very similar to 4pi confocal fluorescence microscopy, except it is based on wide field configurations. An incoherent light source like arc lamp is used as the illumination light source, and there is no pinhole placed in front of the detector. There are also three different configurations of I^5M in excitation and detection.

Compared to 4pi confocal fluorescence microscopy, I^5M has faster raw data acquisition speed. However, it has more pronounced side lobes and relevant later substructures [116].

3.1.3 Standing wave microscopy

Bailey et al. enhanced the axial resolution of fluorescence microscopy by standing-wave excitation. In standing-wave fluorescence microscopy (SWFM), they used two coherent

plane waves from a laser across the specimen to form the interference:

$$L_{ex}(z) = 1 + \cos(Kz + \phi) \tag{3.1}$$

where $K = (4\pi n/\lambda)\cos\theta$ and λ is the wavelength of the excitation laser, and n is the refractive index of the sample. Since the fluorescence excited from the specimen is proportional to $I_{ex}(z)$, the nodes and antinodes of the field have a spacing $\Delta x = \lambda/(2n\cos\theta)$. As a result, the axial resolution of this system could be estimated as $\lambda/4n$, about 100 nm for water.

3.1.4 Isotropic diffraction-limited focusing using a single objective lens

This work is developed by Mudry et al. in 2010 [110]. They used a spatial light modulator to create two symmetric focal spots and used a mirror behind the sample to overlap these two focal spots.

They used the time-reversal theory to calculate the phase required to generate these two focal spots. The reflected field is obtained by illuminating the mirror with a beam made of plane waves propagating in all the $-\mathbf{u}$ directions, with complex amplitudes $e^*(\mathbf{u})$. It is proportional to the imaginary part of the field emitted by the dipole. So according to the field generated by a dipole and its mirror image, phase modulation could be calculated.

3.1.5 Spectral self-interference fluorescence microscopy

Spectral self-interference fluorescence microscopy is developed in 2004 by Moiseev et al. [117]. They presented an electromagnetic model of spectral self-interference to determine the precise position of fluorescent molecules above reflecting dielectric interfaces. They calculated the electromagnetic field of a dipole, kept the far field components only, and took into account all the multiple reflections from the layers below the interface. In their later work, they used this interferometric technique to measure the average location of

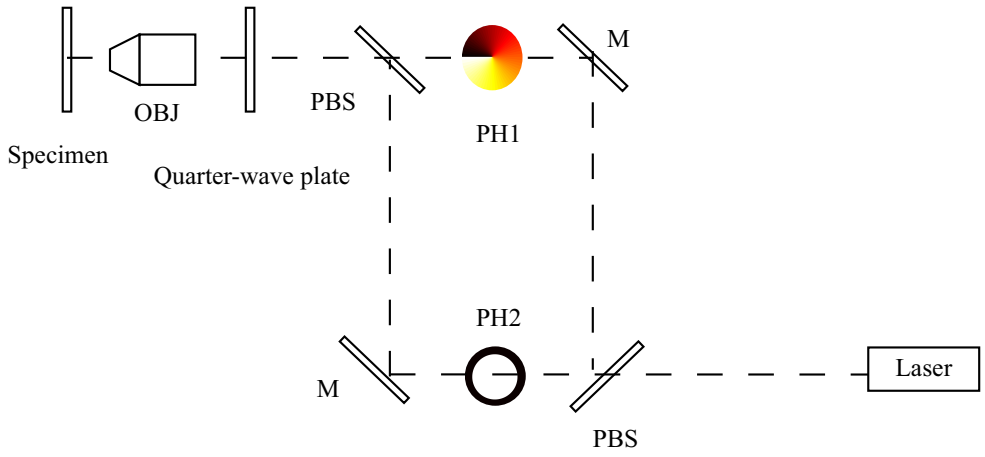

Figure 3.2: Schematic diagram of 3D STED [119]. Only depletion beam is drawn here.

a fluorescent label in a DNA layer relative to the surface [118]. They estimated the shape of coiled single-stranded DNA, the average tilt of double-stranded DNA of different lengths, and the amount of hybridization.

3.1.6 3D Stimulated emission depletion microscopy

3D STED could be realized by a phase plate or with 4pi microscope. Here we introduce the phase plate configuration described in Reference [119]. Schematic diagram of this configuration is drawn in Figure 3.2. They used a vortex phase plate to achieve lateral superresolution and a custom-made radially stepwise phase plate to obtain axial superresolution. The phase modulation of the phase plate could be described as $\Psi(\theta) = n\pi\eta(\theta - P\alpha)$, where θ denotes the semi-aperture angle and η is the Heaviside step function.

With this configuration, they succeed in reducing their resolution to 45*45*108 nm [119]. The challenge of this method is the optical alignment of the excitation beam and two depletion beams.

3.2 Theoretical simulation on MEANS and MEANS-STED PSFs

We found the axial resolution of the scanning microscopy could be enhanced by a mirror behind the sample. To predict the axial confinement of the PSF, we simulated the excitation

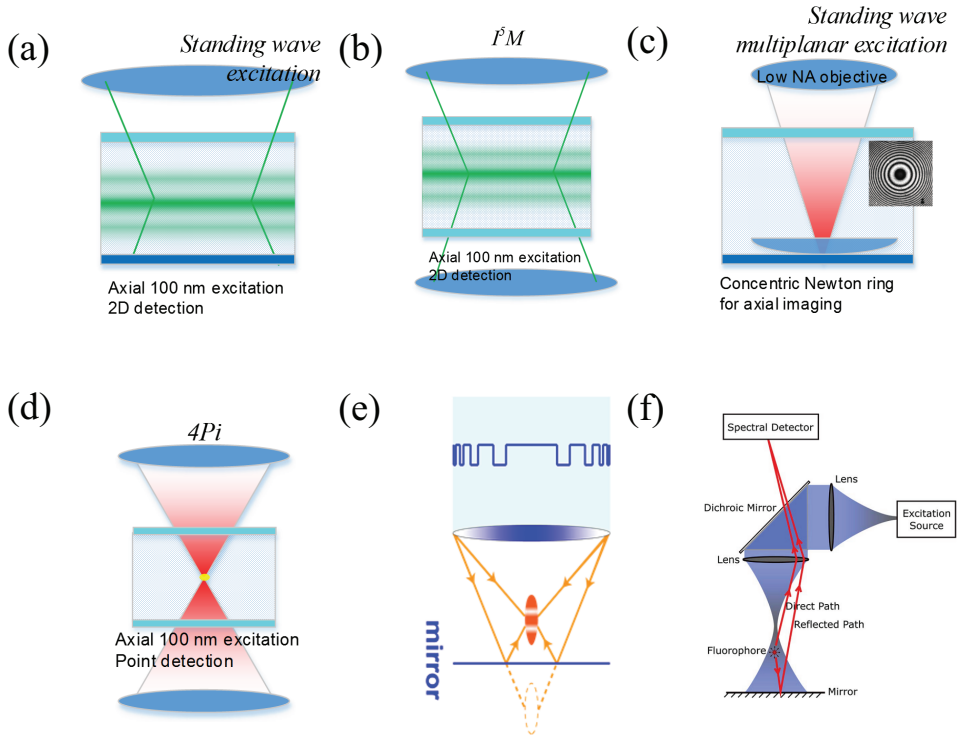

Figure 3.3: A review of previous self-interference microscopy [105]: (a) Standing wave microscopy is based on wide-field microscopy. It enhances the local electromagnetic field through interference. (b) $\mathrm{I}^5\mathrm{M}$ is also a wide-field based interference microscopy. Using two opposing objectives, it experimentally demonstrates the wide-field axial narrowing. (c)Standing wave multiplanar excitation microscopy employs a low NA objective, a flat mirror, and a plano-convex lens to mount the specimen. The number of interference Newton rings denotes the axial positions of the fluorophores. (d) 4Pi is a confocal point-scanning microscopy with two opposing objectives, with axially narrowed PSF. (e) Isotropic diffraction-limited focusing uses the interference of two real focal spots produced by phase modulation; one of them is then reflected by a mirror to generate interference. (f) SSFM utilizes fluorescence spectrum information to extract the axial positions of fluorophores. A mirror with a spacer much larger than the wavelength ($> 10\lambda$) is employed.

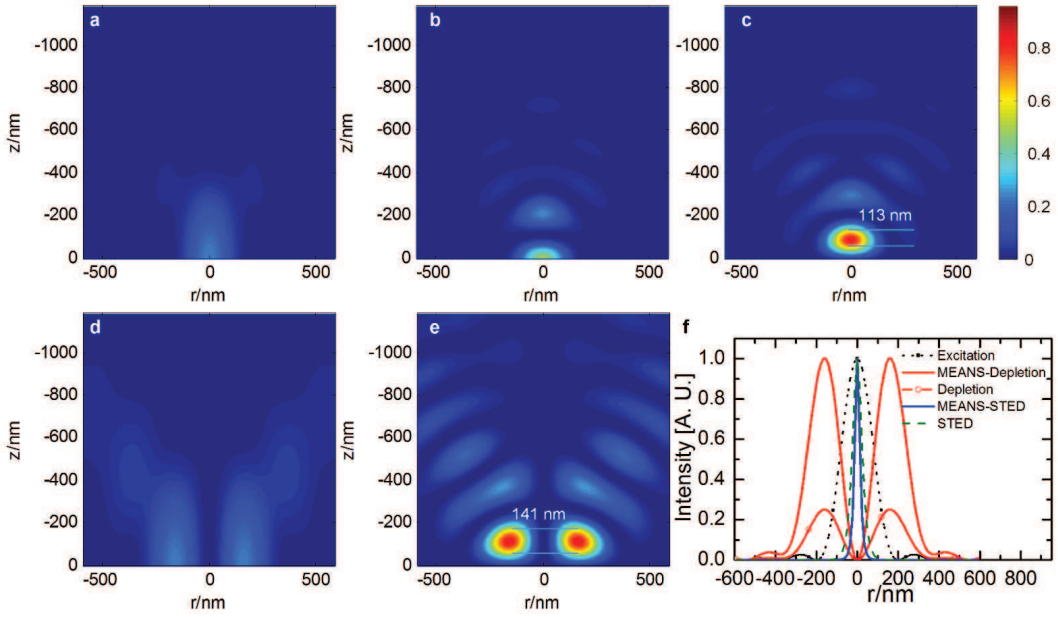

Figure 3.4: Numerical simulations of focal intensity profiles of (a) confocal excitation, (b) 4Pi excitation, (c) MEANS excitation, (d) STED depletion, (e) MEANS-STED depletion [105]. The origin of z-axis denotes the objective focal plane. With the help of axial interference, 4Pi and MEANS could generate PSFs with 100 nm axial width, while the axial PSF width of confocal is 700nm. Parameters for simulation are: reflective index of medium n=1.5, objective numerical aperture NA=1.4, and wavelengths $\lambda_{ex} = 488\,\mathrm{nm}$, $\lambda_{dep} = 592\,\mathrm{nm}$. MEANS takes full advantage of the incident intensity through reflection, so its local maximum intensity is three times higher than conventional confocal microscopy and 1.5-times higher than 4Pi. Accordingly, almost two-fold resolution enhancement over conventional STED can be obtained for MEANS-STED as shown in (f).

electromagnetic fields for multiple imaging techniques (Figure 3.4). Theoretical derivations have been presented in Section 2.2.2: interference of the incident laser and the reflected laser generates a sectioning layer in the focal volume. When the mirror moves away from the focus, the reflected laser has a much lower intensity than the incident laser, so the interference pattern is not significant. Our simulation results of the electric field of MEANS microscopy reveals that MEANS (Figure 3.4(c)) could achieve more than three times local maximum intensity than conventional confocal microscopy (Figure 3.4(a)). Instead of dividing the laser into two beams as 4pi (Figure 3.4(b)), MEANS uses the interference of the incident and reflected laser; As a result, MEANS has higher excitation efficiency than 4pi.

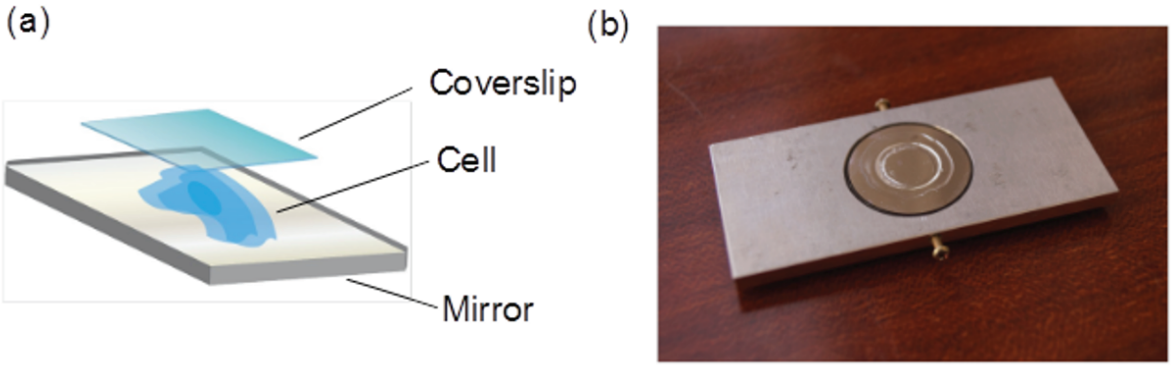

Figure 3.5: The structure of a MEANS specimen [105]. (a) Cells are grown on the top of a $50\,\mathrm{nm}$ silica-coated mirror, and under a coverslip. (b) A photograph of the cell sample loaded with a slide adapter.

3.3 Sample preparations

3.3.1 Mirror preparation

The first problem we need to address is to grow the cells on the mirror surface. The surface property is influential in the morphology of cell growth [120]. To avoid changing the cell behavior in our microscopy, we coated a protective SiO_2 above the first surface mirror (China Daheng Group). The thickness of the adjustable silica layer is around $100\,\mathrm{nm}$, so the cells could grow on it as on slides. After staining, the mirror is covered with a coverslip and sealed with nail polish. A home-made metal holder with the size of a microscope slide is used to hold the mirrors, adapting them to any conventional microscopes (Figure 3.5).

3.3.2 Cellular sample preparation

Our cells were cultivated by our collaborators from Georgia Institute of Technology following standard protocols [105]. Vero cells (ATCC CCL-81) were maintained in High Glucose DMEM (Lonza) with 10% FBS (Hyclone), 100 U ml-1 penicillin, and $100\,\mu\mathrm{g}$ ml-1 streptomycin (Invitrogen). hRSV strain A2 (ATCC VR-1544) was propagated in HEp-2 cells (ATCC CCL-23) at a titer of 1 x 106 pfu/mL. Cells were plated the day before infection at

25% confluency. Cells were infected by removing the media, washing with PBS (without Ca^{2+} and Mg^{2+}), adding virus at a multiplicity of infection (MOI) of 1, and incubating the cells for one h at $37\,^{\circ}C$. After adsorption, fresh medium was added to the inoculum. The cells are grown on top of a first-surface mirror, coated with a SiO_2 protective layer, so that the cell can grow on top of the SiO_2 layer.

Vero cells were fixed with either 4% paraformaldehyde in PBS for 10 min at room temperature and then permeabilized with 0.2% Triton X-100 (for nuclear pore complex staining) or fixed with 100% ice-cold methanol for 10 min at $-20\,^{\circ}C$ and then permeabilized with 100% ice-cold acetone for 2 min at $-20\,^{\circ}C$ (for microtubule staining). Nonspecific antibody binding was blocked with 5% bovine serum albumin (EMD) in PBS for 30 min at $37\,^{\circ}C$. Veros were then incubated with a primary antibody for 30 min at $37\,^{\circ}C$, washed twice in PBS, and incubated with a secondary antibody for 30 min at $37\,^{\circ}C$, washed twice in PBS, and mounted in a mixture of Mowiol 4-88 (Sigma) and DABCO (VWR) [121].

Primary antibodies used were rabbit anti-alpha tubulin (polyclonal IgG, Abcam catalog: ab18251) and mouse anti-NPC proteins that contain FXFG repeats (monoclonal IgG, Abcam catalog: ab24609). Secondary antibodies used were goat anti-rabbit DyLight 650 (Pierce) and donkey anti-mouse AlexaFluor 488 (Life Technologies).

3.3.3 Spin capture of RSV filaments on glass

To capture single hRSV filamentous virions on glass, hRSV A2 was propagated in HEp-2 cells at an MOI of 0.1. At 4 days p.i., the cell-associated and supernatant fractions were scraped, freeze-thawed, and spun through $5\,\mu m$ and $0.45\,\mu m$ pore-size centrifugal filters (Millipore) at $5.000\,\mu g$ and $4\,^{\circ}C$ for 4 min and 1 min, respectively. The fraction between $0.45\,\mu m$ and $5\,\mu m$ in diameter was collected and immobilized onto a poly-L-lysine (Sigma)-coated the first-surface mirror or cover glass by adsorption of $500\,\mu l$ of filtered virus for two hr at $4\,^{\circ}C$. The immobilized virions were fixed using 4% paraformaldehyde and immunostained according to the aforementioned protocol. Antibodies used were anti-

RSV F monoclonal (palivizumab, MedImmune) and anti-RSV N monoclonal (clone B023, Abcam). Coverslips were mounted in a mixture of Mowiol and DABCO (VWR) [121].

The MEANS-STED imaging was performed with a Leica TCS SP8 STED 3X system equipped with a white light laser as excitation, and 592 nm and 660 nm for STED depletion. The HyD detector and 100x oil-immersion objective (NA=1.4) were employed. Time-gated detection was also used [122], in which for AlexaFluor-488 the detection is delayed 0.5 ns, whereas for Cy5 (GE Lifesciences) the detection is delayed one ns.

3.4 Experiment results

3.4.1 Verification on the enhancement of sectioning

Direct measurement of the interference thickness is difficult for two reasons: first, the thickness of MEANS laser is below the optical diffraction limit, so it cannot be discriminated by an optical microscope. Second, this layer moves with the position of the mirror, so it cannot be measured by axially scanning the sample. One solution is to view MEANS as a simplified version of 4pi and measure the excitation layer thickness in 4pi, which gives a sectioning capacity of $\sim 100\,\mathrm{nm}$ [102]. However, we can also demonstrate the sectioning capacity of this system by using a phantom specimen. Inspired by a result from light sheet experiment (see Appendix A), we embedded 20 nm fluorescent beads into 1% agarose and evaluated the density of detected beads at different axial positions. The size of these beads is much smaller than the system point spread function so that they could be viewed as an ideal point fluorescence sources.

The beads are uniformly distributed in the sample, but it is found near the mirror surface its concentration is reduced. We plotted the curve of the signal to the background, and a 2-3 times enhancement of signal to background ratio is observed at the 13-14 $\mu\mathrm{m}$ layer close to the mirror surface. This indicates an enhancement of optical sectioning.

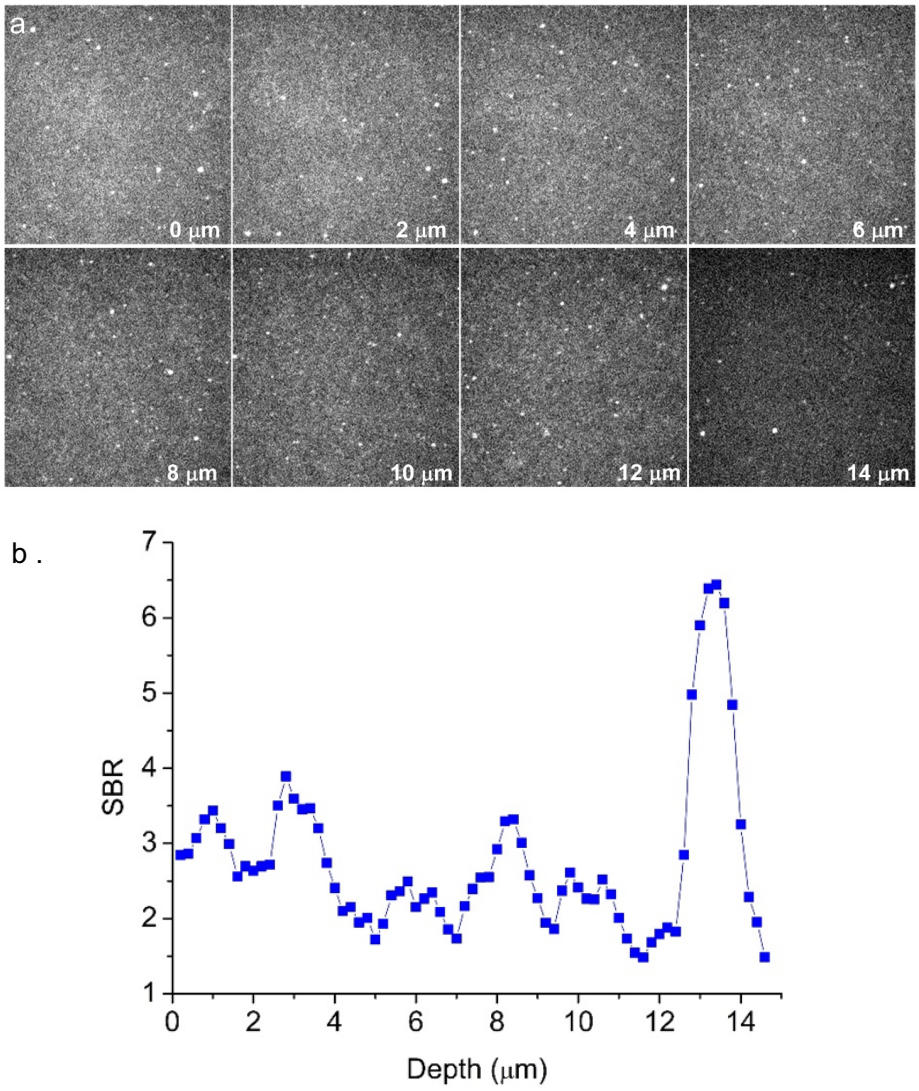

Figure 3.6: The depth imaging of 20 nm fluorescent beads in agarose [105]. (a) Images of fluorescent beads at different depths. Beads near the mirror position ($14\,\mu\mathrm{m}$) are detected with stronger intensity and lower density. (b) The signal to background ratio (SBR) is plotted with respect to the depth. The 3-fold SBR at the $13.5\,\mu\mathrm{m}$ layer indicates a much narrower excitation layer due to the MEANS interference.

3.4.2 MEANS confocal

Comparison of MEANS and TIRF microscopy

In this section we show MEANS is compatible with conventional sample preparation procedures, while Total Internal Reflection Fluorescence microscope (TIRF) has special requirements on the sample. TIRF is a type of microscopy in which ~ 100 nm thin structures could be resolved. By using evanescent wave on the glass boundary, it requires the immersion media of the sample have a different refractive index from glass. So only structures near the boundary could be resolved. Unfortunately, in a rigid sense, TIRF is not compatible with other imaging modalities because the refractive index mismatch may induce aberration. When the refractive index of the mounting medium matches the refractive index of glass, total reflection does not happen, and its sectioning capacity disappears.

Shown in Figure 3.7, we demonstrate a series of in-situ correlative images of "TIRF" and MEANS from a single Vero cell. While the layer near the coverslip can still be imaged by the TIRF mode of a microscope (Figure 3.7a), the MEANS imaging modality (Figure 3.4b) provides super-resolution information within an interior layer of the cells with $\sim$100 nm axial thickness. Near the nuclei of the cell, the microtubule network only exists near the coverglass surface and is captured, in this geometry, by MEANS microscopy. This indicates MEANS is more suitable for the study of structures together with other modalities.

MEANS Dual-color, spinning disk confocal and two-photon microscopy

In this section, we further demonstrate our MEANS microscopy could be easily used together with a variety of other modalities. First, we show MEANS-spinning disk microscopy in Figure 3.8. Image stacks are acquired by moving the objective toward the specimen. In layers from z=$0\,\mu\mathrm{m}$ to $1.5\,\mu\mathrm{m}$, structures on the focal plane are away from the mirror, and this is a region of conventional confocal. In this region, the reflected light intensity is below the incident laser intensity in the focal volume. As a result, effective interference cannot

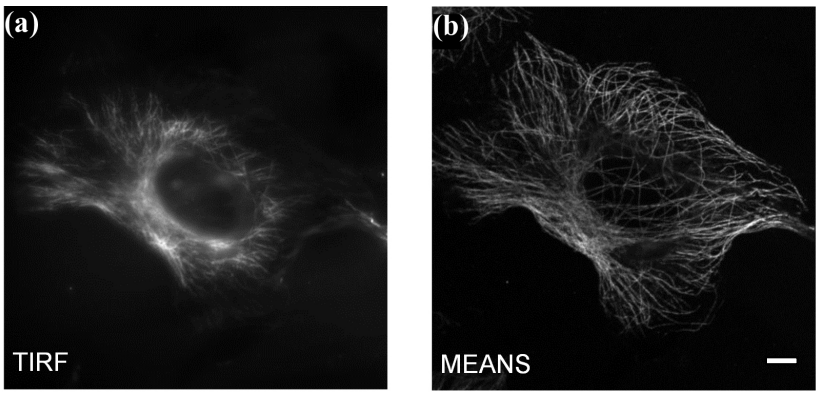

Figure 3.7: Compare of MEANS and TIRF modalities [105]. (a) "TIRF" and (b) microscopy imaging modalities. MEANS microscopy can be easily realized with a confocal microscope, while TIRF is typically not compatible with confocal samples, as shown in (a). The sample here is a Vero cell immunostained for tubulin using an AlexaFluor-488 secondary antibody. Scale bar: 10 µm.

occur. From z=2 µm to 2.5 µm a significant enhancement on signal level and contrast of the images could be observed. Further moving the mirror, we could observe the confocal images of the cell again.

It is shown in Reference [105] that our MEANS could also be applied into dual color microscopy and two-photon microscopy.

3.4.3 Changing the position of the MEANS layer

Moving the MEANS layer with different silica coating thicknesses

Usually, the position of the layer is dominated by the phase difference between the incident laser field and the reflected laser field, so it keeps the same height away from the mirror surface, as shown in Figure 3.8. Assuming the distance from the MEANS layer to the cell-silicon boundary is h_1, from the MEANS layer to the mirror surface is h_0, and from the cell-silicon boundary to the mirror surface is h_2, we have $h_0 = h_1 + h_2$. Since h_0 is fixed, we can change h_2 to alter the height of MEANS layer in cell h_1. To show the possibility of imaging at different depths into a cell, we grew COS-7 cells on mirrors coated with different thickness of silica coating. Figure 5 in Reference [105] shows different structures

are revealed in optical sectioning layers of actin filaments within the COS-7 cell, achieved by changing the thickness of the silica coating from 50 nm, 100 nm, 150 nm and 200 nm. We stained actin microfilaments, one type of cytoskeletal element responsible for the cell shape and cell motility. When the thickness of the spacer is small, top layers of cells are excited, which is rich in actin filaments and bundles; when the thickness of spacer increases, bottom parts of cells are excited, in which we can distinguish the position of nuclei in cells.

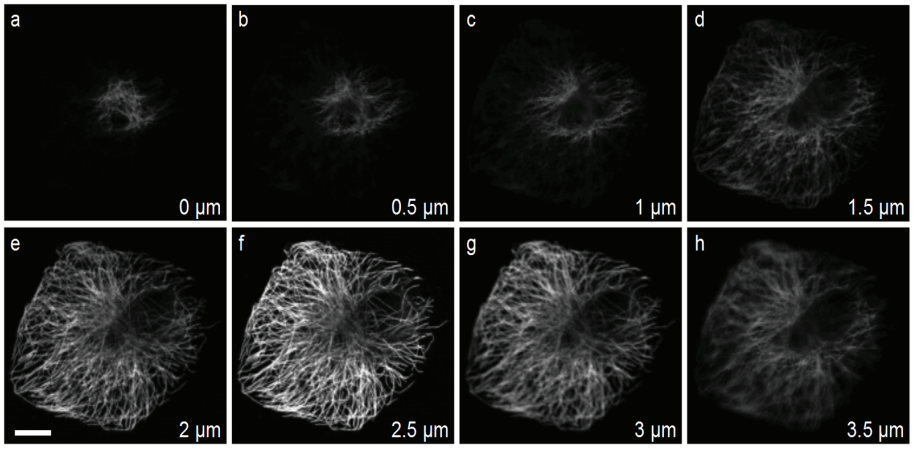

Figure 3.8: Image z-stacks of MEANS-confocal microscopy (Olympus FV-1200, with an apochromatic 60x, oil-immersion objective, NA=1.42) [105]. Images are taken with $0.5\,\mu\mathrm{m}$ interval from the top surface towards the mirror substrate. When the mirror is away from the objective focal plane, as shown in (a)-(d), the reflected laser intensity is smaller than the incident laser intensity and their superposition yields conventional confocal images. (e)-(g) show MEANS results. Almost the same layer of the cell is imaged in all stacks, but its signal to background ratio reaches maximum at $3.5\,\mu\mathrm{m}$ from the top, when the interfered maximum overlaps with the objective focal plane. Scale bar, $10\,\mu\mathrm{m}$.

Moving the MEANS layer with different wavelengths

Since the distance between the mirror and the MEANS enhanced layer is linearly proportional to the excitation wavelength, we also explored the method of changing the MEANS layer position through excitation wavelength modulation. Fluorescent nanodiamonds with nitrogen vacancy centers inside have broad absorption spectrum. They are observed under a laser scanning confocal system (Leica TCS SP8) equipped with a white light laser and plan-apochromatic objective (Leica HC PL APO CS2, 63X/1.40 OIL). As shown in Figure

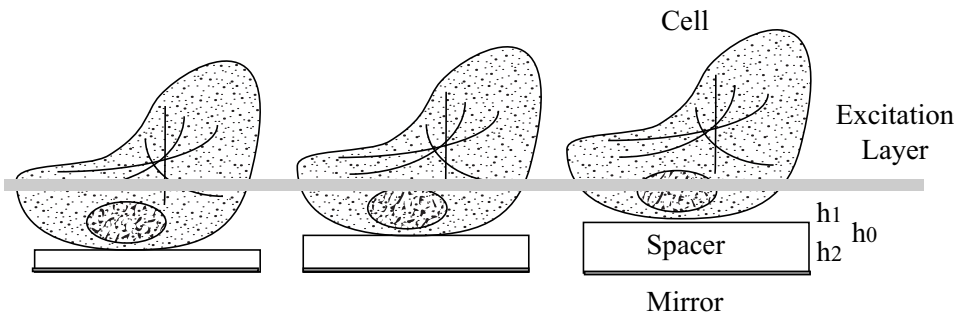

Figure 3.9: By adjusting the spacer thickness we can obtain the cross-sectional imaging of different layers in the cell specimen. h_0 is the distance from the excitation layer to the mirror surface, h_1 is the distance from the excitation layer to the spacer surface, and h_2 is the thickness of the spacer. For MEANS constructive interference, the maximum spacer thickness is 100-150 nm.

3.10, different colors represent different excitation wavelengths. Beads in different layers have different colors, indicating the excitation layer position changes with the wavelength.

3.4.4 MEANS-STED microscopy of NPCs and viral filaments

Two important properties of MEANS inspire us to apply it in STED: first, the excitation is sectioned into 100 nm layers. If the out of focus structure is not illuminated at all, the background could be surpassed, so that we can resolve very fine structures in the focal plane. Second, the depletion intensity could be significantly enhanced. For depletion, the spatial electric fields come from the superposition of both the incident filed and the reflected field. A coherent interference would result in a four times enhancement in light intensity while an incoherent interference could contribute two times enhancement. Since the resolution of STED is dependent on the depletion intensity, which can be written as [123]

$$d = \frac{\lambda}{2NA} \frac{1}{\sqrt{1 + I_{dep}/I_{sat}}} \tag{3.2}$$

where I_{dep} is the depletion intensity, and I_{sat} is the saturation intensity of the molecule, the constructive interference in MEANS-STED mode provides 1.5-2 times resolution enhancement over conventional STED. According to our previous discussion in Chapter 2,

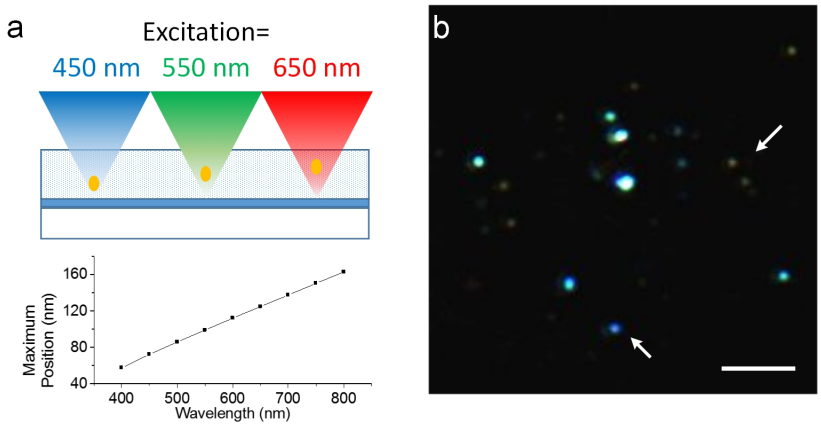

Figure 3.10: Imaging nanodiamond particles embedded in agarose with different excitation wavelengths [105]. The nanodiamond particles are excited by 470-490 nm, 550-570 nm, and 650-670 nm lasers, and each wavelengths are represented by B, G, and R colors, respectively. The fluorescence particles indicated by arrows show beads with different colors, indicating different depths differentiated by MEANS-excitation. Scale bar, $5\,\mu\mathrm{m}$.

the depletion power could be lower.

To verify our MEANS method in STED nanoscopy, we applied the MEANS approach on a commercial Leica TCS SP8 STED 3X super-resolution microscope. As a result of the MEANS assisted STED (Figure 3.11 a-d), we have already achieved 19 nm resolution in the observation of pore complex (NPC) using a relatively low 592-nm depletion laser power of 60 mW measured at the back aperture of the objective.

We used MEANS to resolve ring structures in nuclear pore complexes, which are composed of three concentric rings nucleoporins (Nups) held together by linker proteins. The inner channel is composed of the phenylalanine-glycine (FG) Nups [124]. The ring structure results in Figure 3.11 could be the result of the ring structures in NPC.

We also used MEANS to visualize the sub-micron hollow structures in Human respiratory syncytial virus (hRSV) virons. hRSV produces filamentous virions that are 100-200 nm in diameter and up to several microns in length. The distance between the centroid of the fusion (F) proteins measured as 120 nm by dSTORM [125]. We immunofluorescently stained the F protein, which is in the virion membrane, and the nucleoprotein (N), which is bound to the genomic RNA inside the virion space. With the MEANS implementation, a

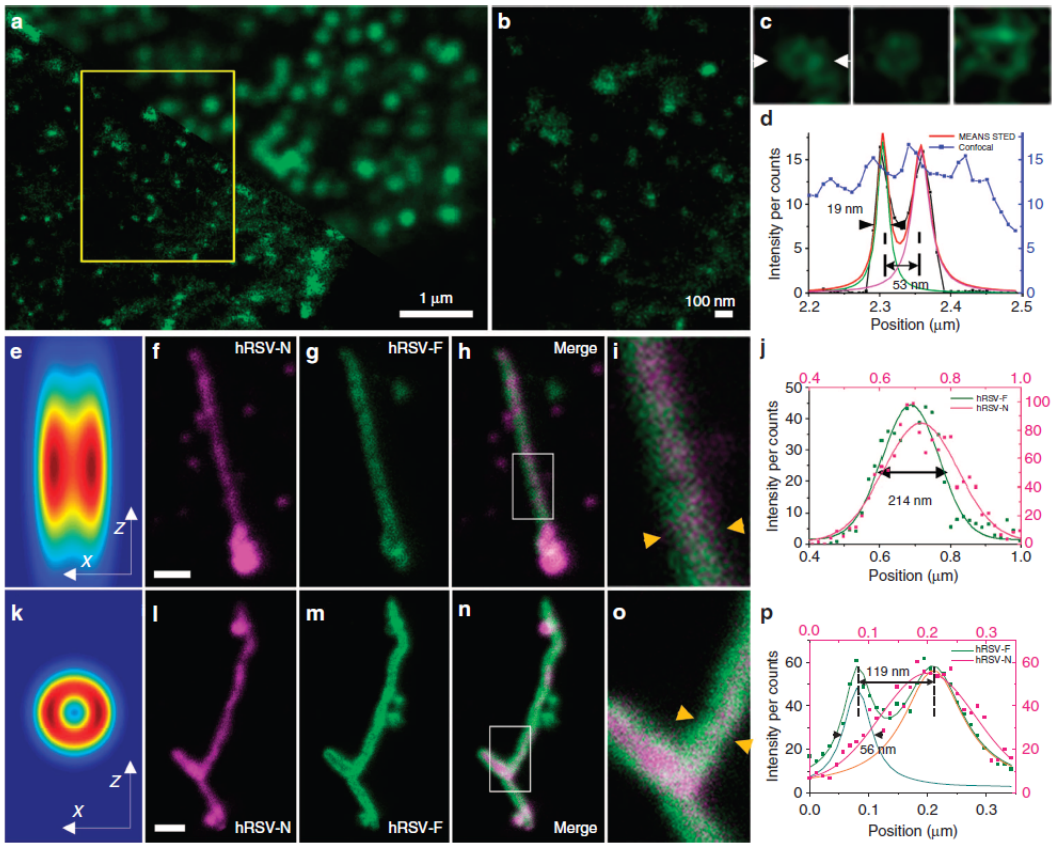

Figure 3.11: NPCs of Vero cells and hRSV viral filaments imaging via conventional STED and MEANS-STED. (a)-(d) are NPCs of Vero cells. (a) shows the compare of confocal (a: upper right) and MEANS-STED (a: lower bottom) modalities. (b) is the magnification of the boxed area in (a), In (c) three individual NPCs are magnified, and their intensity distributions are plotted in (d). Two NPCs with a distance of 53 nm could be separated by MEANS-STED. (e)-(p) are images of hRSV viral filaments: (f)-(h) are taken from conventional STED. (i) is a magnification of the boxed area in (h), and its intensity distribution is plotted in (j). hRSV-N and hRSV-F cannot be distinguished by conventional STED, because the filament structure in (k) is convoluted by an elongated PSF as shown in (e). On the other hand, with the help of axially narrowed PSF, MEANS-STED could distinguish the difference between hRSV-N and hRSV-F, as shown in (i)-(p). Gaussian fitting of the data in j only shows one slope with a width of 214 nm, whereas the fitting in p indicates that the width of the hRSV-F is $\sim$56 nm, and the distance between the split peaks is $\sim$119 nm. Scale bar=500 nm in (f, l) [105].

thin section in the middle of the filament is excited, and the top and bottom of the filament are not excited, allowing us to resolve the F proteins on opposing sides of the viral envelope with the N protein in the center.

3.5 Conclusions and discussions

In this chapter, we introduce the mirror enhanced axial narrowing microscopy to enhance the axial resolution of the point-scanning microscopy. It is much simpler compared to previous interference axial-superresolution microscopy, and compatible with conventional sample preparation procedures compared to TIRF. We also demonstrated that this method could be combined with other modalities like spinning disk confocal, multi-color confocal, two-photon confocal microscopy and STED. This method could be broadly applicable to other optical systems requiring PSF engineering, including the pulsed or time-gated STED [122], RESOLFT [74], ground state depletion, excitation state absorption, saturation [126], optical data storage [127], upconversion [128], charge state depletion [129], etc.

CHAPTER 4
BEYOND FLUORESCENCE: SCHLIEREN CONFOCAL, A PHASE CONTRAST MODULE ON SCANNING MICROSCOPY

In previous chapters, it is pointed out that the point-scanning microscopy has an intrinsic sectioning capacity because only the detection point is excited, so it is popular in fluorescence imaging. However, the point detector used in point scanning microscopy is not compatible with most other imaging modalities like phase contrast microscopy, so an additional 2D detector has to be added into the system, which further induces system complexity. In this chapter, we introduce a simple quantitative point scanning phase detection scheme, Schlieren confocal microscopy(S-confocal) or Laser Oblique Scanning Optical Microscopy (LOSOM), which is fully compatible with the previous point-scanning fluorescence sectioning microscopy. Section 4.2-4.4 has been published in Reference [130].

4.1 Introduction and previous work

This chapter we focus on phase objects, which are transparent samples with no light absorption. Under conventional microscopes, these samples are hard to be observed due to the lack of contrast. We propose a point-scanning based phase contrast microscopy, Schlieren confocal microscopy, named after Schlieren photography [131, 132, 133], which uses partially blocked detection to obtain the phase information. First, we have a review on phase contrast microscopy in history.

4.1.1 Phase contrast microscopy

The first phase contrast microscopywas developed by Zernike in 1942 [134], and he was awarded the Nobel Prize in Physics in 1953.

The principle of phase contrast microscopy is shown in Figure 4.1: An annular aperture

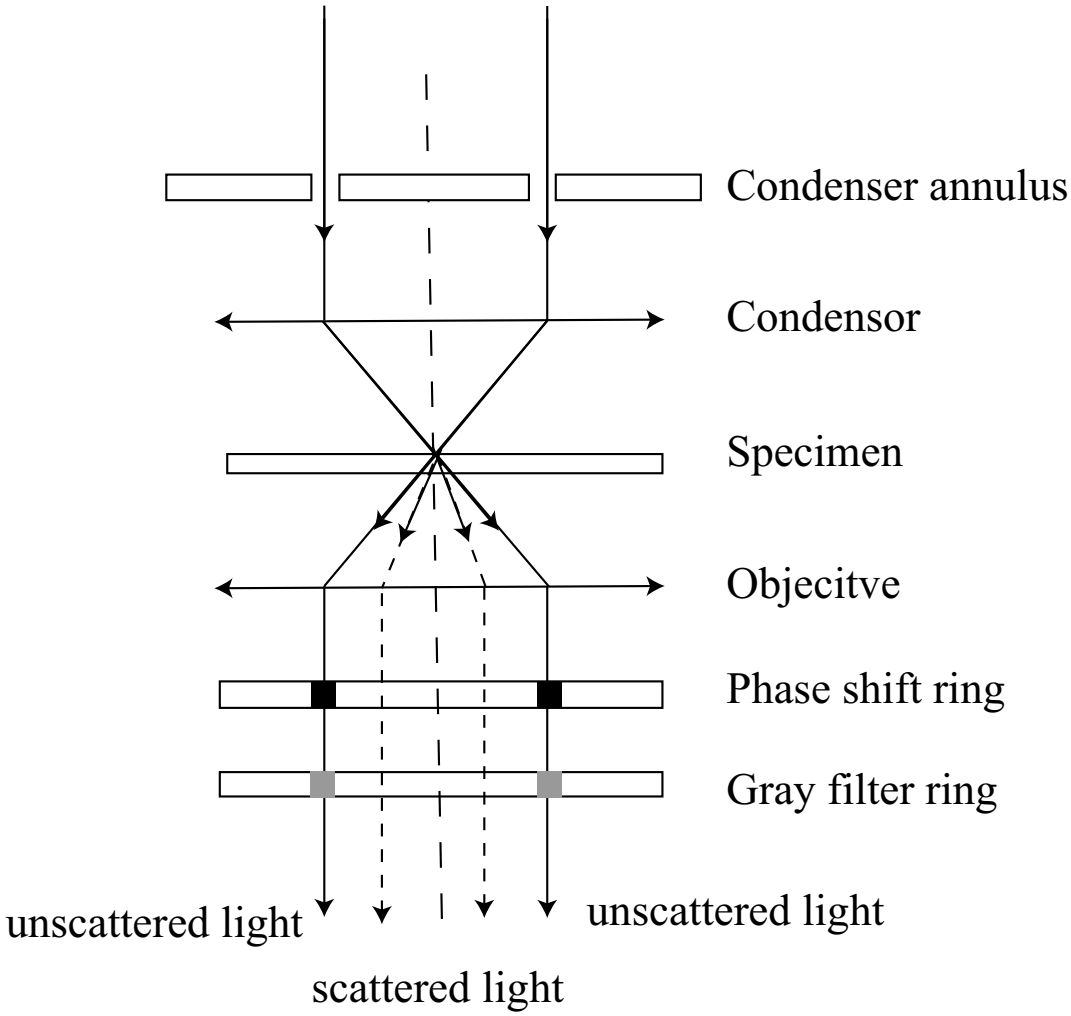

Figure 4.1: Phase contrast microscopy [135].

is put on the front focal plane of the condenser, and a phase plate is put on the back focal plane of the objective. For unscattered light that passes the sample, an additional $\lambda/4$ optical path difference imposes a phase shift of $\pi/4$. Further, a gray filter ring is used to match the intensity of the background light and the diffracted light. These two components will interfere at the image plane; As is shown in Figure 4.1, if there is no phase shift in the sample, the sample will have a similar intensity as the background; if the sample has a $\pi/2$ phase difference, sample intensity will change due to constructive or destructive interference.

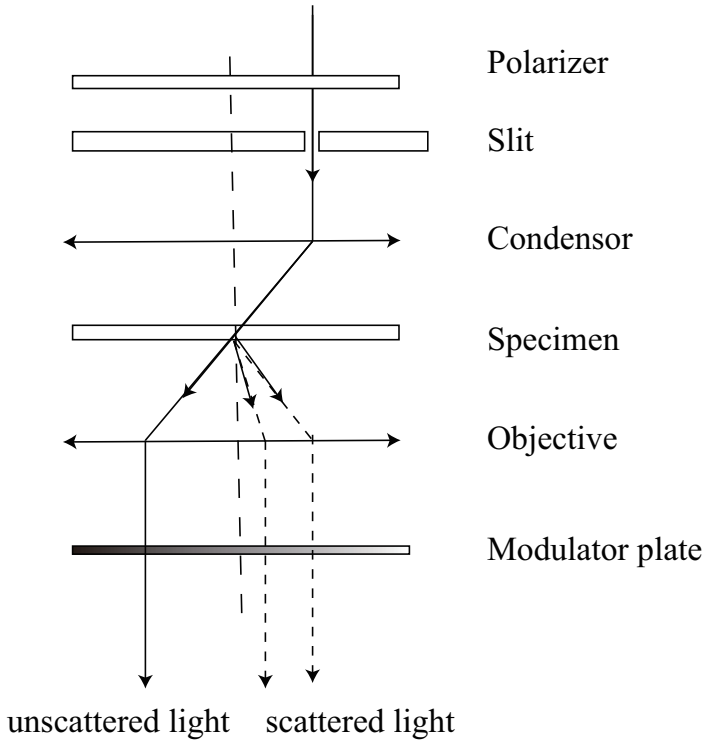

Figure 4.2: Hoffman modulation contrast microscopy [135].

4.1.2 Hoffman modulation contrast microscopy

Hoffman modulation phase contrast microscopy is based on a similar principle. But instead of phase modulation, this method uses the modulation of the transmission rate, as shown in Figure 4.2. The background light is attenuated by a factor of 1%. The low order diffraction components are attenuated by a factor of 15%, while the high order diffraction components are attenuated by a factor of 85%. Again they interfere on the image plane, and the final image intensity reflects the phase of the sample. This method is not quantitative.

4.1.3 Differential interference contrast microscopy

Differential interference contrast microscopy [136, 137, 138] is still a widely used phase imaging technique today. The image formation process could be described in Figure 4.3:

1. An unpolarized light beam passes a polarizer, and the polarization became 45 degree.

2. This light beam is separated into two orthogonally polarized beams by a Wollaston

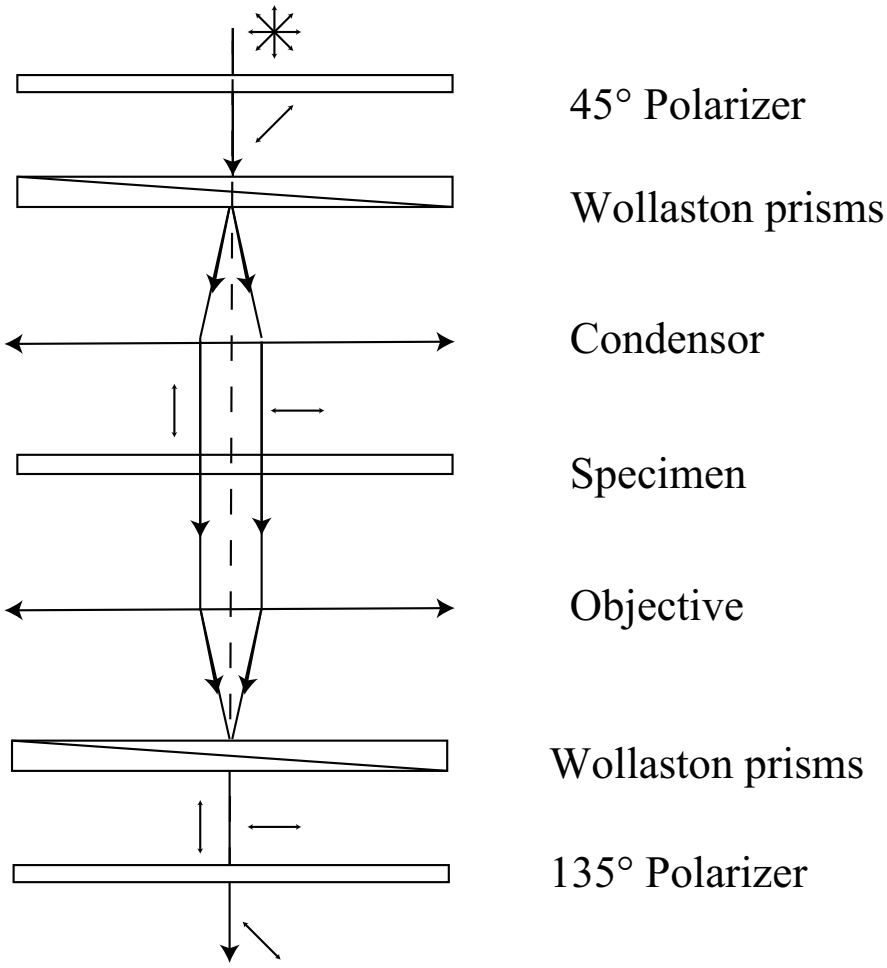

Figure 4.3: Differential Contrast microscopy [135].

prism. These two beams have a small angle with respect to each other.

3. After the condenser these two beams incident on two different positions on the sample, with their phase shifted by the sample.

4. Then they are collimated by the objective and realigned by a second Wollaston prism.

5. A second polarizer oriented at 135 degree is used to form the interference of these two beams.

The limitation of this method is it could not be used on samples with polarization effect.

4.1.4 Modern digital phase contrast microscopy

There are also modern phase microscopy techniques like diffraction phase microscopy [139] and spiral phase contrast microscopy [140], which use a spatial light modulator to modulate the sample frequency information in the Fourier domain. They are all methods based on wide field microscopy.

4.2 Principle of S-confocal

We propose a point-scanning based phase contrast microscopy. Our setup shown in Figure 4.4(a) consists of a standard confocal microscopy. To form an S-confocal system, we place a fluorescence plate above the specimen. The key component introduced is a beam obstructor placed in front of the confocal collection lens to partially block the fluoresce. The incident laser is focused by the objective, and its direction is altered by the phase of the specimen, as shown in Figure 4.4(b). Then it incidents on the fluorescence plate and generates fluorescent irradiance as a secondary incoherent light source. The fluorescence travels through the specimen, refracted again, partially blocked by the obstructor, and focused by the collecting lens on the confocal pinhole. The spatially shifted excitation can generate detectable fluorescence signal, whose change is proportional to the phase gradient of the specimen. As can be seen from the theoretical analysis and the experiments, when a small pinhole is used, both excitation and detection can be effectively shifted, resulting in dual modulation; yet when a relatively large pinhole is used, the phase gradient in the detection focal region is averaged, resulting in a linear modulation sensitive to the local excitation phase gradient.

4.3 Quantitative analyses

Without loss of generality, a 2-dimensional system with piezo stage scanning is analyzed here for simplicity. First we investigate the intensity of fluorescence excitation. We use

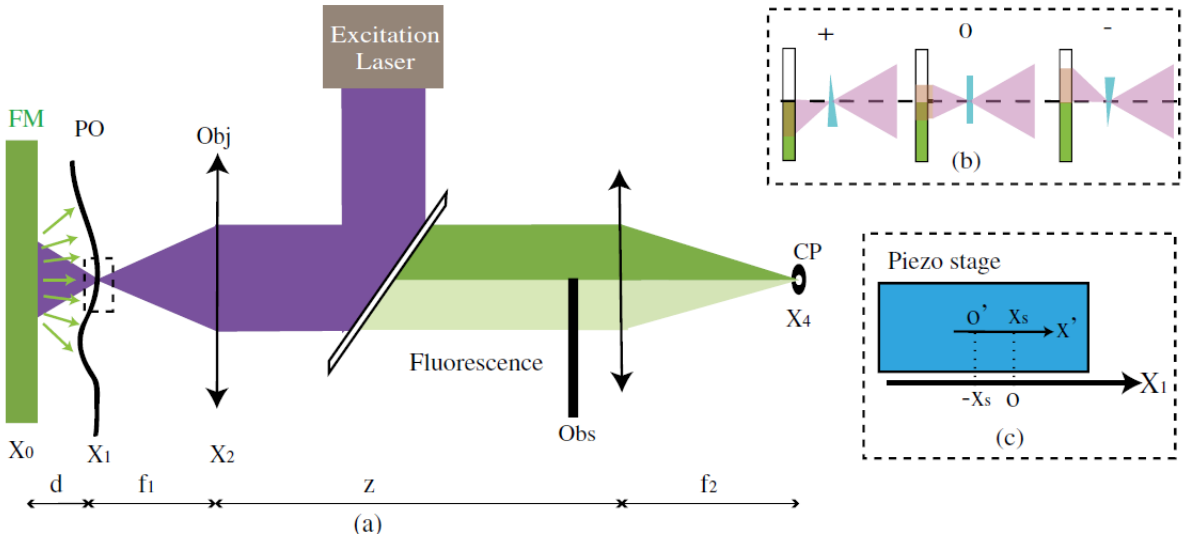

Figure 4.4: Schematic diagram of S-confocal [130]. (a) S-confocal is based on a CLSM, except for a fluorescent plate placing above the specimen, and a block in front of the fluorescence collection. FM: fluorescent medium, PO: phase object, CP: confocal pinhole, Obj: objective lens, TL: tube lens, SL: scan lens, Obs: obstruction, DM: dichroic mirror. Fluorescence illuminates the whole sample, but only the optical rays go through the neighborhood of scanning point could be detected. (b) Coordination on the piezo stage. O is the laboratory frame, and O' is a moving frame on the sample. The coordination of the scanning point in the sample frame is x_s. (c) The phase gradient of the specimen acts as a micro-prism to effectively deflect the incident/fluorescent beams. Here only incident laser beam is drawn.

Kirchhoff theory to prove the illuminated area is determined by the sample phase gradient on focal point [31]. The excitation system is similar to a typical scanning transmission electron microscope, whose detection intensity on the fluorescence plate plane can be written as [141]

$$U(x_0, x_s) = U_0 \int_{-\infty}^{+\infty} h(x_1) t(x_1 + x_s) \exp \frac{\mathrm{i}kx_0x_1}{d} \mathrm{d}x_1, \tag{4.1}$$

where $t(x')$ is the transmission rate of the specimen in the specimen coordination x', x_1 is the laboratory coordinate with respect to the scanning point, and x_s represents the scan position in the specimen coordination. The coordination we use is shown in Figure 4.4(a) and we have $x' = x_1 + x_s$. $h(x_1)$ is the laser incident point spread function (PSF) on the sample, given by $h(x_1) = \int_{-\infty}^{\infty} P(x_2) \exp \frac{\mathrm{i}kx_1x_2}{f} \mathrm{d}x_2$, where f is the focal length of the objective and $P(x_2) = \xi(x_2/a)$ is the effective aperture function of the objective lens. Here a is the laser radius on the lens and ξ is the rectangle function $\xi(x) = 1$ if $|x| < 1$; otherwise $\xi(x) = 0$. Dropping the pre-multiplying constants, this gives $h(x_1) = \mathrm{sinc}(kx_1a/f)$. We assume the transmission rate of the phase object can be written as $t(x_1 + x_s) = \exp\{\mathrm{i}\phi(x_1 + x_s)\}$, where $\phi(x')$ is the additional phase function in the specimen coordination x'. Since in a confocal system laser is focused on the image point, we expand the phase function into Taylor series, with only two leading orders remained: $t(x_1 + x_s) = \exp\{\mathrm{i}\phi(x_s) + \mathrm{i}kg(x_s)x_1\}$, where $g(x_s)$ is the local phase gradient of the scanning point: $g(x_s) = \frac{1}{k} \frac{\mathrm{d}\phi(x_s)}{\mathrm{d}x_s}$. Substituting expression of $h(x_1)$ and $t(x')$ into Equation 4.1, we derive $U(x_0, x_s) = U_0 \xi(\frac{g(x_s) + x_0/d}{a/f})$. It has a straightforward physical interpretation: light is refracted by the local phase gradient as a micro prism (see Figure 4.4(b)). Since the fluorescence excitation is proportional to the incident laser intensity, its intensity can be written as

$$I_f(x_0, x_s) = I_{f0} \xi(\frac{g(x_s) + x_0/d}{a/f}). \tag{4.2}$$

Under paraxial approximation, each isotropic excited point has an equal contribution to the detected intensity; but since only the optical rays go through the neighborhood of scanning point could be detected, the obstruction makes some of the fluorescence points invisible to the pinhole. If the refracted angle by the sample is $g(x_d) = \frac{1}{k}\frac{\mathrm{d}\phi(x_d)}{\mathrm{d}x_d}$ where x_d is the detection point, detection intensity can be derived as:

$$I_{det}(x_s, x_d) = \int_{-\infty}^{\infty} I_f(x_0, x_s)\eta(-g(x_d)d - x_0)\mathrm{d}x_0, \tag{4.3}$$

where $\eta(x) = 1$ if $x > 0$ and $\eta(x) = 0$ if $x < 0$, and x_4 is the image of x_d. For simplicity, we assume the edge of obstruction is on the optical axis, so that half of the fluorescence is blocked. Finally, image intensity is the sum of all the detection points:

$$I_{det}(x_s, x_d) = \int_{-\infty}^{\infty} I_f(x_0, x_s)\eta(-\bar{g}(x_d) - x_0)\mathrm{d}x_0. \tag{4.4}$$

where $\bar{g}(x_d)$ is the average gradient of the detection area corresponding to the pinhole size. If the detection area is relatively large in a large pinhole confocal case, the local gradient would be smoothed and averaged. The effect of $\bar{g}(x_d)$ in Equation 4.4 would be insignificant compared to $\bar{g}(x_d)$ in Equation 4.2. Consequently, image intensity would be dominated by the sample phase gradient of the laser incident focal point:

$$I_{det}(x_s) = I_0(1 + \frac{1}{ka/f}\frac{\mathrm{d}\phi(x_s)}{\mathrm{d}x_s}). \tag{4.5}$$

4.4 Experiments

4.4.1 Validation of the theory

We have experimentally validated our theory. An inverted microscope (Ti-U, Nikon, Japan) with an objective of 10X (NA=0.3) is employed as the platform of a home-built CLSM. A

375 nm UV laser (RGB Lase) is used for excitation. A piece of white printing paper or fluorescence plate (Chroma) is used as the fluorescence medium placed above the specimen. The laser is reflected by a dichroic mirror (Chroma). A pair of galvanometers (Nutfield) is used for raster scanning in CLSM. Then the incidence is focused by the scan lens (f=50 mm), expanded by the tube lens, and collimated by the objective of the microscope. It focuses on the specimen, illuminates the fluorescence media, and excites fluorescence. The fluorescence then travels through the specimen, de-scanned by the galvanometers, passes the dichroic mirror and the filter, and then the light is converged by an eyepiece (f=22 mm). There are two 4f systems in the optical beam path: one 10X magnification microscope consists of the objective and tube lens, whereas the other 1/2X microscope consists of the scan lens and the collecting lens. Consequently, 1 Airy Unit (with a wavelength of about $0.4\,\mu\mathrm{m}$) corresponds to $20\,\mu\mathrm{m}$ on the detector for our system.

First, we show the effect of the incident refraction. We used a grating with period of $40\,\mu\mathrm{m}$ and height of $1\,\mu\mathrm{m}$ as the sample. In Figure 4.5(b)-(d), a multi-mode fiber is used as the confocal pinhole (diameter $200\,\mu\mathrm{m}$, corresponding to 10 AU). UV laser and fluorescence medium shown in Figure 4.5(a) are employed as illumination. Image of grating is showed in Figure 4.5: (b) is its S-confocal image without extra block, where the dark stripes result from finite aperture of lens; (c) is the upside block result, where the rising edges become bright, and falling edges become dark; (d) is the downside block result which shows opposite shadowing direction of Figure 4.5 (b). The cracks and dusts on the grating can be clearly visualized in different shadowing effects in Figure 4.5(c)-(d). According to Equation 4.5, with such a large pinhole, the detection gradient signal is smoothed and vanish, and the resulted intensity only depends on the incident gradient, so in Figure 4.5(b)-(d) the image is very sharp. We call it Type 1 S-confocal. These results show S-confocal intensity gives the first derivation of the sample, and the direction of shade depends on the direction of obstruction. Fig. 4.5 (k) shows the grating profile (green dash and dots), grating gradient (red dashes), and the measured image gradient. As can be seen, the image gradient match-

es well with the sample gradient, which implies that this technique has the potential to be applied for quantitative phase retrieval. Then the effect of refraction could be observed in Figure 4.5(e)-(g). When the sample is illuminated with wide-field illumination, the resulting image is heavily blurred, as shown in (e)-(g). These three images are taken under the same block and detection conditions as (e)-(g), but with Köehler illumination as shown in Figure 4.5(a).

Then in Figure 4.5(e)-(j), we show the final image is the superposition of incident and detection gradients. When a much smaller confocal pinhole is used with laser and fluorescence medium, blocking the detection beam can generate dual-mask imaging result. In this case, we used a fiber with a diameter of $60\,\mu\mathrm{m}$, which is corresponding to 3 AU. Since the detection area is now comparable to the excitation area, resulted images have both contributions of Equation 4.2 and Equation 4.3. Figure 4.5(e)-(g) show the effect of detection gradient when the sample is illuminated by wide-field Köehler illumination with a tungsten-halogen lamp. These images are blurred because the spatial extent of fiber diameter is about the size of the phase edge. In (h)-(j) laser scanning images are provided. Clearly two different sets of stripes with defects are present in images, resulted from incident gradients as in Figure 4.5(b)-(d) and detection gradients in Figure 4.5(e)-(g).

4.4.2 Co-localized fluorescence confocal and S-confocal microscopy

Finally, we demonstrate the application of S-confocal in a biological sample. We used a mouse kidney slide (F-24630, Invitrogen) and $200\,\mu\mathrm{m}$ fiber as confocal pinhole (10 AU). Its S-confocal image, the fluorescence image and merged image of both modalities are shown in Figure 4.6. As the nuclei have a slightly higher refractive index over the surrounding tissue [142], it shows as small pits in Figure 4.6(a). These pits match well with the blue spots in Figure 4.6(b) and (c), indicating that S-confocal is very sensitive in detecting the change of refractive index, or the phase gradient. Moreover, S-confocal image and fluorescence image mode could be switched conveniently if we take away the top fluoresces medium

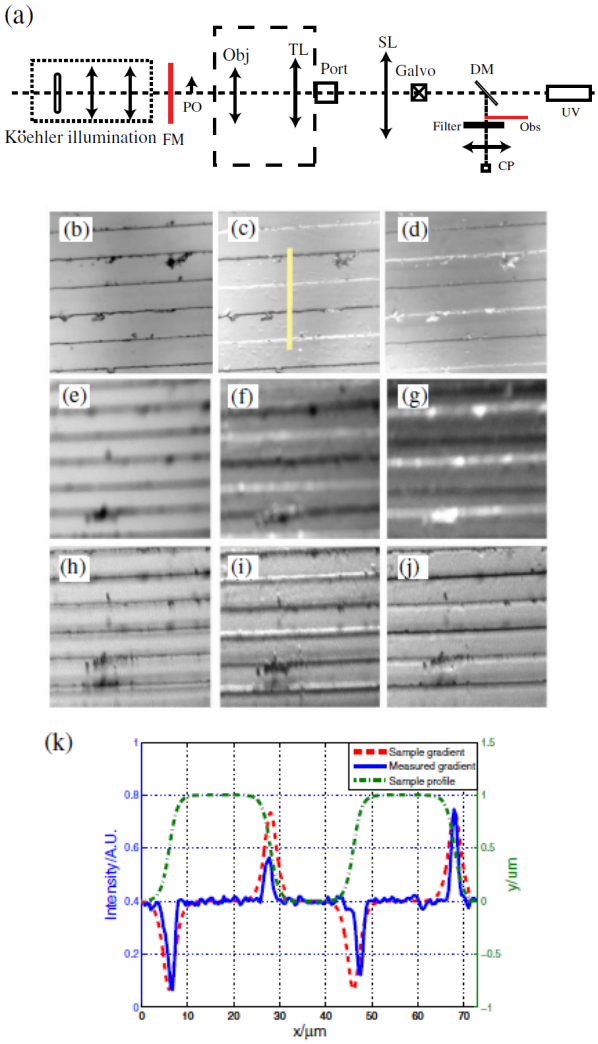

Figure 4.5: (a) is the system we used to illustrate the effect of incident and detection gradient. (b)-(d) show the S-confocal image with UV laser incident, fluorescence medium on top and pinhole of 10 AU. The obstruction direction determines the orientation of the shade effect. Image intensity indicates the incident gradient since the detection gradient is averaged. (e)-(g) are scanning images with Köehler illumination with 3 AU pinhole but without laser and fluorescence medium, and (h)-(j) show the S-confocal image with a pinhole of 3 AU. Thereby the intensity in (h)-(j) is contributed by both the incident gradient as of (b)-(d), and the detection gradient as of (f)-(h). Left, middle and right columns are images without obstruction, upside obstruction and downside obstruction, respectively. The image size is $120\,\mu\mathrm{m} \times 120\,\mu\mathrm{m}$. (k) Grating profile (green dash and dots), grating gradient (red dashed) and measured gradient (blue solid) along yellow line in Fig. (c) [130].

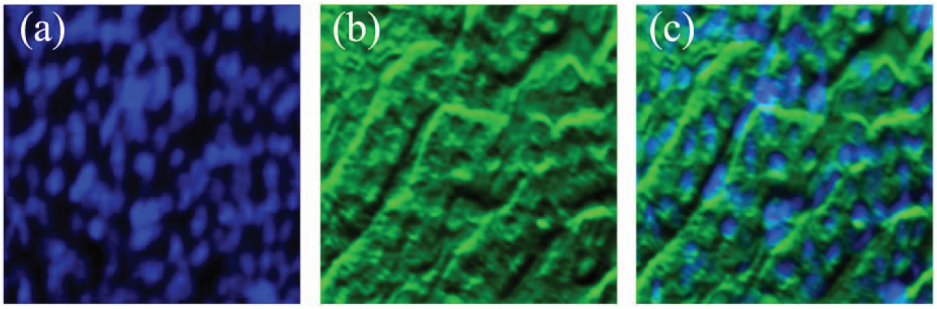

Figure 4.6: (a) Fluorescence image of mouse kidney (DAPI stained), (b)Phase relief image of mouse kidney by S-confocal, and (c) merged image [130]. The image size is $180\,\mu\mathrm{m} \times 180\,\mu\mathrm{m}$.

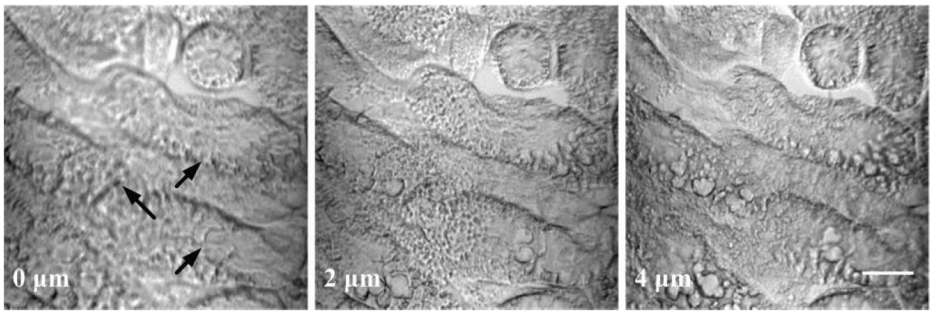

Figure 4.7: A series of optical sections of the mouse kidney taken at $2\,\mu\mathrm{m}$ intervals [143]. Scale bar: $30\,\mu\mathrm{m}$.

and block. Both structure and component information could be obtained from the merged image.

4.4.3 Axial scan

In Figure 4.7 we show a series of optical sections of the mouse kidney, which indicates the optical sectioning effect.

4.4.4 In-vivo applications

Ding et al. have used this technique to observe the microcirculation system in the mesentery of the rat model. Utilizing a localized point-scanning detection scheme, high-contrast images of leukocytes were obtained [144]. This work shows that our method has the potential for clinical diagnosis.

4.5 Type 2 S-confocal microscopy

Our previous analyses are based on the assumption that the incident laser does not fill the aperture of the objective. Then the resolution of the system would be lower than the diffraction limit. Since the detected signal is proportional to the overlap between the excitation zone and the detection zone as shown in Figure 4.4(b), we can use a partial fluorescent medium, with only the green area being fluorescent, to generate the same effect without any obstruction. We call it Type 2 S-confocal.

The Type 2 S-confocal does not need any modification to the confocal optics, and the pinhole size could be as small as 1 AU. So the resolution and the sectioning capacity of confocal fully remain. The analytical relationship between the phase gradient and the intensity, as shown in Figure 4.8, could be written as:

$$I(\vec{r}) = I_0 \int_{-\infty}^{\frac{1}{k\alpha}\frac{\partial\phi(\vec{r})}{\partial x}} \exp(-x^2)\mathrm{d}x \tag{4.6}$$

If we consider the background I_b may vary and define $\mathrm{erf}(x) = \frac{2}{\sqrt{\pi}}\int_0^x \exp(-x^2)\mathrm{d}x$, we have

$$I(\vec{r}) = I_b + I_0\mathrm{erf}(\frac{1}{k\alpha}\frac{\partial\phi(\vec{r})}{\partial x_i}) \tag{4.7}$$

Here $\alpha = a/f$ if the laser fills the aperture and $x_i = x$ or $x_i = y$ depends on the orientation of the phase plate. Here I_b, I_0 and α could be calibrated using standard phase samples. Two directional phase derivations $\partial\phi/\partial x$ and $\partial\phi/\partial y$ could be measured sequentially with rotation of the phase plate or simultaneously with phase plates of two different kinds of fluorophores, and then they could be separated from spectrum. Then the phase of the object could be reconstructed from these two measurements. If four types of fluorophores are used or four independent measurements are taken, this method could even be used to

measure the transmission rate of sample $t(\vec{r})$

$$I(\vec{r}) = t^2(\vec{r})[I_b + I_0 \mathrm{erf}(\frac{1}{k\alpha}\frac{\partial\phi(\vec{r})}{\partial x_i})] \tag{4.8}$$

With this method we have measured the phase gradient in a phantom sample and achieved similar results as shown in Figure 4.5.

4.6 Conclusions and discussions

In conclusion, we propose a method to achieve phase edge enhancement based on partial obstruction of CSLM, which can be readily adapted to current confocal setups. With only one fluorescent medium and one partial beam obstructor introduced, the fluorescent illumination is compatible with fluorescence labeled specimens and can obtain multi-modality fluorescence/structure images within a single system. An imaging mechanism is found that in S-confocal, the incident laser is refracted by local phase gradient, and the resulted partially illuminated fluorescence forms a phase relief image. The final intensity of the image is contributed by both incident and detection phase gradient modulation. A linear relationship between the local phase gradient and the detected intensity is found in both Type 1 S-confocal and Type 2 S-confocal, implying this method has the potential for quantitative phase imaging. Type 1 S-confocal has the advantage of high signal to noise ratio, while Type 2 has better resolution. The scope of phase in our system is $-kNA < d\phi/dx < kNA$. With an estimated resolution of $\lambda/2NA$, it requires the phase difference in the resolution region to be no more than 2π.

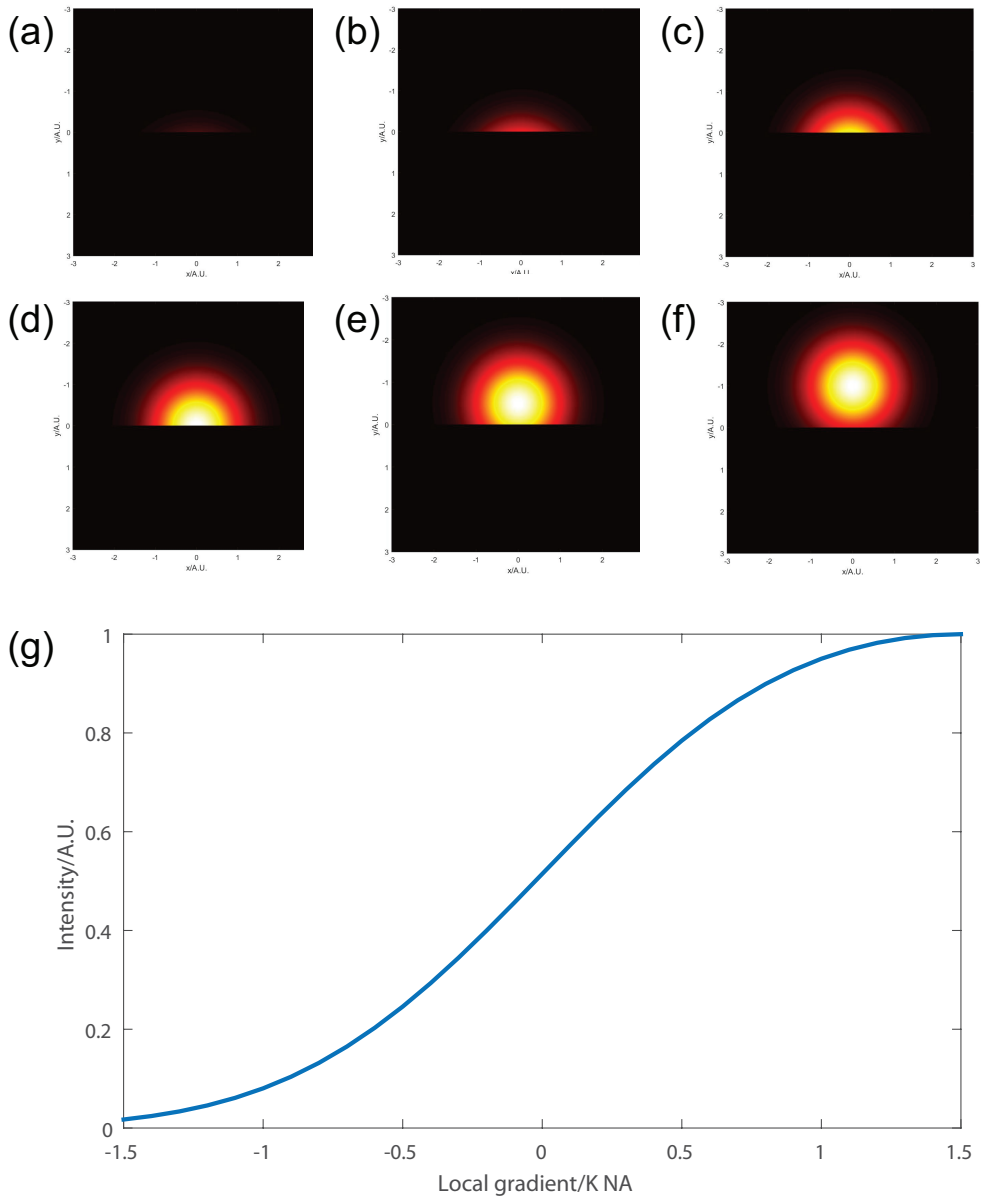

Figure 4.8: Fluorescence intensity changes with the phase gradient. (a)-(f) show the fluorescence patterns on the phase plate when the phase gradient is equal to $-2\pi/3, -\pi/3, 0, \pi/3, 2\pi/3$. (g) shows the intensity changes with the phase gradient.

CHAPTER 5
SECTIONING VOLUMETRIC MICROSCOPY

Self-interference could improve the sectioning capacity in the point-scanning microscopy, but this principle does not work for other 2D or 3D imaging modalities. In this chapter we show using light sheet illumination to reduce the fluorescence background in light field microscopy, and an introduction to light sheet illumination with 2D detection is given in Appendix A. We found with the help of a light sheet, the background of a light field image could be reduced at the cost of the axial field of view. Further, an ultra-fast light sheet system could be setup if the light sheet thickness is smaller than the axial resolution of the light field microscope. Its imaging speed is only limited by the frame rate of the detector. We introduce the setup of this system, and a proof-of-concept experiment is presented at the end of this chapter.

5.1 Introduction and previous work

5.1.1 Light field microscopy

Light field microscopy is developed to record the 3D spatial information in a single image stack so that the 3D image could be acquired at very high rates. In 2006, Ren et al. inserted a microlens array (MLA) into the intermediate plane of a conventional microscope to develop a volumetric microscope [145]. In 2013, wave optics theory is developed to enhance the spatial resolution of light sheet microscopy [41], and later in 2014 Prevedel et al. applied the light field microscope to capture the dynamics of spiking neurons in a volume of $\sim 700\,\mu\mathrm{m} \times 700\,\mu\mathrm{m} \times 200\,\mu\mathrm{m}$ [146].

In Figure 5.1 we illustrate the basic idea behind light field microscopy, which is similar to light field photograph. A Microlens array is located on the intermediate plane of a

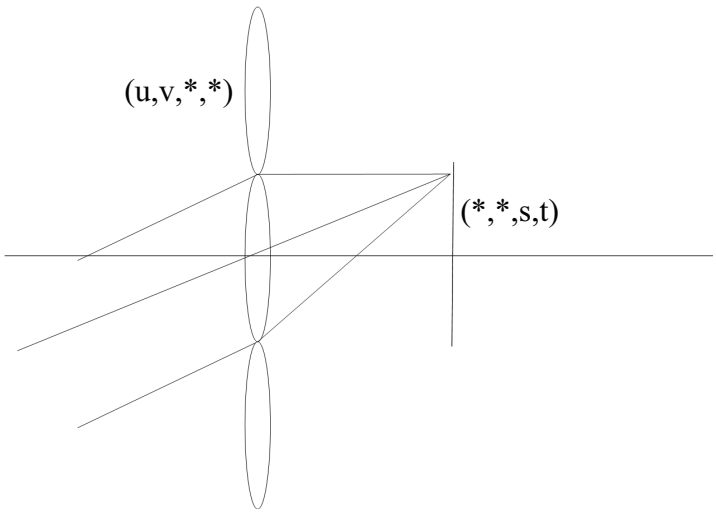

Figure 5.1: Using a MLA to determine the position and the direction of an optical ray. The index of the MLA gives its coordinate, and the index of CCD pixel indicates its direction.

microscope system, and the detector is on the focal plane of the MLA. An optional relay lens could be inserted between them to match the focal lengths. For each pixel on the detector, it has four indexes (u,v,s,t). The detected image is divided into sub-images behind each microlens. $(u, v, *, *)$ is the index of the microlens array and $(**, s, t)$ indicates a pixel with indexes (s, t) in the sub-image. If one photon is detected with index (u, v, s, t), it corresponds to an optical ray passes (s, t), and the angle between this ray and the optical axis is $\alpha = sp/f$, $\beta = tp/f$, where p is the pitch size of the MLA. If all the rays can be traced in the volume, 3D reconstruction is accomplished.

An equivalent camera array based light field microscopy configuration is described in Xin et al. [147]. Instead of a MLA, they used a camera array to gather light from different directions. Each camera has an image of the sample from one perspective, and the final 3D image is reconstructed from the images from all perspectives. This configuration has the advantage of a larger field of view. On the basis of Camera array based light field microscopy, they also developed Snapshot Hyperspectral Volumetric Microscopy for "5D imaging" [148].

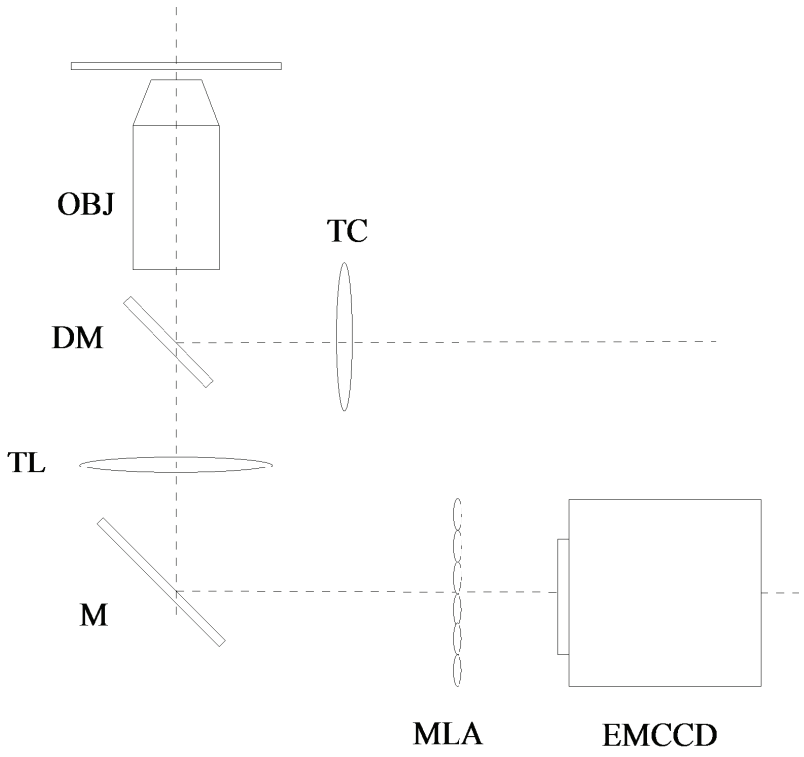

Figure 5.2: Setup of a light field microscope. OBJ: objective, DM: dichroic mirror, TL: tube lens, M: mirror, TC: TIRF collimation lens.

5.1.2 Reconstruction algorithms

Refocusing algorithm

In our work, we used the LFDisplay software [149] from Stanford Computer Graphics Laboratory, which uses a linear transformation to trace the optical rays to their original positions on every specific plane [150].

$$E_{(\alpha \cdot F)}(x', y') = \frac{1}{\alpha^2 F^2} \iint L_F(u(1 - \frac{1}{\alpha}) + \frac{x'}{\alpha}, v(1 - \frac{1}{\alpha}) + \frac{y'}{\alpha}, u, v)\mathrm{d}u\mathrm{d}v \tag{5.1}$$

For more details about this equation, see Ren's work [151]. Compared to nonlinear reconstruction algorithms based on statistics, this is a linear algorithm resistant to system noise.

Statistical algorithm

In 2013, Broxton et al. used wave optics theory and 3D deconvolution for the light field image reconstruction [41]. They modeled the imaging process as:

$$f = Hg \tag{5.2}$$

where f is the light field, g is the discrete volume, and H is the measurement matrix modeling the forward imaging process. Each element in H represents the coefficient to mapping a voxel to a pixel on the light field image. To derive the expression of H , this equation is written into integration:

$$f(x) = \int |h(x,p)|^2 g(p) \mathrm{d}p \tag{5.3}$$

where $h(x,p)$ is the point spread function given by diffraction theory. Next thing to consider is the sensor's noise model, in which the relationship between the intensity detected by the CCD and the original light field image intensity is assumed to be Poisson distributed:

$$f \sim \mathrm{Poison}(Hg + b) \tag{5.4}$$

As a result, the joint possibility of the image is

$$Pr(f|g,b) = \prod_i \left(\frac{(Hg + b_i)^{f_i} \exp(-(Hg+b)_i)}{f_i!}\right) \tag{5.5}$$

This is a convex problem with following gradient descent update

$$g^{(k+1)} = \mathrm{diag}(H^T 1)^{-1} \mathrm{diag}(H^T \mathrm{diag}(Hg^{(k)} + b)^{-1} f) g^{(k)} \tag{5.6}$$

Next we can consider the optics. First, image on the object space is diffracted by the

objective

$$U_i(x,p) = \frac{M}{f_{obj}^2 \lambda^2} \exp(-\frac{\mathrm{i}u}{4\sin^2(\alpha/2)}) \int_0^{\alpha} P(\theta) \exp(-\frac{\mathrm{i}u \sin^2(\theta/2)}{2\sin^2(\alpha/2)}) J_0(\frac{\sin\theta}{\sin\alpha} v) \sin\theta \mathrm{d}\theta \tag{5.7}$$

where the coordinates u and v are given below

$$\begin{cases} u = k\sqrt{(x_1 - p_1)^2 + (x_2 - p_2)^2} \sin\alpha \\ v = 4kp_3 \sin^2(\alpha/2) \end{cases} \tag{5.8}$$

The diffraction process on MLA plane can be obtained using Fresnel diffraction in the Fourier domain:

$$h(x,p) = F^{-1}\{F\{\Phi(x) U_i(x,p)\} \exp[-\frac{\mathrm{i}}{4\pi} f_{\mu lens}(\omega_x^2 + \omega_y^2)]\} \tag{5.9}$$

Here $\Phi(x) = \phi(x) * \mathrm{comb}(x/d)$, where the comb function represents the repeating factor and $\phi(x) = \mathrm{rect}(x/d) \exp(\frac{-\mathrm{i}k}{2f_{\mu lens}} ||x||_2^2)$. To apply those results in deconvolution, we finally rewrite it as a discrete version

$$h_{ij} = \int_{\alpha_j} \int_{\beta_i} \omega_i(p) |h(x,p)|^2 \mathrm{d}p \mathrm{d}x \tag{5.10}$$

where α_j is the area for Pixel j, β_i is the volume for Voxel i. Then Voxel i is integrated over a cubic volume centered at point P. This method uses the aliasing of the lenslets to deduce the high-resolution information. Broxton has shown this by comparing with the deconvolution method with the previous computational focal stacks, but it is also shown that lots of artifacts are induced in the reconstruction process, which may cause problems in quantitative analyses.

5.1.3 Limitations

The first limitation of light field microscopy is the illness nature of the reconstruction algorithm. According to the Fourier Slice Theorem, Fourier transformation of an angular projection is a slice in the Fourier domain, as plotted in Figure 5.3. In light field microscopy only projections satisfying $n \sin\theta < NA$ could be acquired, resulting in a missing cone in the frequency domain (shown in circles in Figure 5.3). That means the reconstruction may not be unique: any distribution in the missing cone will not change the measurement result as long as a non-negative condition is satisfied in the spatial domain. Limit angle reconstruction algorithms, or deconvolution could be applied for reconstruction [145]; but some artificial constraints have to be imposed, like the sample need to be smooth. As the case in deconvolution microscopy, the background cannot be fully removed if the sample has a high density.

The second is a limited spatial resolution. Ren et al. have derived $N_u N_v = \frac{W*H}{R_{obj}^2}$, where $R_{obj} = \frac{0.47\lambda}{NA}M$. W and H are the microlens dimensions, N_u and N_v are resolvable sample points behind a lenslet, and R_{obj} is the Sparrow resolution [145]. That means spatial resolution has been obtained at the cost of its lateral resolution.

5.2 Microlens array coupled light sheet

5.2.1 Principle

Background reduction in light field microscopy

The principle of our background reduction is shown in Figure 5.4. The fluorescence from the detected point is drawn in red, and the background fluorescence is drawn in green. In epi-fluorescence light field the whole sample is illuminated. Each pixel in the detector would gather fluorescence from the entire sample, which is much stronger than the fluorescence from the detected point. However, if we use a light sheet to illuminate some stacks selectively, the background level could be reduced. We show the experiment results

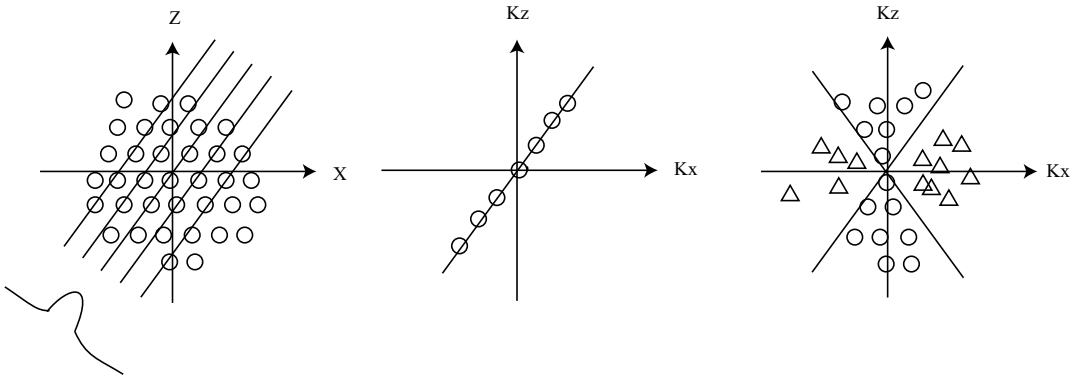

Figure 5.3: Illustration of Fourier Slice Theory. Left: detected signals are the linear integrations of spatial signals. Middle: Fourier transformation of the linear integration gives a slice of the spatial frequency component in a specific direction. Right: limited detection angle means only signals with spatial frequency in some specific angles (plotted in circles) could be detected, while the triangle components are missing.

in Figure 5.13.

The axial field of view in the light field h is determined by the lateral field of view w: $h = w/NA$. In our system the lateral field of view is $w = 515 * 16/20 = 400\,\mu\mathrm{m}$ and $NA = 0.25$. This yields $h = 1600\,\mu\mathrm{m}$, which indicates 1.6 mm thick specimen will contribute to the background of the image. If we illuminate part of this layer, for example, $100\,\mu\mathrm{m}$, the background of the detected image could be $1/16$ of the original image and a 4-fold improvement in SNR could be achieved.

5.2.2 Motionless MLA coupled light sheet

When the thickness of the light sheet is even thinner than the axial resolution of the light field reconstruction, the MLA could be used to refocus the light at a specific axial position. It would be a light-scanning light sheet microscopy, in which the axial scan is performed by the movement of the light sheet instead of the sample movement. Oscillation of galvanometer on the focal plane results in parallel movement of optical rays, as shown in Figure 5.8. Since oscillation of a galvanometer is usually much faster than the movement of piezo stages, this configuration could significantly speed up the 3D imaging process in light sheet microscopy.

The effect of MLA in this light sheet system is shown in Figure 5.5. In Appendix C we derived that the reconstruction uncertainty increases with its axial coordinates and decreases with the lenslet size for off-focus positions, as shown in Figure 5.5.

5.2.3 System setup

Laser output unit

Laser (PicoQuant, PDL 800D) is attenuated by a neutral density filter and then reflected by a mirror. A pair of collimation lenses (L1 and L2) are used to expand the diameter of the laser to 6 mm. Then an iris is used to change the diameter of the laser beam, in order to control the field of view in the epi-fluorescence mode or control the light sheet thickness in

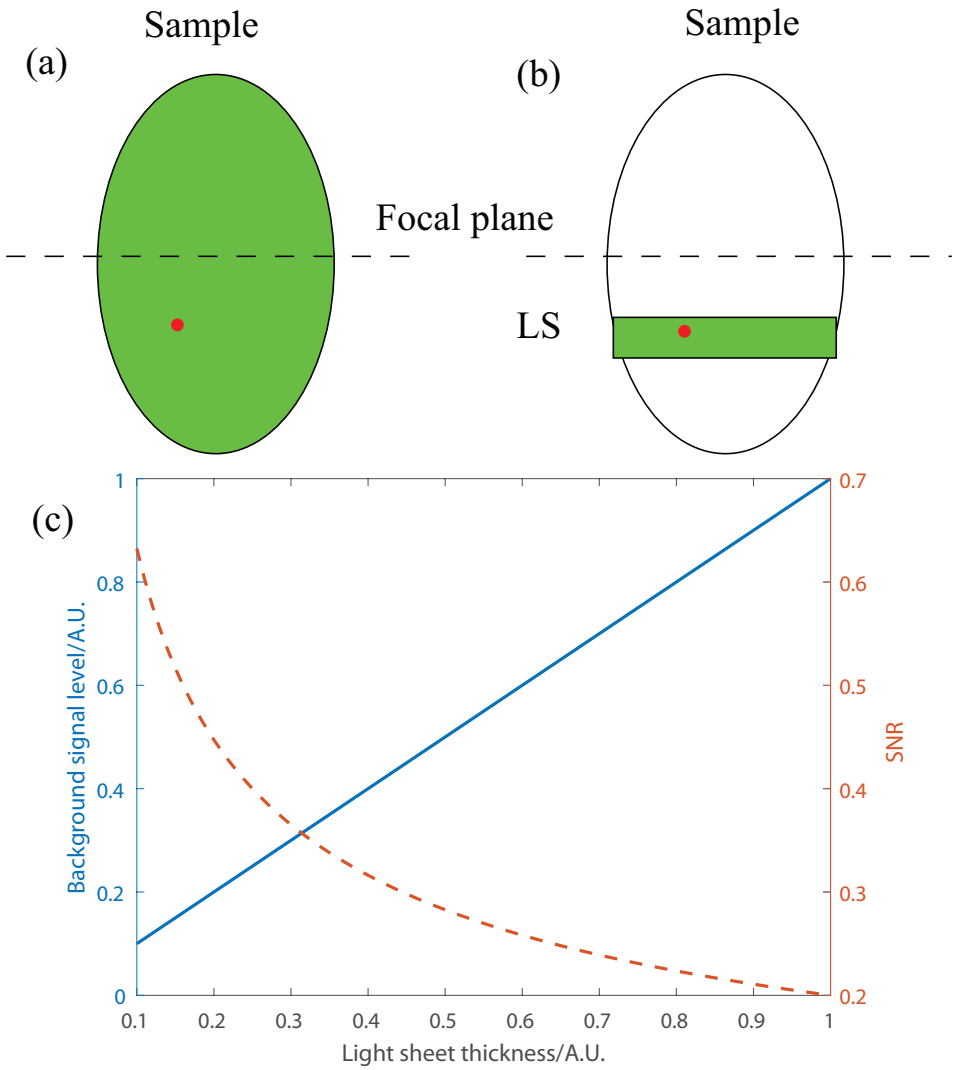

Figure 5.4: Principle of the light field background reduction. Green: fluorescence background; Red: signal from the detected point. (a) In an epi-fluorescence light field, the entire sample is illuminated. Each pixel in the detector would gather fluorescence from the entire sample, which is much stronger than the fluorescence from the detected point. So the original image is hard to restore. (See the right column of Figure 5.14). Using a light sheet, we can selectively excite stacks to reduce the background level. (see Figure 5.13(a)-(c)) (c) Background level(blue solid) reduces with the reduction in the light sheet thickness, while the SNR (red dashed) reduces with the inverse square root of the background level.

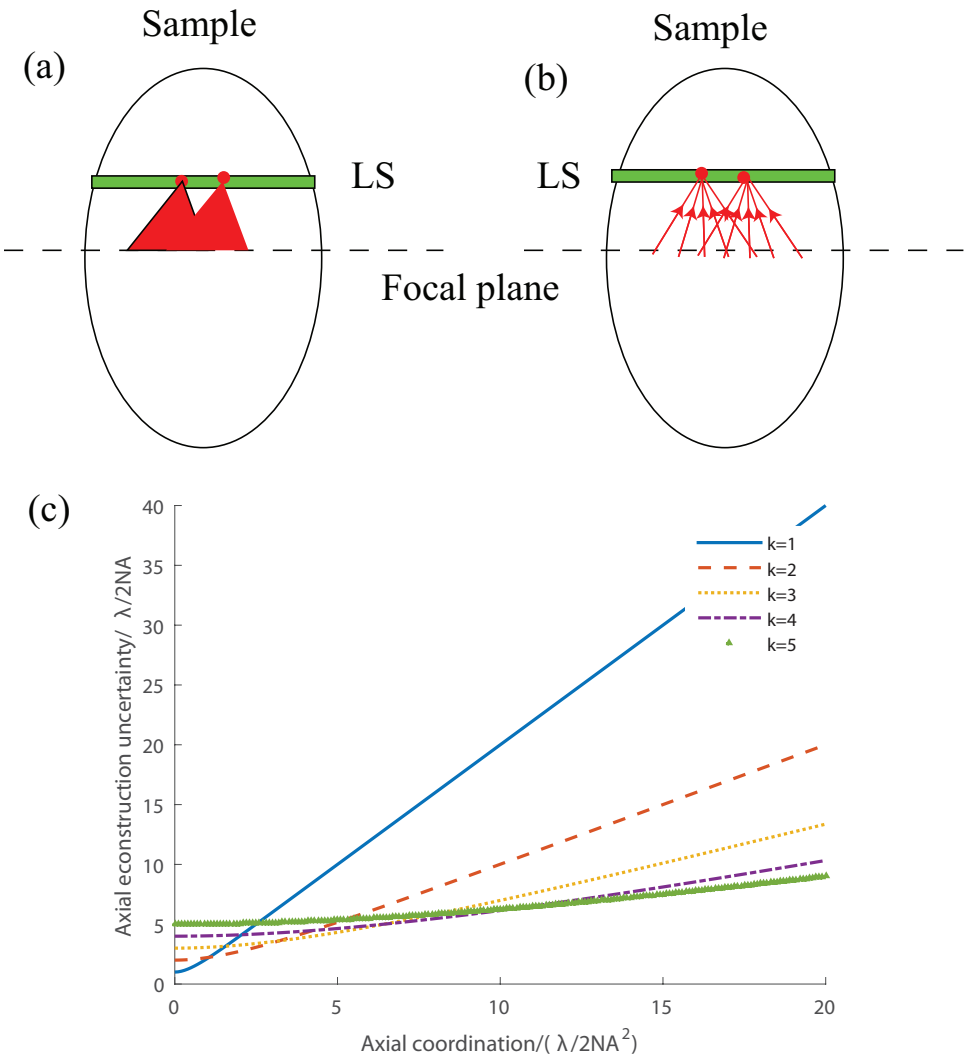

Figure 5.5: Principle of the MLA coupled light sheet microscopy. (a) When using a thin light sheet, defocused images will blur. (Figure 5.13(d)) (b) Using microlens array, we can trace the optical rays back to their original positions. (Figure 5.13(c) and left column of Figure 5.14) (c) The reconstruction uncertainty increases with its axial coordinates. k is the pitch size of microlens array with respect to the FWHM of the diffraction PSF: $P = kM\lambda/2NA$. The larger lenslet is used in MLA, the less off-focus divergence there could be. For our system the unit of x-axis is about $1.3\,\mu\mathrm{m}$, unit of y-axis is $2.6\,\mu\mathrm{m}$ and $k = 5$.

the light sheet mode.

Epi-illumination unit

A TIRF collimation lens is used to focus the laser on the back focal plane of the objective. The dichroic mirror is used to reflect the laser and separate the excitation light path and the fluorescence detection light path. Then the laser would be nearly parallel after it exits the objective, illuminating evenly on the sample. The sample is placed on a 3D stage, with manual adjustments on the XY plane and a piezo stage on the z-axis. Control of the piezo stage is discussed in detail in Appendix C.

Detection unit

Fluorescence from each excited fluorophore is collected by the objective (10X/0.25), passes the dichroic mirror (Chroma) and then it is collimated by the tube lens (Edmund Optics, f=400 mm). Before the intermediate plane, two mirrors are inserted to adjust the position of the image. The microlens array (Thorlabs MLA150-5C, f=$5200\,\mu\mathrm{m}$, pitch size $150\,\mu\mathrm{m}$) is placed on the intermediate plane, and a 1:1 relay lens (Nikon 105 mm macro) is used to match the intermediate plane and the EMCCD plane (Andor, DU897U). The protocol we used to align the MLA on the intermediate plane is discussed in Appendix C.

Light sheet illumination unit

When we want to use the light sheet illumination, we remove mirror M4, and the laser goes into the 2D galvanometer. The scanning mirror of the galvanometer is on the focal plane of L2. L1 and L2 consist a 4f system, and their distance is about 300 mm. Cylindrical lens and L1 are close together, and their distance to the back focal plane of OBJ2 is the their focal length, about 150 mm.

To make sure the conjugation of the galvanometer and the objective focal plane, we used a trick: 1. Narrow down the diameter of the incident laser beam; 2. Drive the galvanometer

to oscillate at a slow rate distinguishable by naked eyes; 3. Put a screen at some distance away from the objective lens, and we can observe the movement of the laser disk. When the galvanometer is conjugate to the focal plane, the output laser point moves in parallel and its shift could hardly be observed; otherwise, the movement would be very obvious.

Then we can align the position of the light sheet to the detection light path. First, under epi-fluorescence, we search the sample for a structure that is small and bright enough. We move this marker to the center of our field of view. Then we are going to move the position of the light sheet. We adjust the screws on the mirror to make sure the laser incident normally to the optical axis of OBJ1 and repeatedly adjust the other two degrees of freedom until the intensity of this marker reaches its maximum.

An excitation filter is suggested by Chroma, and it is proved to be necessary for low SNR conditions. Diode laser usually has multiple laser emission lines. Other weak lines may contribute a lot of reflection signal in fluorescence images.

5.2.4 Software design

Measurement control system

The measurement control software is written in Labview from National Instruments. The User Graphical Interface is shown in Figure 5.9. Two subunits would be used in our measurement: galvanometer scanning and 3D imaging.

5.2.5 Results

Evaluation of system parameters

To measure the thickness of the light sheet, we removed the cylindrical lens CL and measured the PSF of the objective lens OBJ2. First, we filled a cuvette with Cy5 solution. The fluorophore is diluted 1:1000 to avoid scattering, but the concentration should be high enough to generate a signal above the noise level. As shown in Figure 5.10, when the radius

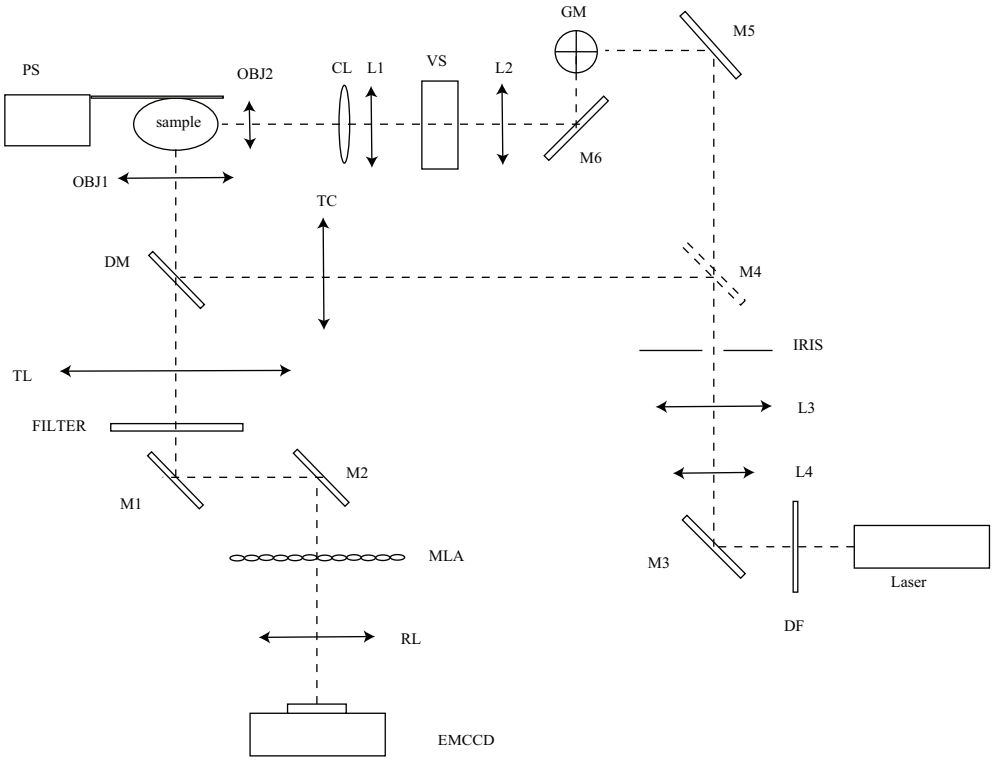

Figure 5.6: Schematic diagram of our system. PS: piezo stage, OBJ1, OBJ2: objectives (10X/0.25), L1, L2, L3: lenses ($f = 150\,\mathrm{mm}$), L4 is a doublet lens ($f = 25\,\mathrm{mm}$), CL: cylindrical lens ($f = 150\,\mathrm{mm}$), $M1 - M5$ are mirrors. DM: dichroic mirror, DF: density filter, MLA: microlens array, VS: vertical shift stage, a stage with two mirrors to shift the height of the optical path.

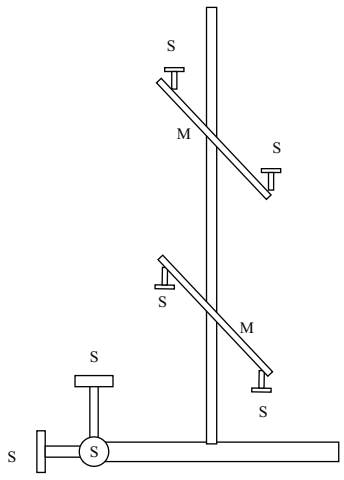

Figure 5.7: An illustration of the vertical shift stage. M: mirrors, S: screws to adjust x,y,z positions of the stage and orientations of the mirror surfaces.

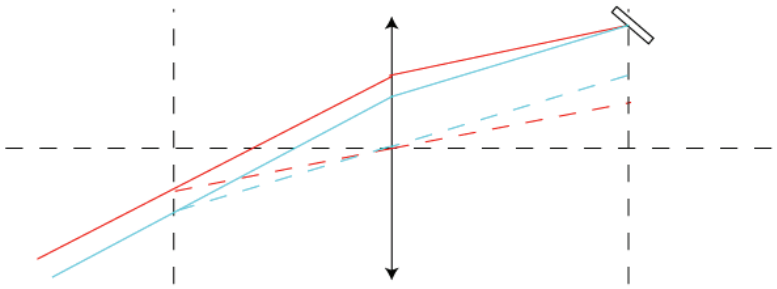

Figure 5.8: When the galvanometer is conjugated to the back focal plane of the objective, output optical rays could scan in parallel.

of the iris is changed from its maximum to minimum, the light sheet thickness alters from $6\,\mu\mathrm{m}$ to $16\,\mu\mathrm{m}$ correspondingly, and the illumination becomes more uniform. When the thickness is about $10\,\mu\mathrm{m}$, its Rayleigh length is larger than the field of view. We used this condition in the following experiments.

We presented the reconstruction of a thin cotton layer in Figure 5.12, at (a) z=$-23\,\mu\mathrm{m}$, (b) z=$23\,\mu\mathrm{m}$, and (c) z=$102\,\mu\mathrm{m}$. The focal region is shown in the yellow circle. In the red rectangle, we see the structures are contaminated by the strong background. This background could be extremely strong in thick samples as shown in Figure 5.14. So this system needs to be improved by selectively illuminating some specific layers.

Background reduction in light field microscopy

The sample we used here and below is cotton fiber with Cy5 fluorophore solution. The fluorophores adherent to the cotton fibers are unevenly distributed after they dry. The diameter of the cotton fiber is several micrometers, similar to the size of cells in embryos.

We showed the reduction of the light field background with a light sheet illumination in Figure 5.13. In (a) and (b) we used laser scanning to illuminate the region between $z = -100\,\mu\mathrm{m}$ to $z = 0\,\mu\mathrm{m}$. The original epi-fluorescence reconstruction is shown in Figure (d), where no features could be recognized due to the strong background. With

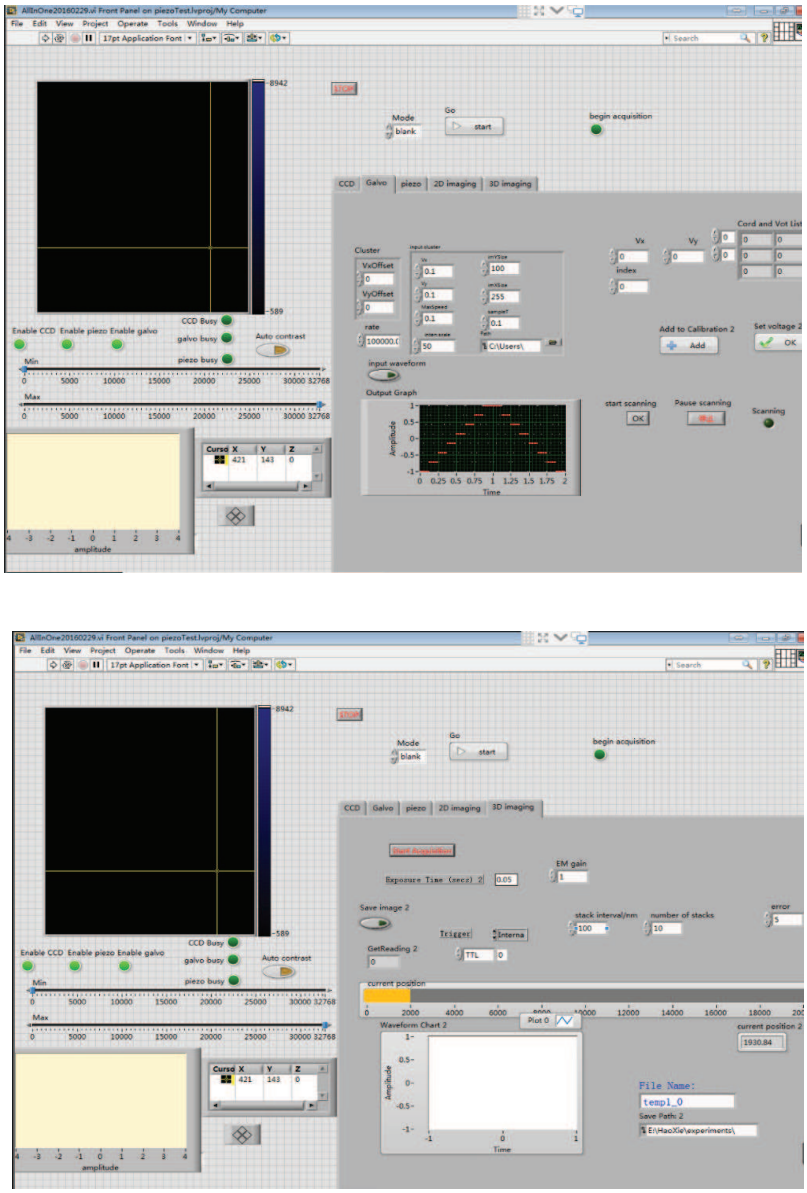

Figure 5.9: User Graphic Interface of our control software. Up: galvanometer scan. Below: 3D scan.

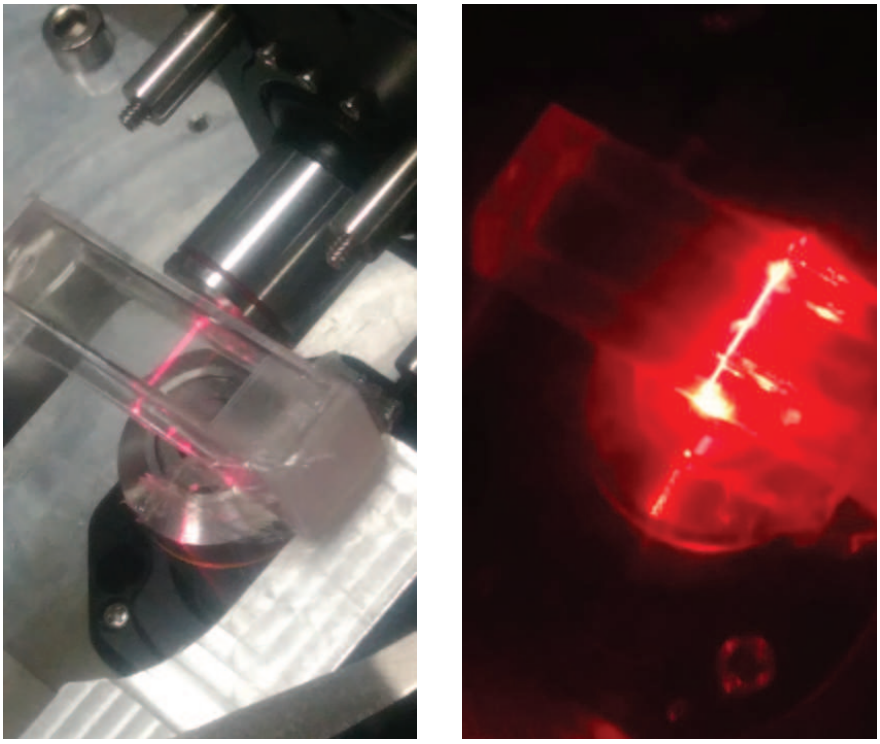

Figure 5.10: Setup used to measure the thickness of the light sheet. Left: positions of the specimen, the excitation objective and the detection objective. Right: photo of the excitation light beam.

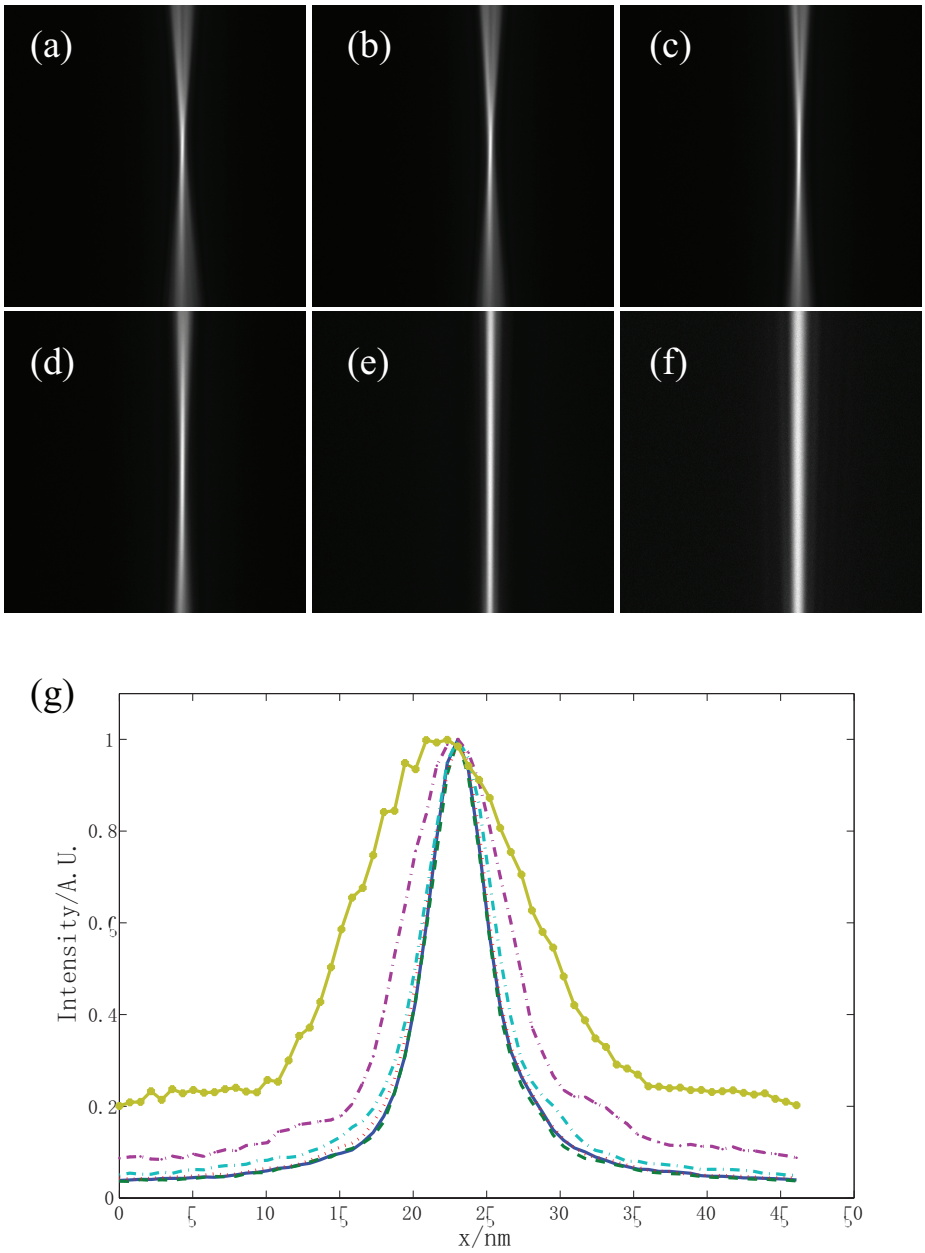

Figure 5.11: With different incident laser diameters, the thickness of the light sheet changes from 6 µm to 16 µm.

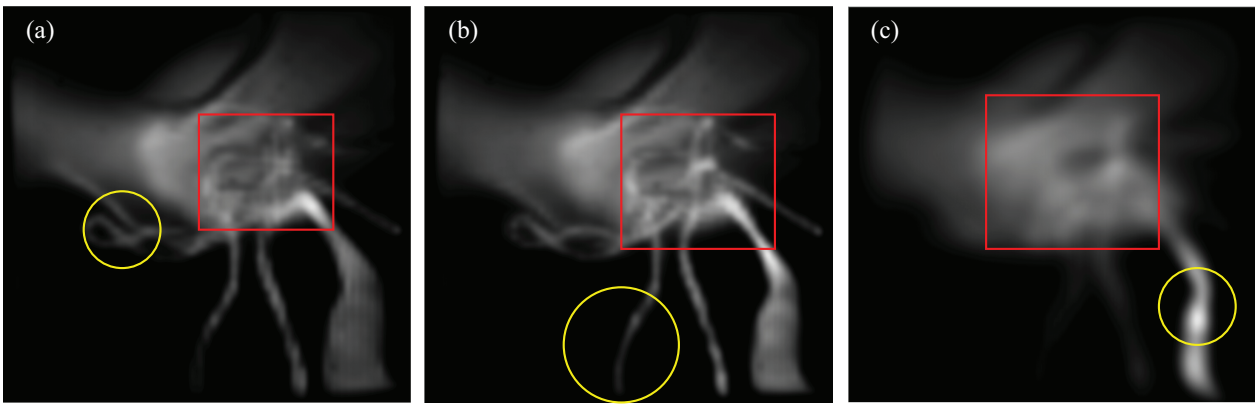

Figure 5.12: Reconstruction of a thin cotton layer. (a) z=$-23\,\mu\mathrm{m}$, (b) z=$23\,\mu\mathrm{m}$, and (c) z=$102\,\mu\mathrm{m}$. The focal region is shown in the yellow circle. In the red rectangle we see the structures are obscured by background.

our background reduction, we can reconstruct the structures at z=$-90\,\mu\mathrm{m}$ and z=$-36\,\mu\mathrm{m}$ as shown in the red circle. Similarly, in (c) we illuminate $z = 200 \sim 300\,\mu\mathrm{m}$ and could reconstruct the structures at $z = -233\,\mu\mathrm{m}$.

Motionless light field microscopy

Right columns in Figure 5.14 are images reconstructed from conventional light field microscopy. Some details could be recognized from the images, but the background is so strong. In the left column we reconstruct different raw images at the same z-stacks as the right column, but with a $10\,\mu\mathrm{m}$ light sheet illumination. We found the signal is significantly stronger compared to the background. More details are revealed compared to the conventional method. Images were taken without moving the sample or the objective; by taking images at different light sheet position, original 3D fluorophore distribution could be reconstructed.

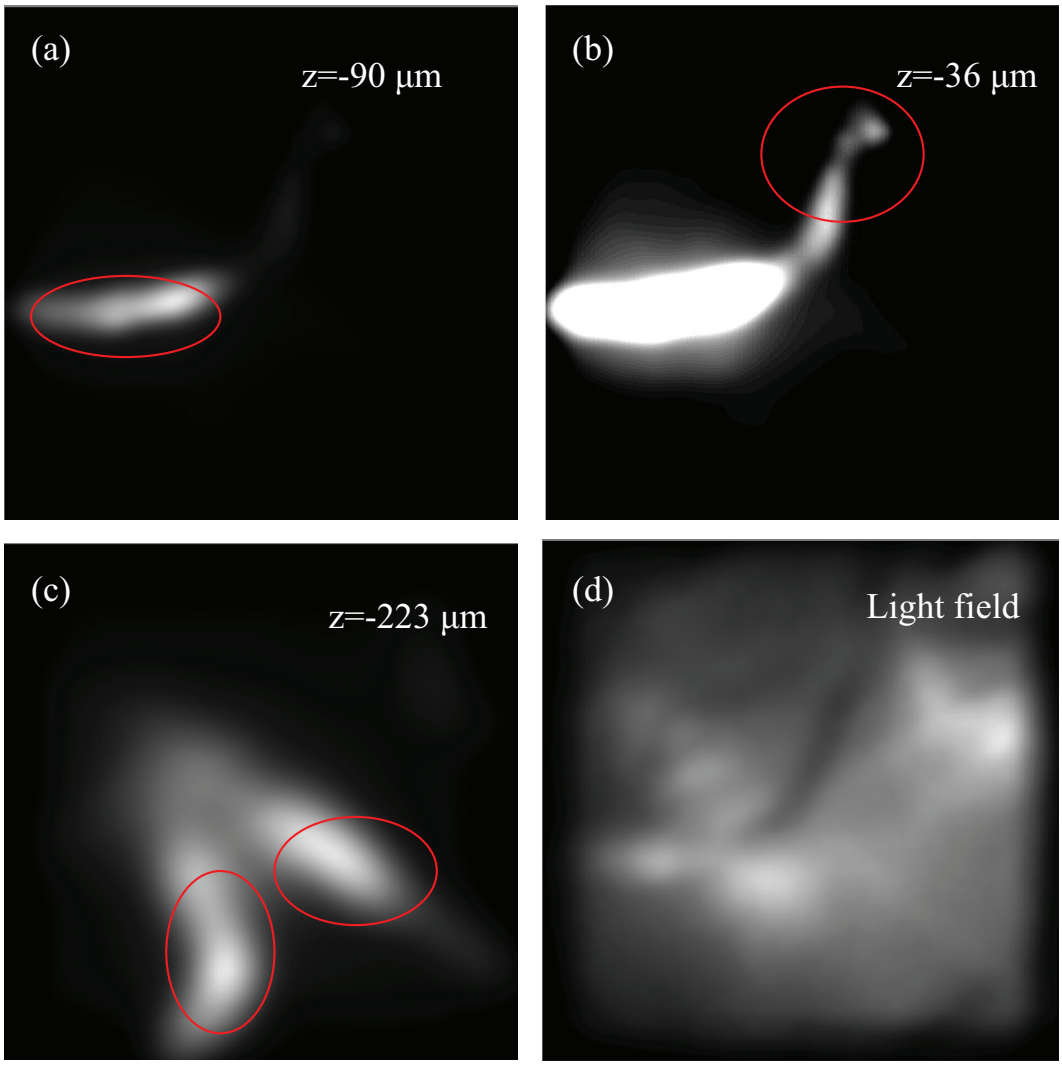

Figure 5.13: Reduce the background with a light sheet in light field microscopy. In (a) and (b) we used laser scanning to illuminate the region between $z = -100\,\mu\text{m}$ to $z = 0\,\mu\text{m}m$. With our background reduction, we are able to reconstruct the structure at $z = -90\,\mu\text{m}$ and $z = -36\,\mu\text{m}$ as shown in red circle. Similarly in (c) we illuminate $z = 200 \sim 300\,\mu\text{m}$ and could reconstruct the structure at $z = -233\,\mu\text{m}$. In (d) we show reconstruction of $-100 \sim 200\,\mu\text{m}$ in conventional epi-fluorescence light field, in which the background is too high that details can hardly be distinguished.

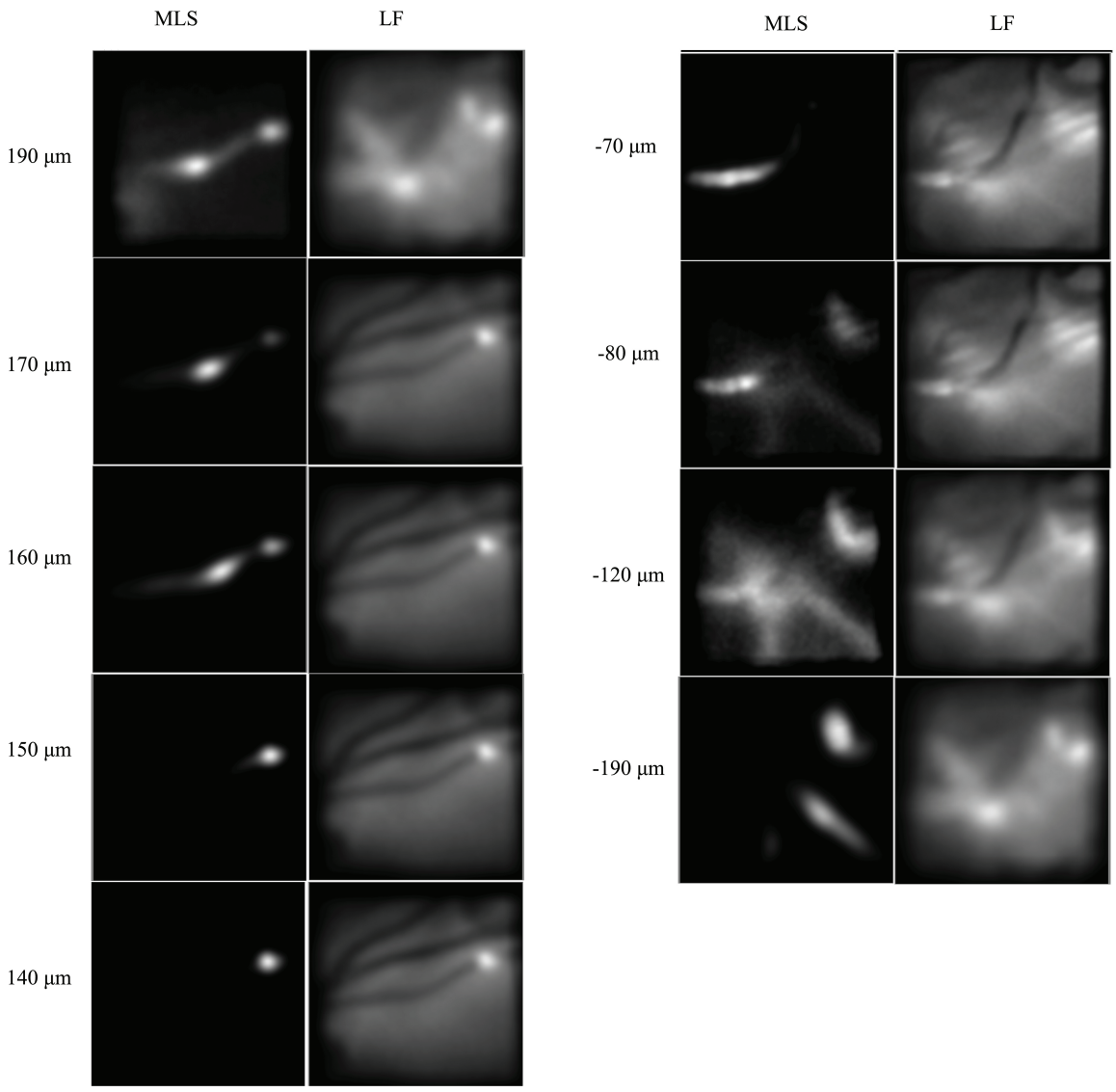

Figure 5.14: MLA coupled light sheet and light field images of cotton fibers. Left: MLA coupled light sheet. Right: light field reconstruction.

5.3 Conclusions and discussions

In this chapter, we reduced the background and improved the SNR of light field system by implementing light sheet excitation. We also found that an ultra-fast, motionless light sheet system could be established by reducing the light sheet thickness below the axial resolution of light field microscopy. Evaluation of cotton samples has verified that our system has superior performance than conventional light field microscopy in thick heavy-labeled specimens.

In conventional fluorescence microscopy, expansion of the axial field of view could also be achieved by reducing the numerical aperture, but fluorescence efficiency is sacrificed since the objective's power of collecting photons is proportional to the square of the numerical aperture. Our method does not scarify the photon efficiency, so every photon is used to enhance the image quality. There are also so-called remote focusing techniques, which use vari-focus lenses, microelectromechanical mirrors or acoustooptics modulators to change the focal length of the optical elements [152]. However, they have to overcome two problems: 1. aberration of systems; 2. synchronization of light sheet scanning and focal plane change. Our method has provided another alternative if the resolution could be enhanced by structured illumination.

Our system has two major problems before it could have more applications: First, the lateral resolution is sacrificed. This could be slightly compensated with deconvolution, but a more elegant solution is the combination of structured illumination. Second, speed is sacrificed for SNR. Adaptive illumination could be developed on the base of our system to balance these two factors.

CHAPTER 6

CONCLUSIONS AND DISCUSSIONS

6.1 Comparison of sectioning microscopy

We assume the quantum efficiencies of PMT, each pixel in EMCCD and sCOMS are similar for simplicity. To acquire an epi-fluorescence image with enough SNR, excitation intensity I and imaging time t seconds is required. There are $N * N$ pixels in an image, and z stacks are taken for the sample. The total imaging time is zt, with peak intensity on the image I and total energy zIt. Z-scan could be realized by piezo scanning.

TIRF is similar to epi-fluorescence, except large scale z scanning is not feasible. The total imaging time is zt, with peak intensity on the image I and total energy zI, assuming we still take z stacks. TIRF has a good sectioning capacity on the boundary.

In confocal, dwell time for each pixel is t/N^2 with its excitation intensity N^2I. The total intensity is zIt. Since t used here is usually longer than epi-fluorescence and the peak intensity is much higher, fluorophores are more prone to photobleaching.

STED is a special confocal, except its enhanced resolution requires higher sampling rate. Assuming the resolution enhancing factor is a, the total imaging time is za^2t, with peak intensity on the image Ia^2 and total energy zIa^2t. MEANS is similar to STED, but

Table 6.1: Comparison of sectioning microscopy

	Sectioning	Z-scan	Bleaching	Resolution	Speed
epi-fluorescence	*	***	**	**	**
TIRF	***	*	**	**	**
Confocal	**	***	***	***	*
STED	**	***	****	****	*
MEANS	***	**	****	****	*
Light sheet	***	***	*	**	**
Light field	*	**	*	*	***
MLA-coupled LS	***	***	*	*	***

the Z-scan is restricted in a smaller range.

For light sheet, the total imaging time is zt, with peak intensity on the image I and total energy I. It could effectively reduce photobleaching.

Light field reducing the acquisition time by simultaneous imaging all stacks. The total imaging time is t, with peak intensity on the image I and total energy I. The cost is a reduction in its resolution. It is suitable for samples that need high temporal resolution but low spatial resolution.

The parameters for MLA coupled light field vary according to light sheet conditions. If the light sheet thickness is thicker than the resolution of light field microscopy, it is a background-reducing light field microscopy. If the thickness of the light sheet is smaller than the light field, the MLA is used to extend the field of view in the z-axis. It could be applied to fluorescent samples with high labeling density.

6.2 Conclusion

Optical microscopy is one of the most widely used tools in biomedical researches. However, in the observation of thick biological samples, conventional optical microscopes suffer from the background of out-of-focus structures. For example, in conventional epi-fluorescence microscopy, the entire sample is illuminated, and the out-of-focus light contributes a strong background to the image, thus obscuring the in-focus details. Confocal microscopy and light sheet microscopy are popular techniques for sectioning imaging. In this dissertation, excitation patterns are designed to improve optical sectioning capacity for point-scanning and volumetric imaging systems.

In the first part of the dissertation, we improve the point-scanning microscopy with excitation laser modulations. We used a mirror to reflect the incident laser to produce an interference in the focal volume. It is found both the sectioning capacity and the peak intensity of the excitation beam and the depletion beam in STED are improved and the signal to noise ratio is enhanced. First, we used diffraction theory to simulate the intensity

distribution in the focal volume. Then we proved its improved sectioning capacity with a nano-particle phantom sample. We grew Vero cells on a silicon dioxide layer above the mirror and applied this method to those samples on conventional multi-color, spinning disk and two-photon microscopy. Further, we developed spectrum methods to move the interference layer inside cell, making 3D observation possible. Finally, we demonstrated the increase in intensity could be used to reduce the laser power requirement in STED microscopy.

This dissertation also developed a point-scanning based phase contrast microscopy: Schlieren confocal microscopy. We found the incident laser refracts due to the local gradient of the sample, and the detected fluorescence intensity could quantitatively reflect the local gradient of the sample. We built the model and applied it to biological specimen measurements. We found this method could obtain a similar effect as the Differential Interference Contrast microscopy, keeps the optical sectioning capacity of confocal, and is fully compatible with confocal.

In the third part, this dissertation applied excitation modulations to inhibit the background in light field microscopy. Light field microscopy sacrifices spatial resolution for acquisition speed and is preferable in the observation of the fast biological phenomena. However, light field reconstruction problem is ill-defined, and it would result in a strong background. We combined light sheet illumination with microlens array coupled detection. It is demonstrated this method could significantly reduce the background in conventional light field microscopy and has faster speed compared to light sheet. It could be applied in samples with high label densities.

In conclusion, we succeed to apply spatially modulated excitation to point-scanning and volumetric imaging systems and improved their sectioning capacities. Our research could be promising tools for in-vivo observation in large specimens.

Appendices

APPENDIX A

SET UP OF A SELECTIVE PLANE ILLUMINATION MICROSCOPE

In this chapter, we introduce the design of a light sheet microscopy plugin on a Zeiss epi-fluorescence microscope. It helps to understand how light sheet removes the fluorescence background.

A.1 Methods and materials

A.1.1 System setup

The schematic diagram is plotted in Figure A.1. Mechanical design is illustrated in Figure A.1(a). Our system is built on Zeiss Observer Z1. The bottom of the system is located between the microscope turret and a piezo stage (PI Z510), which is also used to control the movement of the objective. A mini platform is built above the objective, and a Miniature Dovetail Stages (Thorlabs, DT12XYZ) is used to control the long-distance movement of the light sheet. Then the optical system, constructed from 16 mm and 30 mm cage systems (Thorlabs), is connected to this stage.

The optical design of our system is plotted in Figure A.1(b). A 640 nm Laser (Toptica iBeam smart, 0.9 mm output diameter) is collimated by a 2X telescope pair (Thorlabs 352610-A f=4 mm and 352240-A f=8 mm). Then it is coupled into a single mode fiber (Thorlabs, 630HP, NA=0.13) by a fiber port coupler (Thorlabs, PAF-SMA-11-A, f=11 mm). The other end of the fiber is connected to another fiber port coupler. The output laser diameter is 2.9 mm. After reflected by the mirror, laser transverses an acylindrical lens (Thorlabs AYL108-B, f=8 mm, NA=0.49) and an aspheric lens (Thorlabs 355151-A, f=2 mm, OD=3 mm NA=0.5). Then a light sheet can be formed with a thickness of about $1\,\mu\mathrm{m}$. The light sheet system and objective (Zeiss 40 X air, NA=0.6) could be moved along z with

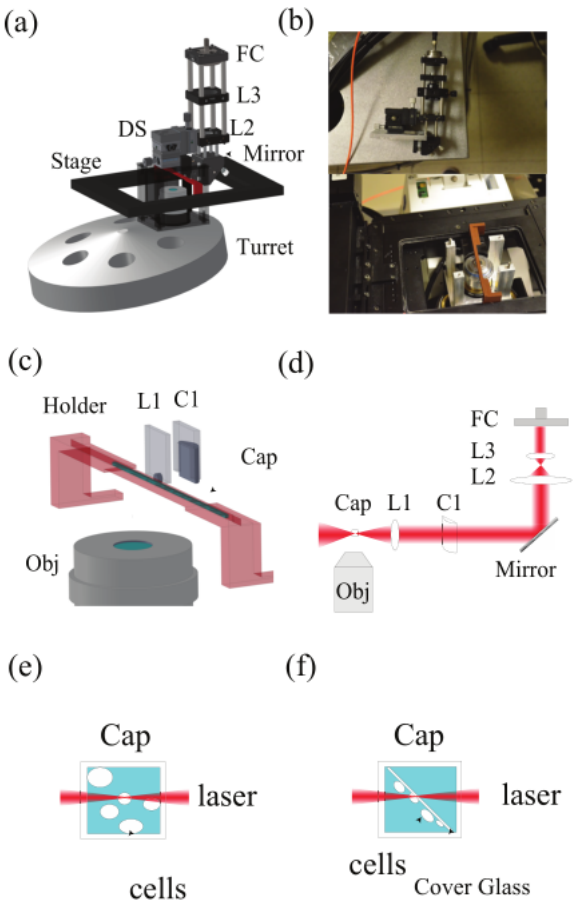

Figure A.1: Schematic diagram of a light sheet system. (a) is the draft of the system and (b) is the optical path. FC: fiber coupler, L1, L2, L3 are aspheric lenses. C1: acylindrical lens, Obj: objective, Cap: capillary. (c) and (d) are photos of two different parts.

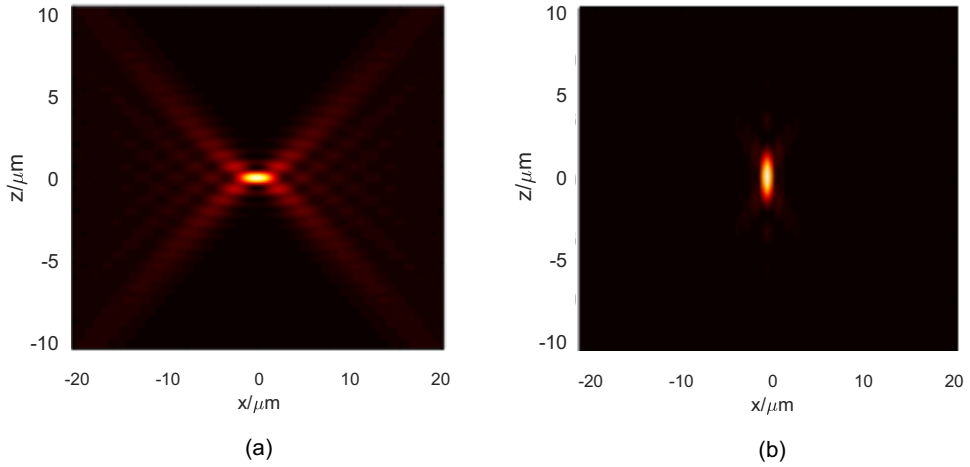

Figure A.2: Point spread function of a light sheet microscope. (a) light sheet PSF. (b) objective PSF.

the turret. All customized lens adapters are made on a mill (Trek) or laser cutter (Universal laser cutter). The sample stored in a 1 mm capillary is supported by a customized holder (Makerbot) on the microscope stage. The image is collected by an sCMOS (HAMAMATSU, ORCA-Flash 4.0 V2).

Motion control of this sample consists of four parts: microscope turret could move the objective and light sheet along the z-axis, which is equivalent to a movement of the sample. A miniature Dovetail stages is used to adjust the light sheet for long distance, while a piezo stage works together with the turret to make fine adjustments for the objective. As a result, the sample, the light sheet, and the objective can move independently. The lateral movement of the sample is realized by the microscope stage. The whole system is designed as compact as possible to minimize the torque and to fit the microscope space. The entire system is controlled by micro-manager [153].

A.1.2 Sample preparations and immunofluorescence staining

We used Tetraspeck beads in low melting agarose as test samples. 100 mg low melting agarose (Lonza) was heated and mixed with 10 ml boiling deionized water. Stirred for about

15 minutes until the solution is clear. Then we cooled it down to the room temperature, mixed $50\,\mu l$ agarose solution with $3\,\mu l$ of $0.1\,\mu m$ Tetraspeck microsphere and vortexed. Finally, we used a pipette to inject this solution into a capillary (Vitrocom 8280, square with outer dimension 1.12 mm). This capillary was kept in $4\,^{\circ}C$ fridge for 20 minutes and rotated every two minutes to prevent precipitation. Finally, both ends were sealed with nail polish to prevent the gel from moving along the capillary.

To make floating cell samples, we cultivated the Vero cells in a T75 flask for two days. We aspirated Dulbecco's Modified Eagle's Medium (DMEM++) medium, washed with Phosphate-buffered saline (PBS) and added 2ml of Trypsin. After 5 minutes in the cell culture room, cells were added with 10 ml of DMEM++ to deactivate the Trypsin. We transferred the cells to a tube, centrifuged (1000g, 5min) and carefully aspirated the liquid. 10 ml of 50:50 methanol-acetone was added to fix and permeabilize the cells. The cells were put in $4\,^{\circ}C$ freezer for 10 minutes, then centrifuged and washed again. We used Mab 414 (Abcam) as the primary antibody, $5\,\mu l$ in 5 ml of PBS, and put cells into $37\,^{\circ}C$ incubator for 30 minutes. Then we used Donkey anti-Mouse IgG (ThermoFisher) as the secondary antibody ($5\,\mu l$ in 5 ml of PBS) and incubated for 30 minutes again. Finally, we washed and mixed the cells with low melting agarose solution following the same procedure as the beads samples.

For microtubule samples, we used the same Vero cells as NPC samples but grew them on coverslips (1 mm*10 mm) in a glass bottom dish (MatTek). We fixed cells in $300\,\mu l$ 4% paraformaldehyde (PFA) buffer for 10 min at room temperature, then permeabilized cells using 1% Triton X 100. Then E7 (DSHB) was used as the primary antibody, and Donkey anti-Mouse IgG (ThermoFisher) was used as the secondary antibody. Finally, we stained the cells with DAPI and inserted the coverslips into a capillary. Capillaries were filled with SlowFade Antifade Reagents (ThermoFisher) as mounting medium to reduce the diffractive index mismatch on glass surfaces, and sealed with nail polish.

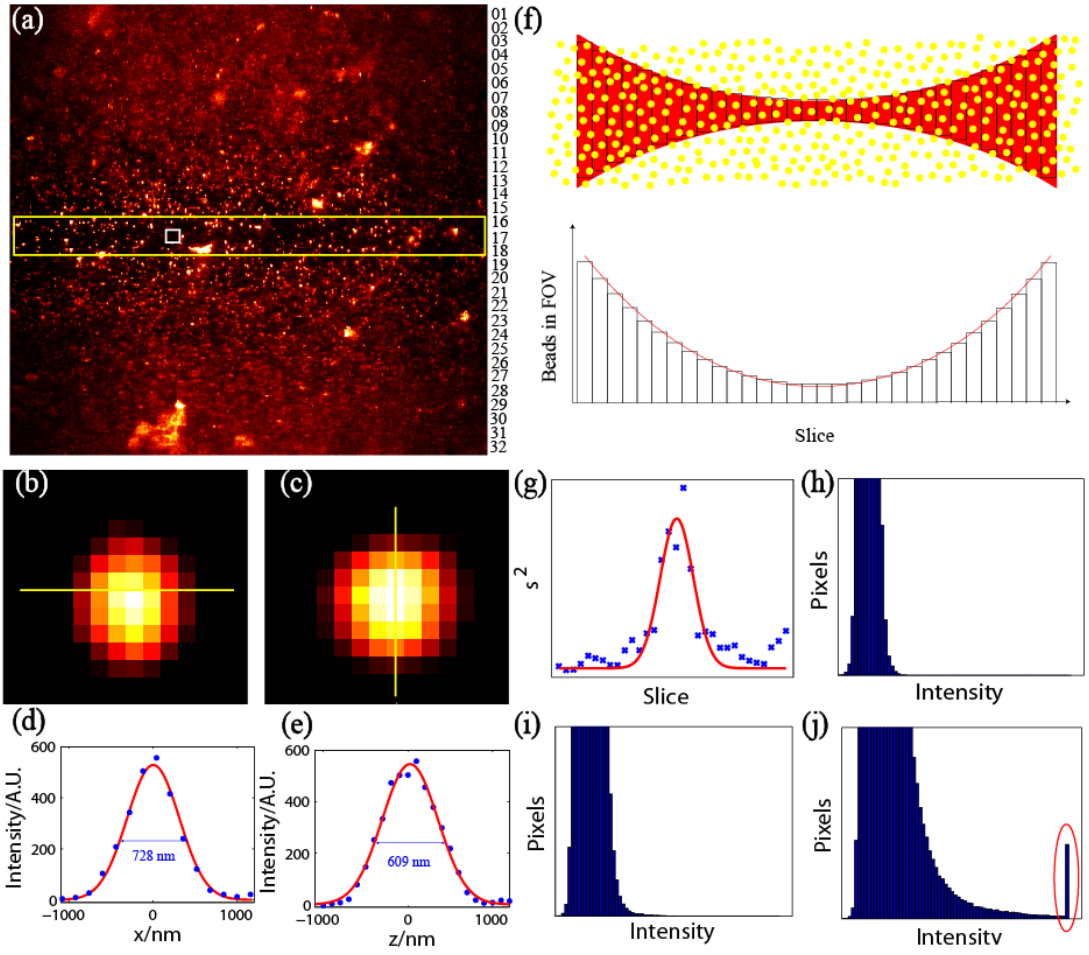

Figure A.3: $0.1\,\mu\mathrm{m}$ fluorescent beads in agarose. (a) $0.1\,\mu\mathrm{m}$ fluorescent beads under light sheet are imaged with a 40X objective (NA=0.6). The yellow box indicates the position of the light sheet. (b) Enlarged image of one bead in the central white solid box of (a). Its intensity plot file is plotted in (d). xz image of this beads is shown in (c) and its intensity profile is in (e).

A.2 Theory and simulations

Numerical simulation is used to estimate our theoretical PSF. For the light sheet lens we used a NA=0.5, $f = 2\,\mathrm{mm}$ acylindrical lens and a NA=0.6, $f = 2.9\,\mathrm{mm}$ air objective. The result of the simulation is plotted in Figure A.2.

A.3 Results

Figure A.3(a) shows the light sheet image of 100 nm Tetraspeck beads. In our system, the thickness of the light sheet is designed to be $< 1\,\mu\mathrm{m}$, and the axial resolution of the imaging objective is $8\,\mu\mathrm{m}$. As shown in Figure A.3, the beads at the central part of the image are much sparser, which is caused by the sectioning of the light sheet shown in a yellow square in Figure A.3(a). The excitation thickness before and behind this layer increases rapidly. As the beads are almost uniformly distributed in agarose, the bead density is proportional to the depth of field: In the central region, axial resolution is determined by the $1\,\mu\mathrm{m}$ light sheet thickness, while in other regions the density is determined by the objective axial resolution which is $8\,\mu\mathrm{m}$. As a result, density in the center area should be 1/8 of other areas. We zoomed in one bead in the central region of z=0 and plotted the XY and Z projection in Figure A.3(b)-(c), respectively. Then in Figure A.3(d)-(e), we measured the lateral and the axial resolution of this system to be both 800 nm. Figure A.4 shows nuclear pore complexes (NPCs) under our light sheet at (a) z=$0\,\mu\mathrm{m}$, (b) z=$4\,\mu\mathrm{m}$ and under wide field microscopy at (c) z=$0\,\mu\mathrm{m}$, (d) z=$4\,\mu\mathrm{m}$. Figure A.5(a) is the image of wide field microscope, and (b)-(c) are light sheet frames from the Vero microtubule sample. In Figure A.5(d), maximum intensity projection is used to reconstruct cells in different frames, and in Figure A.5(e) we show the 3D reconstruction. Compared with wide field results in Figure A.5(a), light sheet results show a significant enhancement in image contrast.

A.4 Conclusions and discussions

In conclusion, we developed a light sheet add-on to conventional microscope systems. It is very easy to install and uninstall, which is useful on shared facilities. Resolution of the system has been estimated by theory and simulation and verified by experiments. Two different methods of mounting cells have been tested. Structures of microtubules and nuclear pore complexes have been observed and compared with wide field images. Better contrast

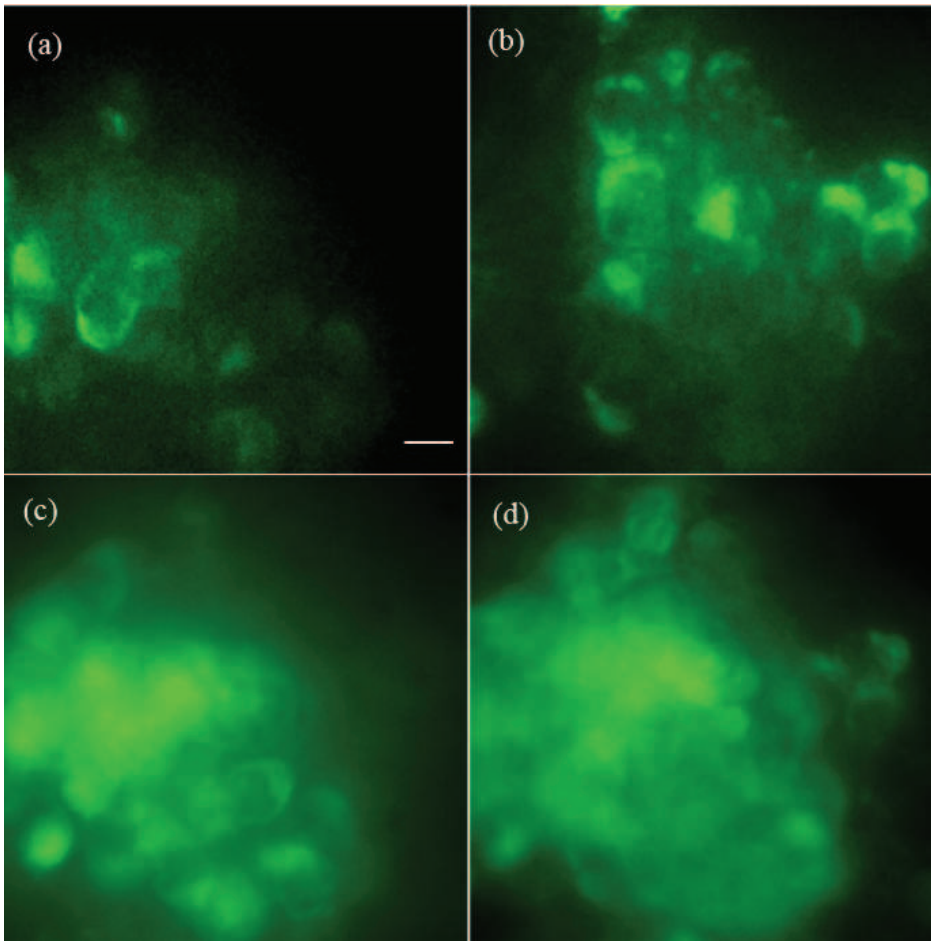

Figure A.4: Vero cells' nuclear pore complexes (NPCs) under our light sheet at (a) z=0 µm, (b) z=4 µm and wide field microscopy at (c) z=0 µm (d) z=4 µm. Images are processed with a median filter to remove shot noise.

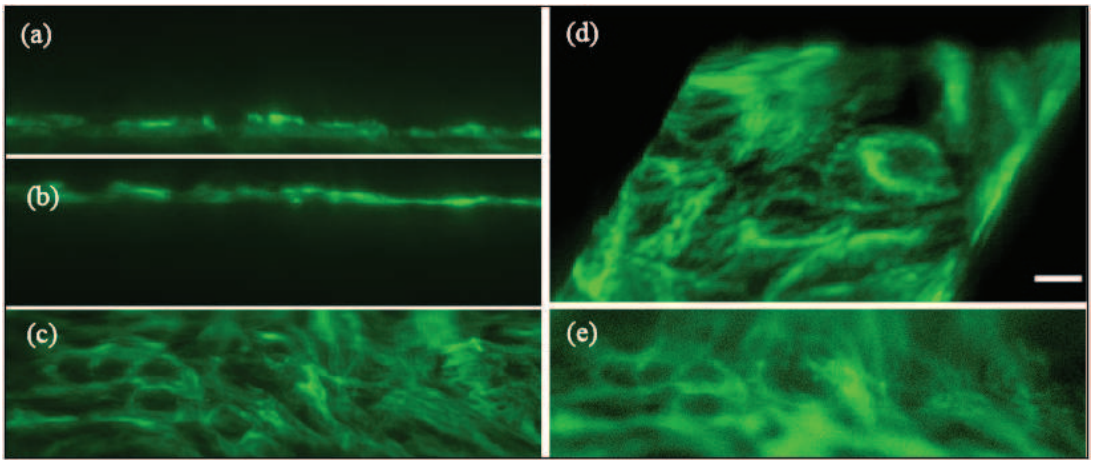

Figure A.5: Light sheet images of Vero cells' microtubules. (a) wide field image of Vero microtubule on a cover glass. (b) and (c)are frames of light sheet image. (c) Maximum intensity projection of 60 frames. (d) 3D reconstruction of the light sheet frames.

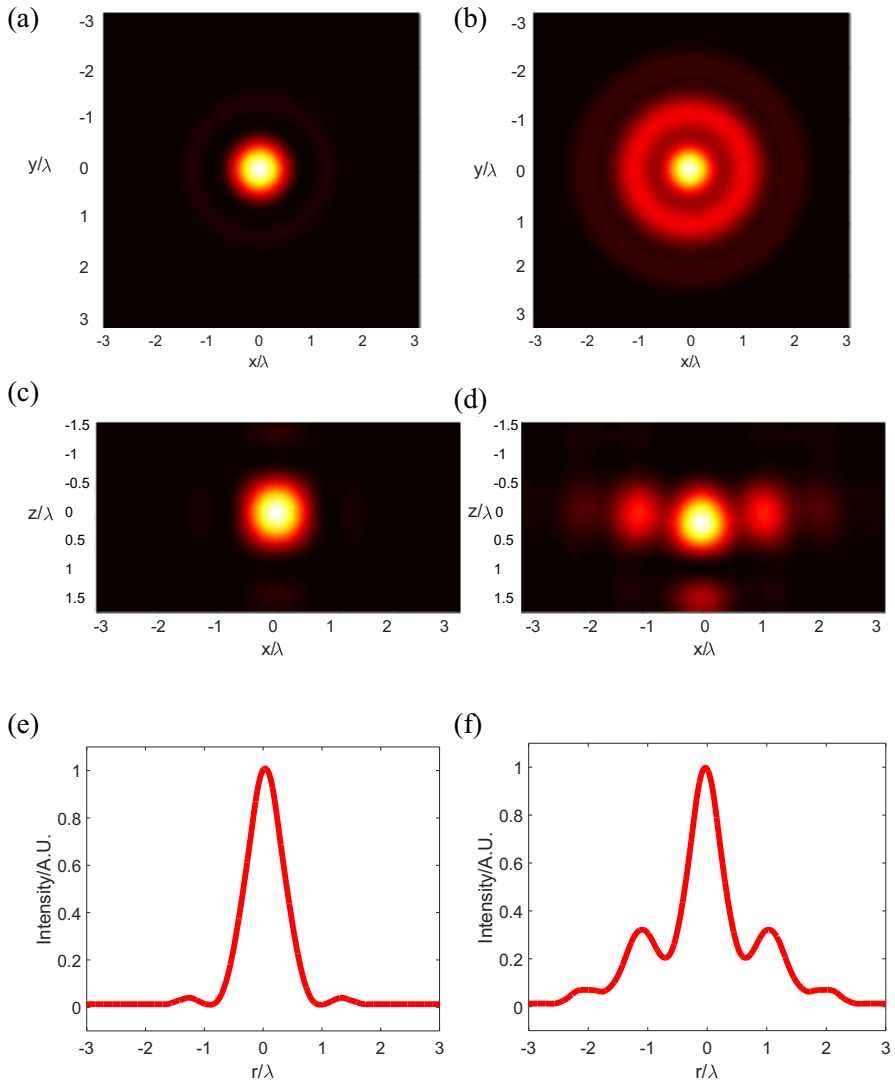

Figure A.6: (a)-(b): Intensity distribution on the focal plane, when the distance between light sheet and the focal plane is $0\,\mu\mathrm{m}$ and $2\,\mu\mathrm{m}$. (c)-(d): Intensity distribution of (a) and (b) on XZ plane.(e)-(f): The lateral intensity distribution of (a) and (b).

has been demonstrated.

A.4.1 Discussion: factors influence the light sheet performances

NA of lenses

The resolution of the light sheet system is determined by both the shape of the light sheet and the resolution of the objective. First, we discuss the factors that decide the shape of the light sheet. According to Gebhardt [85], the length of the light sheet is inversely proportional to NA^2, while the thickness is inversely proportional to NA. So thinner light sheet thickness results in a smaller field of view. In our experiments, the minimum sheet thickness is $1\,\mu\mathrm{m}$, and the corresponding sheet length is $10\,\mu\mathrm{m}$, as shown in Figure A.3. This field of view could be enlarged by moving the sample along the direction of the light sheet, but at the cost of longer exposure time. Ritter et al. [154] used a cylindrical zoom lens to change the light sheet thickness dynamically. Here we used a telescoping pair before the mirror to change the laser diameter statically. For larger samples as tissue or embryos, we could decrease the laser diameter for a larger field of view. In Figure A.8(a), we used a pair of lenses to reduce the diameter of the incident laser to 1 mm. It is shown that the length of light sheet increases, but the contrast enhancement is less significant.

Collimation of the cylindrical and spherical lenses

We showed the alignment of the acylindrical and aspheric lens pair has little impact on the light sheet shape. In Figure A.7, we find that a light sheet could form as long as the horizontal focal point does not overlap with the vertical focal point. After simple geometric optics calculation, it is derived that distance between two focal points is $v - f_1 = f_1^2/\Delta$, where $\Delta = L - f_1 - f_2$, ν is the horizontal focal point, f_1 is the focal length of the aspheric lens and f_2 is the focal length of the acylindrical lens. Then we can estimate the intensity change rate resulted from misaligned lens pair by $\delta|L - f_1 - f_2|/f_1^2$, where δ is the FWHM of the light sheet from the diffraction limit. When the front focal plane of acylindrical lens

overlaps with the back focal plane of the aspheric lens, $L - f_1 - f_2 = 0$, indicating the outgoing optical rays are collimated horizontally. On more general cases, since $L - f_1 - f_2$ is on the same order of f_1, and δ is much smaller than f_1, this number is always much smaller than 1. We conclude that the intensity error resulted from misalignment of the lens pair is always small. As a result, accurate alignment of the lens pair is not necessary. In Figure A.8(b). we directly put the acylindrical lens and spherical lens together. This new setup provided us more flexibility in system design. Further, the width of the light sheet does not change with the position of two lens pair $w = f_1/f_2$

‘

Displacement of the focal plane

From the simulation, we find the width of the light sheet is much smaller than z resolution of the objective. If the central position of the light sheet is z_0, system PSF is approximately given by $D(x, y) = h_{obj}(x, y, z_0)$ when the detection point is inside the region of sheet and $D(x, y) = 0$ if the point is outside. From Figure A.6 we see if the light sheet overlaps with the objective focal plane, the intensity of the primary diffraction maximum is 300 times stronger than the secondary maximum; but this ratio would be only 2 if the light sheet is $2\,\mu\mathrm{m}$ away from the objective focal plane, though the FWHM is almost the same. As a result, we used a piezo stage to ensure perfect overlap of the light sheet plane and the objective focal plane.

Tilt of focal plane

If the light sheet plane is not perpendicular to the objective optical axis, an asymmetric PSF will be generated. Our simulation indicates a 10-degree tilt light sheet will yield a tilt XZ PSF as shown in Figure A.9. However, the system PSF does not change much if we do not consider the defocus effect.

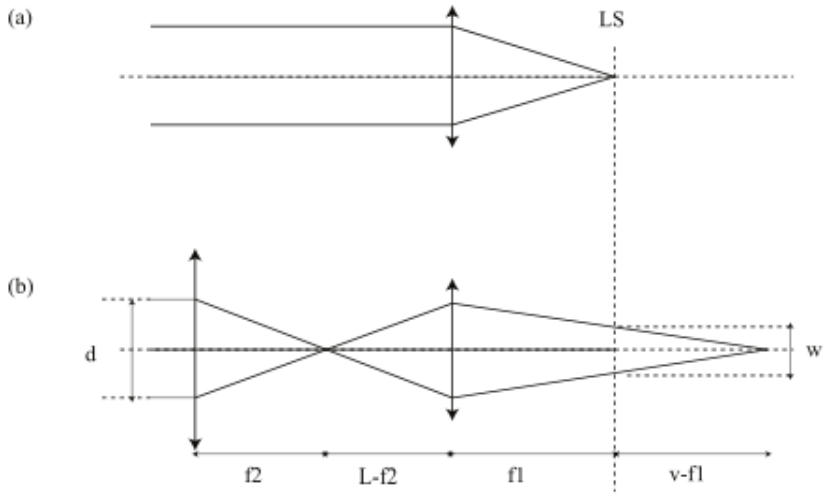

Figure A.7: Optical path of the light sheet. (a) Vertical view of the system. The laser is collimated by an aspheric lens and forms a light sheet at its back focal plane. (b) Horizontal view of the system. When the horizontal focus does not overlap with the vertical focus, a light sheet could be formed at the focal plane of the aspheric lens, as plotted in (b).

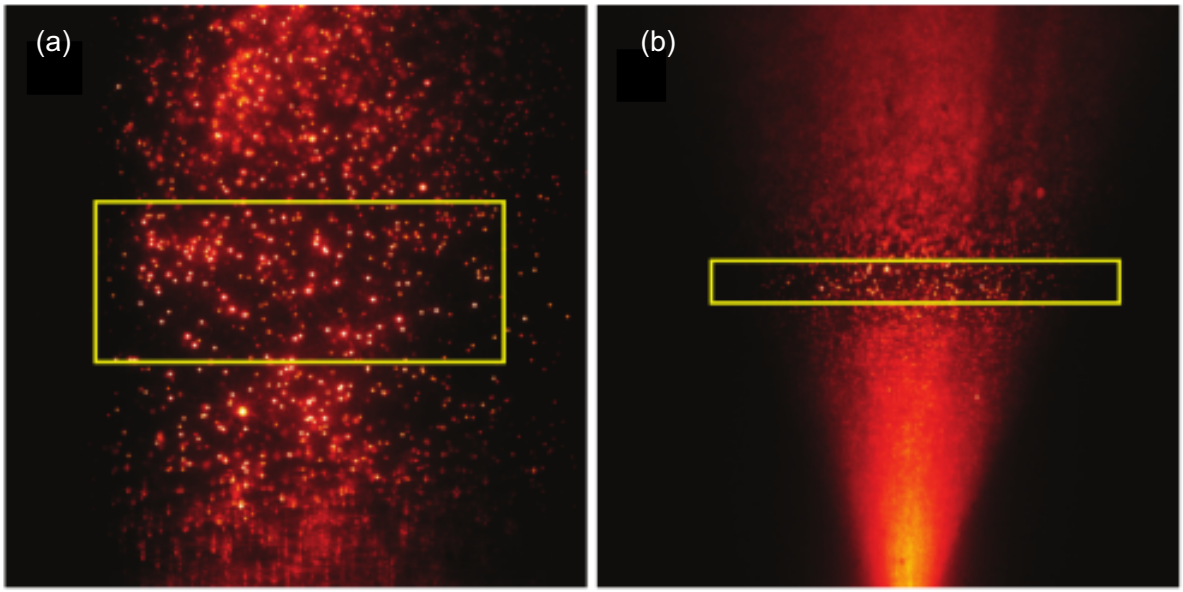

Figure A.8: Fluorescent beads under a thicker light sheet. All system parameters are the same as in A.3, except laser beam diameter is reduced to 1 mm. (b) Fluorescent beads under an inhomogeneous light sheet. Instead of the previous lens pair, we used a $f = 20\,\mathrm{mm}$ cylindrical lens just before the aspheric lens.

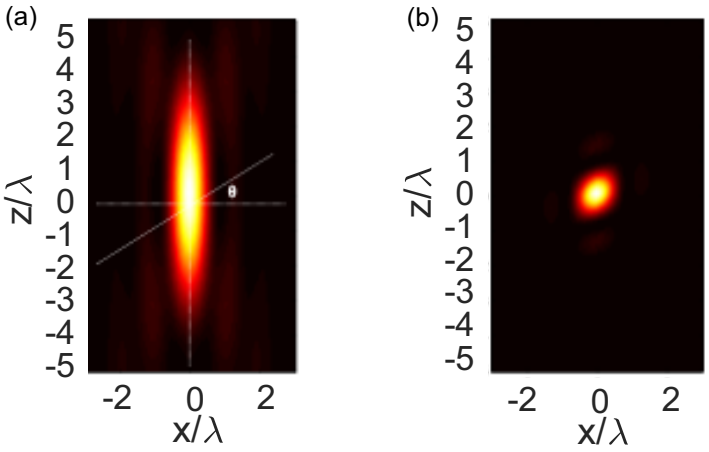

Figure A.9: Tilt light sheet resulted in a tilt PSF. (a) is the objective PSF, (b) is the overall PSF, and θ is the tilt angle of the light sheet .

Mismatch of refractive index

Mismatch of the refractive index could impact the system resolution. For simplicity, we use the 1D model to simulate this effect. Under paraxial approximation, the transverse field only changes a constant factor after refracted by the boundary [92]. The incident field is $A(x) = \exp(\mathrm{i}n_0 k\sqrt{x^2+f^2})$, while the propagator is given by $g(x,x') = \exp(\mathrm{i}n_1 k\sqrt{(x-x')^2+z_2})$. Refracted focal plane is approximately given by fn_1/n_0. According to our simulation, we take $n_0 = 1$ and $n_1 = 1.3$. In Figure A.10 we plot the thickness of the light sheet with respect to water depth. It is shown that for air objective, deeper immersion in water results in poorer resolution. As a result, water immersion objectives or water dipping objectives are better for light sheet systems for in-vivo biological applications. Further, for an air objective, a displacement between the light sheet and the objective focal plane may happen during axial scanning, resulted from the refractive index mismatch. If the sample is immersed in the medium with refractive index n and the distance between the coverglass and objective is L, the focal plane would be $d = n(f-L)$ above the coverglass, which gives $\Delta d = n\Delta L$. As a result, the focal plane of the objective does not shift simultaneously with sample and light sheet, and synchronization

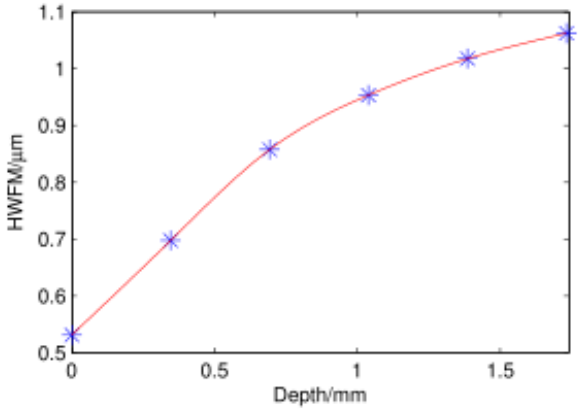

Figure A.10: Lateral resolution of microscope systems deteriorates when the immersion depth increases.

is required for a large axial field of view.

APPENDIX B

DERIVATION ON THE STED SQUARE ROOT LAW

This chapter introduces the STED square root law discussed in Chapter 2. This derivation has been published in Reference [96].

B.1 Approximation to the square root law

The square root law is derived from Taylor Series [101]. Now consider the light intensity distribution on focal plane $z_p = 0$. Since $J_\nu(x) = \Sigma_{k=0}^{\infty} \frac{(-1)^k}{k!\Gamma(k+\nu+1)}(\frac{x}{2})^{2k+\nu}$, the approximation to the second-order can be used: $J_0(x) = 1 - \frac{x^2}{4}$, $J_1(x) = \frac{x}{2}$, and $J_2(x) = \frac{x^2}{8}$. If we define $s = \sin^2\alpha$ and
$B(s,p,q) = \int_0^s t^{p-1}(1-t)^{q-1}\mathrm{d}t = 2\int_0^\alpha \sin^{2p-1}\theta\cos^{2q-1}\theta\mathrm{d}\theta$, which is the incomplete Beta function, we can express $I_1 - \mathcal{I}_5$ as polynomials of ρ_p with their coefficients given by $a_{01} - b_5$, and their coefficients are incomplete Beta functions of s, as shown in the last section of this chapter. For a linearly or elliptically polarized laser, it is always possible to rotate coordinates to make the polarization a standard ellipse with $A_{1x} = C_1$, $A_{1y} = \mathrm{i}C_2$, $A_{2x} = D_1$, $A_{2y} = \mathrm{i}D_2$, where C_1, C_2, D_1, D_2 are real. Then the excitation and STED doughnut intensities can be expressed as:

$$\begin{cases} I_{ex}(\rho_p,\phi_p) = (C_1^2+C_2^2)a_{01}^2 + 2[(C_1^2+C_2^2)(a_{01}a_{02}+a_1^2) \\ \qquad\qquad + (C_1^2-C_2^2)(a_{01}a_2+a_1^2)\cos 2\phi_p](k_1\rho_p)^2 \\ I_{dep}(\rho_p,\phi_p) = (D_1-D_2)^2 b_{41}^2 + (D_1^2+D_2^2)b_1^2(k_2\rho_p)^2 \\ \qquad\qquad + (D_1-D_2)^2(\frac{1}{2}b_2^2 + 2b_{41}b_{42})(k_2\rho_p)^2 \\ \qquad\qquad - (b_1b_2+2b_{41}b_5)(D_1^2-D_2^2)\cos 2\phi_p(k_2\rho_p)^2 \end{cases} \tag{B.1}$$

This expression gives an analytical description of the excitation and depletion intensi-

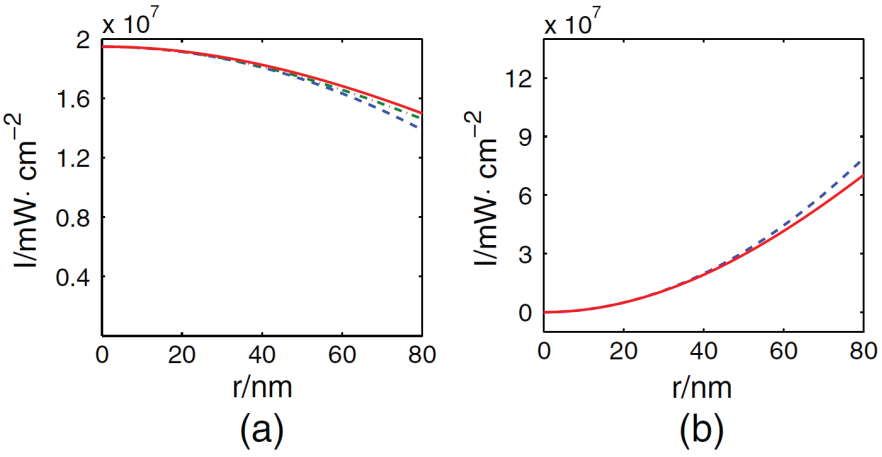

Figure B.1: The intensity profile of (a) excitation and (b) depletion beams on the x-axis of the focal plane. Simulation intensities are plotted in red solid, polynomial approximation of Equation (B.1) are plotted in blue dashed, and the exponential approximation is plotted in green in (a) [96].

ties in the vicinity of the focus. A special case is that the depletion beam is left-hand circularly polarized (the same as the direction of the vortex direction) with $C_1 = C_2 = \frac{\sqrt{2}}{2}C$ and $D_1 = D_2 = \frac{\sqrt{2}}{2}D$, which indicates that the center of donut has zero intensity. Then $I_{ex} = C^2[a_{01}^2 + 2(a_{01}a_{02} + a_1^2)(k_1\rho)^2]$ and $I_{dep} = D_1^2 b_1^2 (k_2\rho)^2$. For an elliptically polarized laser or linearly polarized laser [155], $D_1 \neq D_2$ leads to $I_{de} \neq 0$ at the focus. This is derived from the second-order approximation, but still, holds true for a strict analytical solution because all the higher-orders annihilate at $r = 0$. The results obtained with our methods can also be validated as shown in Figure 2.3. The full-width at half-maximum (FWHM) of STED PSF could be estimated accordingly, with the decay functions for CW or pulse cases described in the next section.

Finally, we can build the relationship between depletion light intensity and achievable resolution. Stimulated emission intensity I_s is often defined as the intensity of fluorescence dropped into its half [101, 156], or 1/e [123, 157]. Here we use the former definition. Using $\exp(-\ln 2x^2) \approx 1/(1 + x^2)$, we wrote both excitation intensity and the extinction function

into Gaussian. After trivial calculation, we derived [156]:

$$FWHM = \frac{\lambda_{ex}}{\alpha NA\sqrt{1+\beta I_{dep}/I_s}} \tag{B.2}$$

where I_{dep} is the non-modulated peak intensity of the depletion beam focus, and $\alpha = \pi\sqrt{-2(a_{01}a_{02}+a_1^2)/(\ln 2)}/a_{01}s$, $\beta = \frac{(\ln 2)b_1^2}{2(a_{01}a_{02}+a_1^2)}(\frac{\lambda_{ex}}{\lambda_{de}})^2$. For $NA = 1.4$ and $n = 1.5$, $\lambda_{ex} = 635\,\mathrm{nm}$, $\lambda_{de} = 760\,\mathrm{nm}$, this expression yields $FWHM = \lambda_{ex}(1{+}0.233I_{dep}/I_s)^{-1/2}/1.83NA$.

Use depletion power to predict resolution

Now all parameters could be directly measured in experiments except the saturation intensity I_s. In reality, single fluorophores are easy to bleach, so the measurement of I_s is often replaced by the measurement of saturation power P_s in solutions:

1. Measure the average fluorescence intensity of the excitation beam by scanning the focus across the fluorescent solution with uniform distribution [100, 101];

2. Introduce the depletion beam without phase modulation, whose PSF should be overlapped with the PSF of the excitation;

3. Adjust the depletion power until the total fluorescence intensity is depleted to its half [100, 101].

Therefore, it is more convenient to express the resolution of STED with the relationship of $P/\mathcal{P}_s$, where P is the depletion power and $\mathcal{P}_s$ is defined by the depletion power when the detected integrated fluorescence intensity (scanning across solution) is reduced by half. The detected integrated fluorescence could be calculated by $I = \iiint i_{illum}(x,y,z)h_{det}(x,y,z)\mathrm{d}V$, where $h_{det}(x,y,z)$ is the detection PSF. Assuming we use a point detector and omit the Stokes shift of fluorescence, numerical evaluation of the factor reveals $P = \mathcal{P}_s$ approximately corresponds to $I = 2I_s$. Then the resolution vs. STED power relationship becomes [100,

102]

$$FWHM = \frac{\lambda_{ex}}{\alpha NA\sqrt{1+\chi P/\mathcal{P}_s}} \tag{B.3}$$

where P is the depletion power, $\mathcal{P}_s$ is the saturation power when the fluorescence is reduced by half. Our representation of resolution then becomes
$FWHM = \lambda_{ex}/(1.82NA\sqrt{1+0.45P/\mathcal{P}_s})$.

B.2 Discussions

In this section we have applied a polynomial approximation of the Bessel integrals, to yield an analytical expression of STED with vectorial waves. The results were validated with previously reported numerical simulations of the electromagnetic wave. The relationship of $1/\sqrt{1+I/I_s}$ has been validated in both CW and pulsed STED cases. We have given new sets of resolution estimation equations, to predict the resolution achievable for a STED system: the expression of resolution, the incident depletion intensity, and the half-peak-fluorescence depletion intensity is analytically derived with incomplete Beta functions, and the relationship of the half-peak-fluorescence depletion intensity and the half-total-fluorescence depletion power was established by simulations. The result can be extended to other RESOLFT type super-resolution techniques where the fluorescence point spread function is modulated with another doughnut shape point spread function through 0-2π phase modulation.

We used STED3D to simulate the electromagnetic field distributions around the focus. In Figure B.1 we plotted the excitation (a) and the depletion (b) intensities on the x-axis in the focal plane. In (a) the simulation intensity was plotted in red, the polynomial approximation of Equation B.1 was plotted in blue, and the exponential approximation was plotted in green. In Figure B.1(b) the numerical solution to the rigid EM field intensity was plotted in red, and the polynomial approximation of Equation B.1 was plotted in blue.

As expected, approximations agree well with the numerical solution of the EM field in the vicinity of focus. This is because in the derivation of Equation B.2, asymptotic expansion at $r = 0$ makes the approximation only available in the vicinity of the focus. In Figure B.1 we found that the curves of analytical and simulation laser intensity overlapped well when r was small but they diverged with the increase of r. In Figure B.1 we found that when $r < 80\,\mathrm{nm}$, the approximated excitation and depletion intensities will induce errors of 5% and 8%, respectively. As a result, our theory applies to high aperture objective lenses with $NA > 1$, or those with high depletion intensity, roughly when the FWHM is less than $\lambda/3$. For smaller aperture objective lens, Watanabe's theory [158] with scalar diffraction theory [31, 93] can provide an acceptable estimation. For the same reason, The analytical FWHM curves better predicts results with an error less than 5% when $I > 10I_s$. With the development of the high-efficiency fluorescent dye and through applications of larger STED power, STED resolution of 6 nm has been demonstrated [159], and standard STED system resolution is $< 80\,\mathrm{nm}$. As usually the best STED nanoscopy resolution at a certain depletion power is concerned, rather than the resolution at moderate power, our result has a wide scope of application in the accurate estimation of the STED (or RESOLFT) system performance.

B.3 Specific derivations

To analytically derive the field of a circularly polarized incident laser, it is necessary to note that in the rotated coordination, Equation 2.15 still holds with phase mask function $\mathrm{e}^{\mathrm{i}k\Phi(\theta',\phi')} = 1$ for the excitation beam and $\mathrm{e}^{\mathrm{i}k\Phi(\theta',\phi')} = \mathrm{e}^{\mathrm{i}(\phi'+\frac{\pi}{2})}$ for the depletion beam. It yields

$$\begin{cases} e'_{1x'}(P) = -\mathrm{i}A_{1y}(I_0 - I_2\cos 2\phi_p) \\ e'_{1y'}(P) = \mathrm{i}A_{1y}I_2\sin 2\phi_p \\ e'_{1z'}(P) = -2A_{1y}I_1\sin\phi_p \end{cases}$$

for excitation and

$$\begin{cases} e'_{2x'} = A_{2y}[\mathcal{I}_1 \exp(\mathrm{i}\phi_p) + \frac{1}{2}\mathcal{I}_2 \exp(-\mathrm{i}\phi_p) - \frac{1}{2}\mathcal{I}_3 \exp(\mathrm{i}3\phi_p)] \\ e'_{2y'} = \frac{\mathrm{i}A_{2y}}{2}[\mathcal{I}_2 \exp(-\mathrm{i}\phi_p) + \mathcal{I}_3 \exp(\mathrm{i}3\phi_p)] \\ e'_{2z'} = -A_{2y}[\mathcal{I}_4 + \mathcal{I}_5 \exp(\mathrm{i}2\phi_p)] \end{cases}$$

for depletion.

In Equation B.1 the parameters are defined as

$$\begin{cases} I_0 = a_{01} + a_{02}(k_1\rho_p)^2 \\ I_1 = a_1(k_1\rho_p) \\ I_2 = a_2(k_1\rho_p)^2 \\ \mathcal{I}_1 = b_1(k_2\rho_p) \\ \mathcal{I}_2 = b_2(k_2\rho_p) \\ \mathcal{I}_3 = 0 \\ \mathcal{I}_4 = b_{41} + b_{42}(k_2\rho_p)^2 \\ \mathcal{I}_5 = b_5(k_2\rho_p)^2 \end{cases} \tag{B.4}$$

where $a_{01} = [B(s,1,3/4) + B(s,1,5/4)]/2$,$a_{02} = [B(s,2,3/4) + B(s,2,5/4)]/8$, $a_1 = B(s,2,3/4)/4$, $a_2 = [B(s,2,\frac{3}{4}) - B(s,2,\frac{5}{4})]/16$, $b_1 = [B(s,3/2,3/4) + B(s,3/2,5/4)]/4$, $b_2 = [B(s,3/2,3/4) - B(s,3/2,5/4)]/4$, $b_{41} = B(s,3/2,3/4)$, $b_{42} = B(s,5/2,3/4)/4$, $b_5 = B(s,5/2,3/4)/8$.

To obtain Equation B.3 it is important to keep in mind that without the phase plate $I_{dep} = D^2 a_{01}^2$. If we defined the depletion power as D_s^2 when peak fluorescence intensity into a half, we also have $I_s = D_s^2 a_{01}^2$. So the depletion later power D^2/D_s^2 in Equation B.2 is equivalent to the peak intensity ratio I_{dep}/I_s in Equation B.3. Finally, $I_{ex}(\rho)\eta(I_{dep}(\rho)) = I_{ex}(0)/2$, $\eta(I_{dep}) = \exp(-\ln 2 I_{dep}/I_s)$, $I_{ex} = C^2 a_{01}^2 \exp[2(a_{01}a_{02} + a_1^2)(k_1\rho)^2/a_{01}^2]$ and

$I_{dep}(\rho) = D_1^2 b_1^2 (k_2\rho)^2$ yield

$$FWHM = \frac{\lambda_{ex}}{\pi n \sqrt{\frac{-2(a_{01}a_{02}+a_1^2)}{(\ln 2)a_{01}^2}} \sqrt{1 - \frac{(\ln 2)b_1^2}{2(a_{01}a_{02}+a_1^2)} (\frac{\lambda_{ex}}{\lambda_{de}})^2 \frac{I_{STED}}{I_s}}} \tag{B.5}$$

Then in Equation B.3 the factors α and β can be obtained.

APPENDIX C
SOFTWARE CONTROL AND SOME DISCUSSION OF MLA COUPLED LIGHT SHEET

In this chapter, we introduce the controlling software design and the microlens array alignment protocol in Chapter 5.

C.1 Software control

First we need to import the API from Andor and Thorlabs. For Andor, install the Andor Solis and do the following as described in the Andor software development kit:

1. Select the menu item "Tools"→ "Advanced" → "Edit Palette Views...".
2. Right Click on the Functions tool bar and select "Insert" → "Submenu...".
3. In the dialog select "Link to LLB library...".
4. Navigate to the "user.lib" directory and select "atmcd32d.llb", the submenu with all SDK functions has been added.
5. Right click on the new palette view and select "Rename Submenu...".
6. Change the name to "Andor SDK".
7. Repeat steps 2-6 for the Controls tool bar.

For Thorlabs piezo stage, it should be noticed that Microsoft.NET Framework 4.5 and Microsoft Visual C++2012 Redistributable (x86) must be installed before you install Thorlabs Kinesis (32 bit). Otherwise, it will report the error "Thorlabs. MotionControl. DeviceManager. dll or its dependent module not found". Once the Kinesis is installed, do the following:

1. Copy all the files in your installed folder of Kinesis to your Labview project folder.

2. On the Controls palette, select the ".NET and ActiveX palette", and drag ".NET container" to the front panel.

3. Right click on the container, choose "Insert .NET Control" and add "TCubePiezoControl" and "TCubeStrainGauge" separately.

4. To create a property node, right click the object on the block diagram, and choose ".NET Platte". Use a similar way to create a invoke node for methods.

In Figure C.1 we present the main loop of the program. An event structure is used in a while loop, so a user's click on "Start" button would be monitored. We set some Boolean variables to record the state of each equipment. Before the start of each task, we check if all the equipment is accessible in the subVI, in which a Boolean 2D matrix is maintained. Then the date acquiring process could begin. We will discuss the galvanometer scanning and piezo scanning units in detail.

The galvanometer scanning unit is shown in Figure C.2. Port of the data generation is configured as ao0:1, which indicates two output channels will be used. Then the clock is set to be continuous sampling, and the onboard clock would be used as the synchronization source. A waveform with two channels is input to the N-channel N-sample task, and the task could be started. The scanning will continue until we set the pause scanning button to false.

For more flexible scanning we use an 8-bit image as the input. We read an image from disk and transform it into a 2D array. At the same time, the image is shown on the screen, as shown in Figure C.4. The 2D matrix is rearranged into two raster scanning waveform arrays with MathRT nodes.

Before taking a 3D image, the piezo stage and camera need to be configured. The configuration of the piezo stage is plotted in Figure C.2. Serial numbers (read from Thorlabs Kinesis software) should be input, and the device could be created in Labview. Mode of

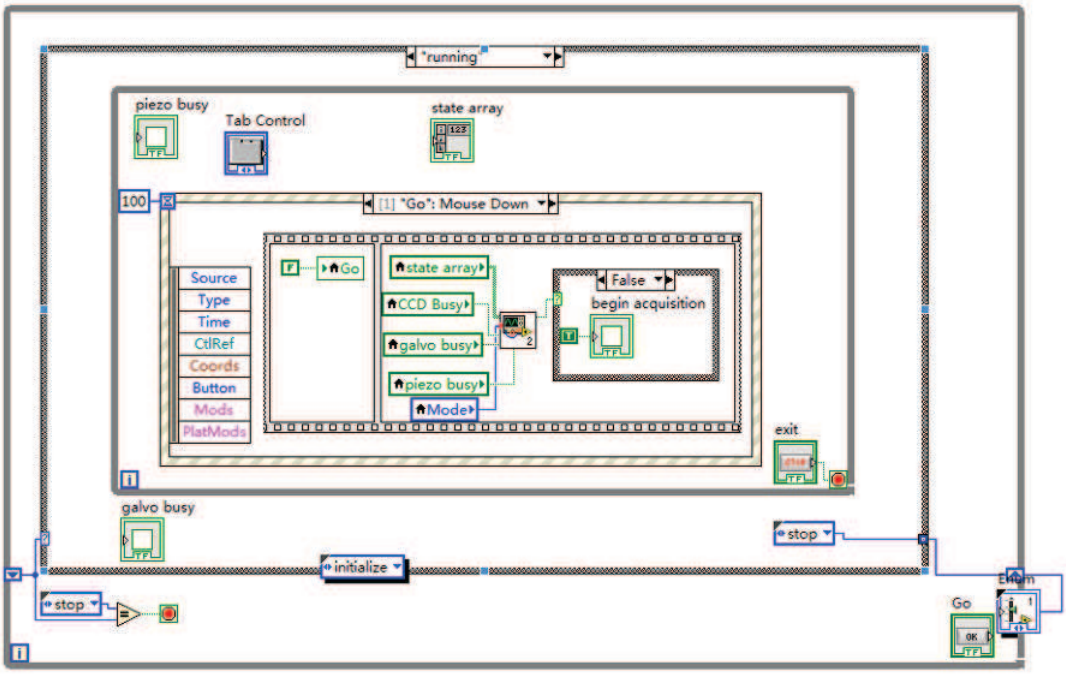

Figure C.1: The main loop of the light sheet controlling program.

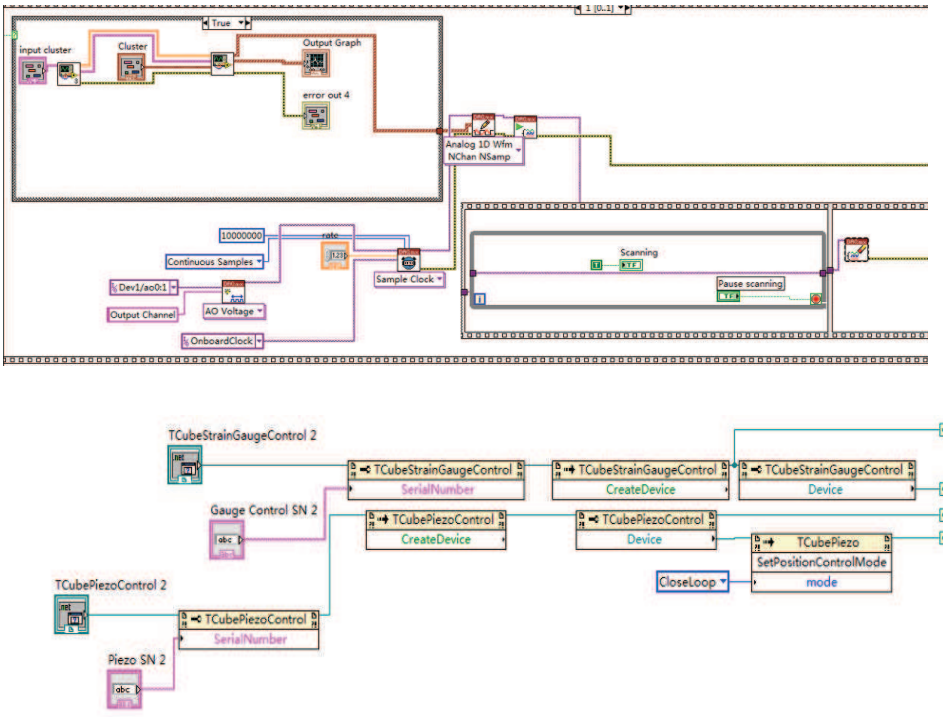

Figure C.2: Initialize of galvanometer and piezo stage.

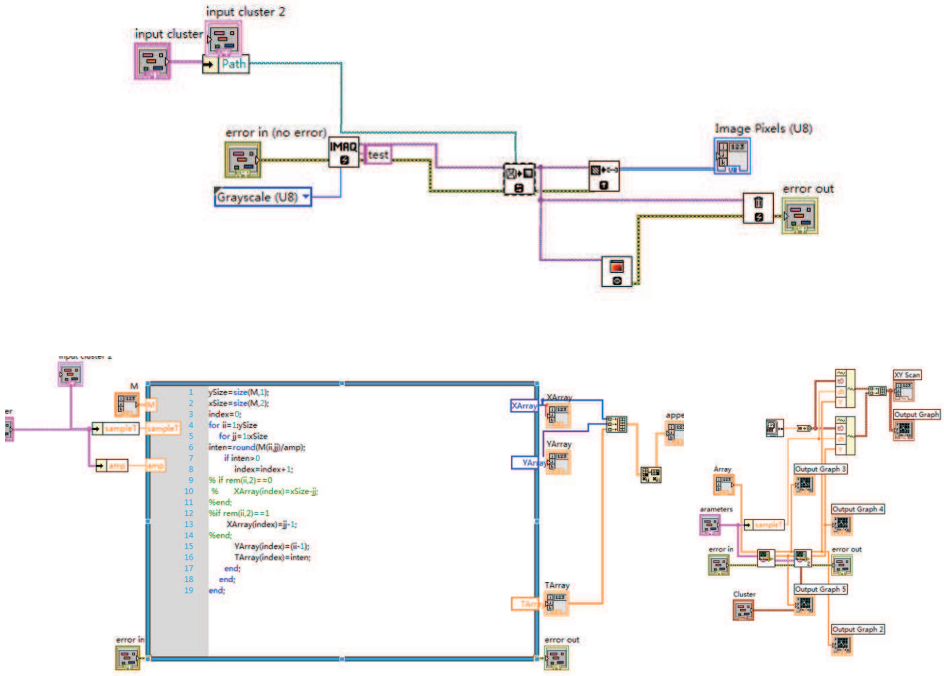

Figure C.3: Reading an image as the galvanometer controlling signal. The images are transformed into two arrays for XY signal.

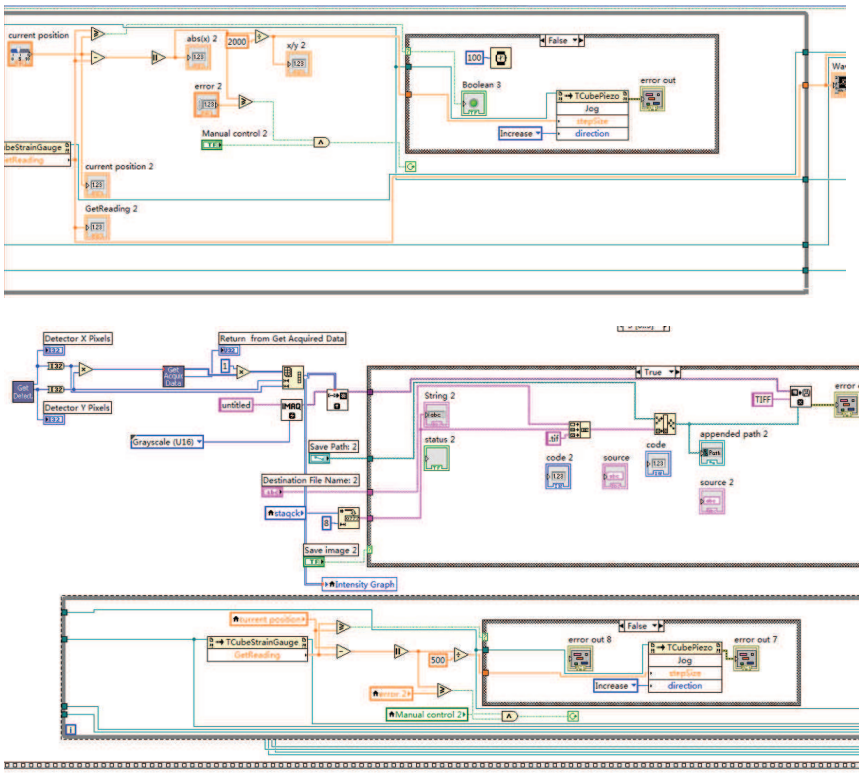

Figure C.4: Taking and saving images, and jogging of the piezo stage.

the piezo stage could be chosen to be open loop or close loop. For the camera, acquisition parameters such as single image mode, trigger mode, shutter mode, exposure time and EM gain could be set here.

Next step is to move the piezo stage. We use the "getReading" function to get the current position of gauge reader and compare it with the position we set. We choose to increase or decrease the voltage by calling the "Jog" function, and the step size depends on the difference of those two positions. This process will continue until the difference of the current position and the preset position is less than error. Then we start the acquisition of the camera as shown in Figure C.4, and save the images on disk. Finally, it is important to close the devices with a "shutdown" method, which is not shown here.

C.2 Spatial resolution of MLA

Let's consider a point source at location (x, y, z). We assume this source is far above the focal plane, i.e. $z \gg f/M^2$. In this case, diffraction patterns could be observed behind the MLA with diameter $\Delta x = \lambda/2(P/2f) = \lambda f/P$, which corresponds to uncertainty in the reconstruction angle $\Delta\theta = \Delta x/f = \lambda/P$. Here P is the pitch size of MLA. After the refocus algorithm, reconstruction resolution could be derived from this angular uncertainty

$$L = 2NAz\frac{1}{k} + P \tag{C.1}$$

where k is the ratio of lenslet pitch size over the objective's optical diffracting limit $P = kM\lambda/2NA$ and M is the amplification factor of the microscope system. When $k = 1$, the first term on right $2NAz$ is the divergent angle without the microlens array. So the role MLA plays is to "refocus" optical rays.

This analysis holds true when the geometric image of this point is smaller than its

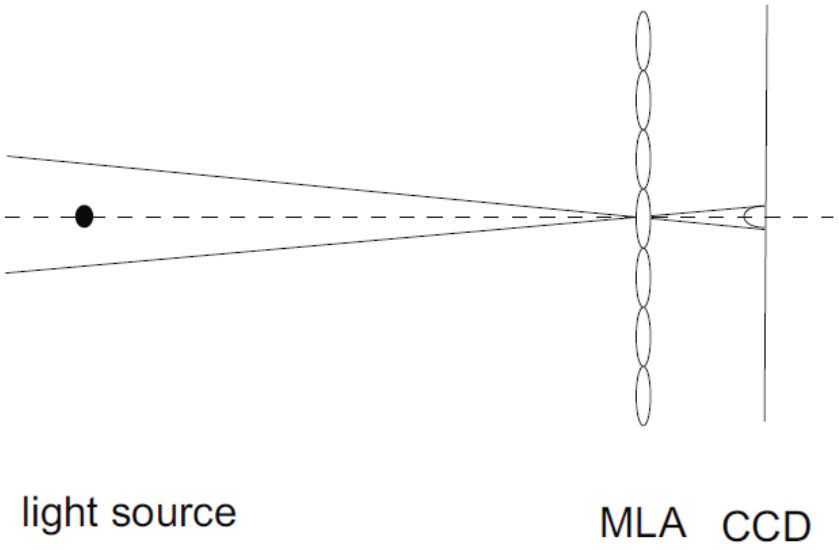

Figure C.5: Reconstruction of a point source. A point source generates a diffraction pattern on the CCD plane, which corresponds to a reconstruction region in the object space.

Table C.1: Reconstruction accuracy of light field microscopy

z position	Lateral reconstruction resolution	Axial reconstruction resolution
$\|z\| > z_c$	$\Delta L = 2NAz/k + P/M$	$\Delta L/NA$
$f/M^2 < \|z\| < z_c$	$\Delta L = 2P/M$	$\Delta L/NA$
$\|z\| < f/M^2$	$\Delta L = 2P/M$	N.A.

diffraction limit, that is

$$\begin{cases} \dfrac{1}{u} + \dfrac{1}{v} = \dfrac{1}{f} \\ L = P(v-f)/v \end{cases} \tag{C.2}$$

It could be calculated $L = Pf/u$ and we write down the critical condition as $L = M\lambda/2NA$. Applying the numerical aperture matching condition $NA/M = P/2f$, it is derived

$$z_c = \frac{1}{M^2}\frac{P^2}{\lambda} = \frac{k^2}{2}\frac{\lambda}{2NA^2} \tag{C.3}$$

Another extreme case is when $|z| < f/M^2$. All light from this point is collected by a single lens and axial reconstruction capacity of system lost. A summary of the reconstructed resolution is listed in Table C.1.

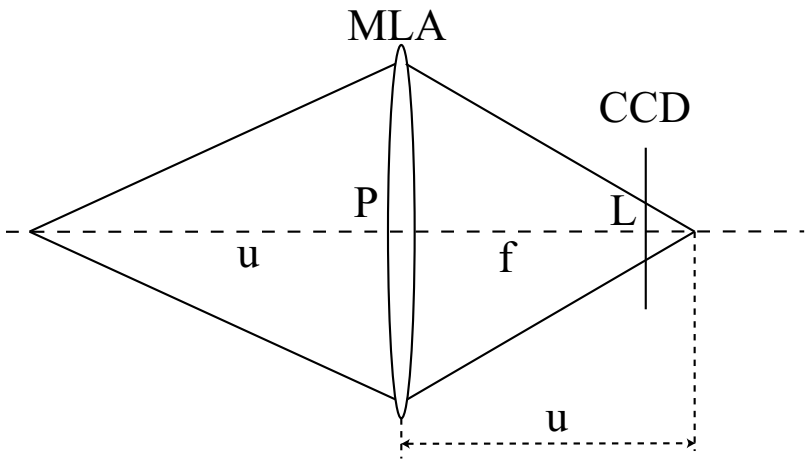

Figure C.6: Geometry image of a point. u: distance from the object to the MLA. v: distance from the MLA to the image of the point sources. P: pitch size of the MLA. f: focal length of the MLA. L: diameter of the point source on the CCD plane.

C.3 Troubleshooting

C.3.1 Find the focal plane of MLA

Light field microscopy requires the MLA to be conjugated to the intermediate plane of the microscope and CCD to be on the focal plane of MLA. It is easy to estimate the precision of both alignments is on the order of mm. The requirement on MLA position results from the fact that aberrations are best corrected on the focal plane of the objective lens. For high-quality objectives, we expect aberrations are well corrected near the focal volume so that this requirement could be broken. On the contrary, the conjugation of the CCD and the MLA focal plane has to be strictly guaranteed, or reconstruction may fail.

We adjust the position of optical elements following this procedure:

1. Roughly overlap the MLA with the intermediate plane of the microscope and put the CCD on the focal plane of MLA.

2. Put a mirror on the sample stage.

3. Adjust the position and orientation of the CCD to maximize the focal intensity.

The method works because the laser incidents almost orthogonally on the MLA.

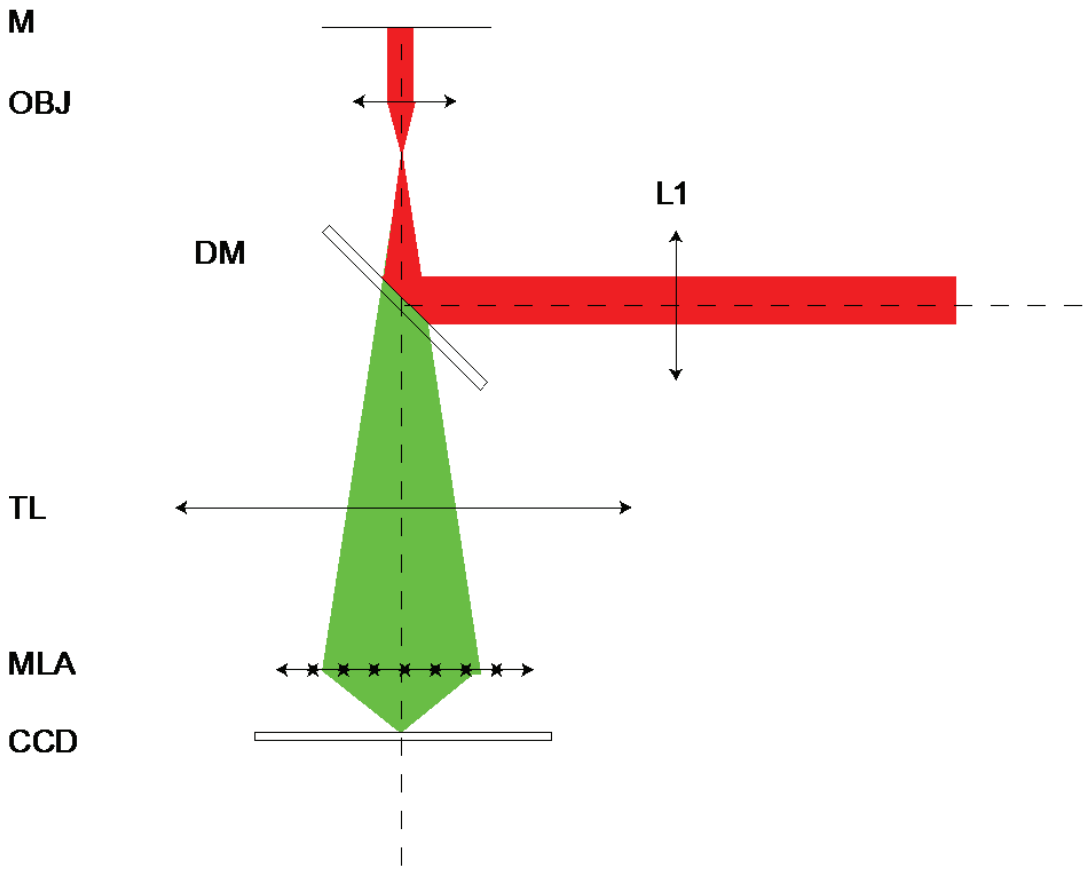

Figure C.7: Adjustment of MLA. M: mirror, OBJ: objective, DM: dichroic mirror, TL: tube lens, L1: lens. CCD should be located on the plane that reflected light intensity reaches its maximum.

APPENDIX D
COPYRIGHT PERMISSIONS

D.1 From Nature Publishing Group

Figures and parts of text in Chapter 3 are from Yang, Xusan, **Hao Xie**, Eric Alonas, Yujia Liu, Xuanze Chen, Philip J. Santangelo, Qiushi Ren, Peng Xi, and Dayong Jin. "Mirror-enhanced super-resolution microscopy." Light: Science & Applications 5, no. 6 (2016): e16134. This is the permission from NPG:

The request you have made is considered to be non-commercial/educational. As the article you have requested has been distributed under a Creative Commons license (Attribution-Noncommercial), you may reuse this material for non-commercial/educational purposes without obtaining additional permission from Nature Publishing Group, providing that the author and the original source of publication are fully acknowledged (please see the article itself for the license version number). You may reuse this material without obtaining permission from Nature Publishing Group, providing that the author and the original source of publication are fully acknowledged, as per the terms of the license. For license terms, please see http://creativecommons.org/.

D.2 From OSA

Section 4.2-4.4 are from **Xie, Hao**, Dayong Jin, Junjie Yu, Tong Peng, Yichen Ding, Changhe Zhou, and Peng Xi. "Schlieren confocal microscopy for phase-relief imaging." Optics Letters 39, no. 5 (2014): 1238-1241.

Figure 4.7 is from Ding, Yichen, **Hao Xie**, Tong Peng, Yiqing Lu, Dayong Jin, Junlin Teng, Qiushi Ren, and Peng Xi. "Laser oblique scanning optical microscopy (LOSOM) for

phase relief imaging." Optics Express 20, no. 13 (2012): 14100-14108.

Section 2.2 and Appendix B are from **Xie, Hao**, Yujia Liu, Dayong Jin, Philip J. Santangelo, and Peng Xi. "Analytical description of high-aperture STED resolution with 0C2 vortex phase modulation." JOSA A 30, no. 8 (2013): 1640-1645.

Following is the permission letter from OSA copyright editor:

Dear Hao Xie,

Thank you for contacting The Optical Society.

Because you are the author of the source paper from which you wish to reproduce material, OSA considers your requested use of its copyrighted materials to be permissible within the author rights granted in the Copyright Transfer Agreement submitted by the requester on acceptance for publication of his/her manuscript. It is requested that a complete citation of the original material be included in any publication. This permission assumes that the material was not reproduced from another source when published in the original publication.

OSA considers this email to be sufficient authorization for the use of the requested material.

Let me know if you have any questions.

Kind Regards,

Rebecca Robinson

December 2, 2016

Authorized Agent, The Optical Society

REFERENCES

[1] A. van Leeuwenhoek, "Part of a letter from mr antony van leeuwenhoek, frs concerning green weeds growing in water, and some animalcula found about them," *Philosophical Transactions*, vol. 23, no. 277-288, pp. 1304–1311, 1702.

[2] D. B. Williams and C. B. Carter, "The transmission electron microscope," in *Transmission Electron Microscopy*, Springer, 1996, pp. 3–17.

[3] C. B. Carter and D. Williams, *Transmission Electron Microscopy*. Springer-Verlag US, 2009.

[4] R. C. Burghardt and R. Droleskey, "Transmission electron microscopy," *Current Protocols in Microbiology*, 2B–1, 2006.

[5] L. Reimer, *Transmission Electron Microscopy: Physics of Image Formation and Microanalysis*. Springer, 2013, vol. 36.

[6] Z. Wang, "Transmission electron microscopy of shape-controlled nanocrystals and their assemblies," *The Journal of Physical Chemistry B*, vol. 104, no. 6, pp. 1153–1175, 2000.

[7] G. Binnig and H. Rohrer, "Scanning tunneling microscopy," *Surface Science*, vol. 126, no. 1-3, pp. 236–244, 1983.

[8] P. K. Hansma and J. Tersoff, "Scanning tunneling microscopy," *Journal of Applied Physics*, vol. 61, no. 2, R1–R24, 1987.

[9] G. Binnig and H. Rohrer, *Scanning tunneling microscope*, US Patent 4,343,993, 1982.

[10] J. A. Stroscio and W. J. Kaiser, *Scanning Tunneling Microscopy*. Academic Press, 1993, vol. 27.

[11] G. Binnig, C. F. Quate, and C. Gerber, "Atomic force microscope," *Physical Review Letters*, vol. 56, no. 9, p. 930, 1986.

[12] D. Rugar and P. Hansma, "Atomic force microscopy," *Physics Today*, vol. 43, no. 10, pp. 23–30, 1990.

[13] E. Meyer, "Atomic force microscopy," *Progress in Surface Science*, vol. 41, no. 1, pp. 3–49, 1992.

[14] J. Pawley and B. R. Masters, "Handbook of biological confocal microscopy," *Optical Engineering*, vol. 35, no. 9, pp. 2765–2766, 1996.

[15] O. Heimstädt, "Das fluoreszenzmikroskop," *Z Wiss Mikrosk*, vol. 28, pp. 330–337, 1911.

[16] P. Ellinger and A Hirt, "Mikroskopische beobachtungen an lebenden organen mit demonstrationen (intravitalmikroskopie)," *Naunyn-Schmiedeberg's Archives of Pharmacology*, vol. 147, no. 1, pp. 63–63, 1929.

[17] W. W. FRANKE, B. APPELHANS, E. SCHMID, C. FREUDENSTEIN, M. OSBORN, and K. WEBER, "Identification and characterization of epithelial cells in mammalian tissues by immunofluorescence microscopy using antibodies to prekeratin," *Differentiation*, vol. 15, no. 1-3, pp. 7–25, 1979.

[18] B. R. Masters, P. So, and E. Gratton, "Multiphoton excitation fluorescence microscopy and spectroscopy of in vivo human skin.," *Biophysical Journal*, vol. 72, no. 6, p. 2405, 1997.

[19] H Matsumoto, S Kitamura, and T Araki, "Autofluorescence in human dentine in relation to age, tooth type and temperature measured by nanosecond time-resolved fluorescence microscopy," *Archives of Oral Biology*, vol. 44, no. 4, pp. 309–318, 1999.

[20] M. Monici, "Cell and tissue autofluorescence research and diagnostic applications," *Biotechnology Annual Review*, vol. 11, pp. 227–256, 2005.

[21] W. W. Franke, E. Schmid, M. Osborn, and K. Weber, "Different intermediate-sized filaments distinguished by immunofluorescence microscopy," *Proceedings of the National Academy of Sciences of the United States of America*, vol. 75, no. 10, pp. 5034–5038, 1978.

[22] P Kurki, K Ogata, and E. Tan, "Monoclonal antibodies to proliferating cell nuclear antigen (pcna)/cyclin as probes for proliferating cells by immunofluorescence microscopy and flow cytometry," *Journal of Immunological Methods*, vol. 109, no. 1, pp. 49–59, 1988.

[23] M. Osborn, W. W. Franke, and K. Weber, "Visualization of a system of filaments 7-10 nm thick in cultured cells of an epithelioid line (pt k2) by immunofluorescence microscopy," *Proceedings of the National Academy of Sciences of the United States of America*, vol. 74, no. 6, pp. 2490–2494, 1977.

[24] N. C. Shaner, P. A. Steinbach, and R. Y. Tsien, "A guide to choosing fluorescent proteins," *Nature Methods*, vol. 2, no. 12, pp. 905–909, 2005.

[25] A. B. Cubitt, R. Heim, S. R. Adams, A. E. Boyd, L. A. Gross, and R. Y. Tsien, "Understanding, improving and using green fluorescent proteins," *Trends in Biochemical Sciences*, vol. 20, no. 11, pp. 448–455, 1995.

[26] M. Chalfie and S. R. Kain, *Green Fluorescent Protein: Properties, Applications and Protocols*. John Wiley & Sons, 2005, vol. 47.

[27] G. Miesenböck, D. A. De Angelis, and J. E. Rothman, "Visualizing secretion and synaptic transmission with ph-sensitive green fluorescent proteins," *Nature*, vol. 394, no. 6689, pp. 192–195, 1998.

[28] C. S. Smith, N. Joseph, B. Rieger, and K. A. Lidke, "Fast, single-molecule localization that achieves theoretically minimum uncertainty," *Nature Methods*, vol. 7, no. 5, pp. 373–375, 2010.

[29] F. Huang, T. M. Hartwich, F. E. Rivera-Molina, Y. Lin, W. C. Duim, J. J. Long, P. D. Uchil, J. R. Myers, M. A. Baird, W. Mothes, *et al.*, "Video-rate nanoscopy using scmos camera-specific single-molecule localization algorithms," *Nature Methods*, vol. 10, no. 7, pp. 653–658, 2013.

[30] X. Chen, Z. Zeng, R. Li, B. Xue, P. Xi, and Y. Sun, "Superior performance with scmos over emccd in super-resolution optical fluctuation imaging," *Journal of Biomedical Optics*, vol. 21, no. 6, pp. 066 007–066 007, 2016.

[31] M. Born and E. Wolf, *Principles of Optics: Electromagnetic Theory of Propagation, Interference and Diffraction of Light*. Cambridge University Press, 2000.

[32] E. Harrison, "Olbers' paradox," *Nature*, vol. 204, pp. 271–272, 1964.

[33] D. Axelrod, "Total internal reflection fluorescence microscopy in cell biology," *Traffic*, vol. 2, no. 11, pp. 764–774, 2001.

[34] M. M. Falk and U. Lauf, "High resolution, fluorescence deconvolution microscopy and tagging with the autofluorescent tracers cfp, gfp, and yfp to study the structural composition of gap junctions in living cells," *Microscopy Research and Technique*, vol. 52, no. 3, pp. 251–262, 2001.

[35] J. W. Shaevitz and D. A. Fletcher, "Enhanced three-dimensional deconvolution microscopy using a measured depth-varying point-spread function," *Journal of the Optical Society of America A*, vol. 24, no. 9, pp. 2622–2627, 2007.

[36] K. K. McDonald, S. Zharikov, E. R. Block, and M. S. Kilberg, "A caveolar complex between the cationic amino acid transporter 1 and endothelial nitric-oxide synthase may explain the arginine paradox," *Journal of Biological Chemistry*, vol. 272, no. 50, pp. 31 213–31 216, 1997.

[37] A. Iwata, J. C. Christianson, M. Bucci, L. M. Ellerby, N. Nukina, L. S. Forno, and R. R. Kopito, "Increased susceptibility of cytoplasmic over nuclear polyglutamine aggregates to autophagic degradation," *Proceedings of the National Academy of Sciences of the United States of America*, vol. 102, no. 37, pp. 13 135–13 140, 2005.

[38] H. A. Arnett, S. P. Fancy, J. A. Alberta, C. Zhao, S. R. Plant, S. Kaing, C. S. Raine, D. H. Rowitch, R. J. Franklin, and C. D. Stiles, "Bhlh transcription factor olig1 is required to repair demyelinated lesions in the cns," *Science*, vol. 306, no. 5704, pp. 2111–2115, 2004.

[39] J. Mertz, "Optical sectioning microscopy with planar or structured illumination," *Nature Methods*, vol. 8, no. 10, pp. 811–819, 2011.

[40] R. C. Gonzalez and R. E. Woods, "Digital image processing," *Nueva Jersey*, 2008.

[41] M. Broxton, L. Grosenick, S. Yang, N. Cohen, A. Andalman, K. Deisseroth, and M. Levoy, "Wave optics theory and 3-d deconvolution for the light field microscope," *Optics Express*, vol. 21, no. 21, pp. 25 418–25 439, 2013.

[42] D. A. Agard, Y. Hiraoka, and J. W. Sedat, "Three-dimensional microscopy: Image processing for high resolution subcellular imaging," in *33rd Annual Techincal Symposium*, International Society for Optics and Photonics, 1989, pp. 24–30.

[43] P. A. Jansson, *Deconvolution of Images and Spectra*. Courier Corporation, 2014.

[44] R. Gold, "An iterative unfolding method for response matrices," Argonne National Lab., Ill., Tech. Rep., 1964.

[45] J. Yassif, "Quantitative imaging in cell biology," in *Methods in Cell Biology*, T. W. Jennifer Ames, Ed. London: Academic Press, 2012, vol. 123.

[46] J.-B. Sibarita, "Deconvolution microscopy," in *Microscopy Techniques*. Springer, 2005, pp. 201–243.

[47] D. S. Biggs, "3d deconvolution microscopy," *Current Protocols in Cytometry*, pp. 12.19. 1–12.19. 20, 2010.

[48] J. G. McNally, T. Karpova, J. Cooper, and J. A. Conchello, "Three-dimensional imaging by deconvolution microscopy," *Methods*, vol. 19, no. 3, pp. 373–385, 1999.

[49] M. G. Gustafsson, "Surpassing the lateral resolution limit by a factor of two using structured illumination microscopy," *Journal of Microscopy*, vol. 198, no. 2, pp. 82–87, 2000.

[50] M. G. Gustafsson, D. A. Agard, and J. W. Sedat, "Doubling the lateral resolution of wide-field fluorescence microscopy using structured illumination," in *BiOS 2000 The International Symposium on Biomedical Optics*, International Society for Optics and Photonics, 2000, pp. 141–150.

[51] P. Kner, B. B. Chhun, E. R. Griffis, L. Winoto, and M. G. Gustafsson, "Super-resolution video microscopy of live cells by structured illumination," *Nature Methods*, vol. 6, no. 5, pp. 339–342, 2009.

[52] L. Shao, P. Kner, E. H. Rego, and M. G. Gustafsson, "Super-resolution 3d microscopy of live whole cells using structured illumination," *Nature Methods*, vol. 8, no. 12, pp. 1044–1046, 2011.

[53] K. F. Sonnen, L. Schermelleh, H. Leonhardt, and E. A. Nigg, "3d-structured illumination microscopy provides novel insight into architecture of human centrosomes," *Biology Open*, BIO20122337, 2012.

[54] A. G. York, S. H. Parekh, D. Dalle Nogare, R. S. Fischer, K. Temprine, M. Mione, A. B. Chitnis, C. A. Combs, and H. Shroff, "Resolution doubling in live, multicellular organisms via multifocal structured illumination microscopy," *Nature Methods*, vol. 9, no. 7, pp. 749–754, 2012.

[55] L. M. Hirvonen, K. Wicker, O. Mandula, and R. Heintzmann, "Structured illumination microscopy of a living cell," *European Biophysics Journal*, vol. 38, no. 6, pp. 807–812, 2009.

[56] M. G. Gustafsson, L. Shao, P. M. Carlton, C. R. Wang, I. N. Golubovskaya, W. Z. Cande, D. A. Agard, and J. W. Sedat, "Three-dimensional resolution doubling in wide-field fluorescence microscopy by structured illumination," *Biophysical Journal*, vol. 94, no. 12, pp. 4957–4970, 2008.

[57] E. H. Rego, L. Shao, J. J. Macklin, L. Winoto, G. A. Johansson, N. Kamps-Hughes, M. W. Davidson, and M. G. Gustafsson, "Nonlinear structured-illumination microscopy with a photoswitchable protein reveals cellular structures at 50-nm resolution," *Proceedings of the National Academy of Sciences of the United States of America*, vol. 109, no. 3, E135–E143, 2012.

[58] L. Schermelleh, P. M. Carlton, S. Haase, L. Shao, L. Winoto, P. Kner, B. Burke, M. C. Cardoso, D. A. Agard, M. G. Gustafsson, *et al.*, "Subdiffraction multicolor imaging of the nuclear periphery with 3d structured illumination microscopy," *Science*, vol. 320, no. 5881, pp. 1332–1336, 2008.

[59] M. G. Gustafsson, "Nonlinear structured-illumination microscopy: Wide-field fluorescence imaging with theoretically unlimited resolution," *Proceedings of the Na-*

tional Academy of Sciences of the United States of America, vol. 102, no. 37, pp. 13 081–13 086, 2005.

[60] X. Yang, Y.-K. Tzeng, Z. Zhu, Z. Huang, X. Chen, Y. Liu, H.-C. Chang, L. Huang, W.-D. Li, and P. Xi, "Sub-diffraction imaging of nitrogen-vacancy centers in diamond by stimulated emission depletion and structured illumination," *Rsc Advances*, vol. 4, no. 22, pp. 11 305–11 310, 2014.

[61] M. Minsky, "Memoir on inventing the confocal scanning microscope," *Scanning*, vol. 10, no. 4, pp. 128–138, 1988.

[62] R. H. Webb, "Confocal optical microscopy," *Reports on Progress in Physics*, vol. 59, no. 3, p. 427, 1996.

[63] W. Amos and J. White, "How the confocal laser scanning microscope entered biological research," *Biology of the Cell*, vol. 95, no. 6, pp. 335–342, 2003.

[64] M. Rajadhyaksha, M. Grossman, D. Esterowitz, R. H. Webb, and R. R. Anderson, "In vivo confocal scanning laser microscopy of human skin: Melanin provides strong contrast," *Journal of Investigative Dermatology*, vol. 104, no. 6, pp. 946–952, 1995.

[65] R. Kiesslich, J. Burg, M. Vieth, J. Gnaendiger, M. Enders, P. Delaney, A. Polglase, W. McLaren, D. Janell, S. Thomas, *et al.*, "Confocal laser endoscopy for diagnosing intraepithelial neoplasias and colorectal cancer in vivo," *Gastroenterology*, vol. 127, no. 3, pp. 706–713, 2004.

[66] J. Korlach, P. Schwille, W. W. Webb, and G. W. Feigenson, "Characterization of lipid bilayer phases by confocal microscopy and fluorescence correlation spectroscopy," *Proceedings of the National Academy of Sciences of the United States of America*, vol. 96, no. 15, pp. 8461–8466, 1999.

[67] H. D. Cavanagh, W. M. Petroll, H. Alizadeh, Y.-G. He, J. P. McCulley, and J. V. Jester, "Clinical and diagnostic use of in vivo confocal microscopy in patients with corneal disease," *Ophthalmology*, vol. 100, no. 10, pp. 1444–1454, 1993.

[68] M. Rajadhyaksha, S. González, J. M. Zavislan, R. R. Anderson, and R. H. Webb, "In vivo confocal scanning laser microscopy of human skin ii: Advances in instrumentation and comparison with histology," *Journal of Investigative Dermatology*, vol. 113, no. 3, pp. 293–303, 1999.

[69] C. B. Müller and J. Enderlein, "Image scanning microscopy," *Physical Review Letters*, vol. 104, no. 19, p. 198 101, 2010.

[70] C. J. Sheppard, S. B. Mehta, and R. Heintzmann, "Superresolution by image scanning microscopy using pixel reassignment," *Optics Letters*, vol. 38, no. 15, pp. 2889–2892, 2013.

[71] O. Schulz, C. Pieper, M. Clever, J. Pfaff, A. Ruhlandt, R. H. Kehlenbach, F. S. Wouters, J. Großhans, G. Bunt, and J. Enderlein, "Resolution doubling in fluorescence microscopy with confocal spinning-disk image scanning microscopy," *Proceedings of the National Academy of Sciences of the United States of America*, vol. 110, no. 52, pp. 21 000–21 005, 2013.

[72] M. Ingaramo, A. G. York, P. Wawrzusin, O. Milberg, A. Hong, R. Weigert, H. Shroff, and G. H. Patterson, "Two-photon excitation improves multifocal structured illumination microscopy in thick scattering tissue," *Proceedings of the National Academy of Sciences of the United States of America*, vol. 111, no. 14, pp. 5254–5259, 2014.

[73] S. W. Hell and J. Wichmann, "Breaking the diffraction resolution limit by stimulated emission: Stimulated-emission-depletion fluorescence microscopy," *Optics Letters*, vol. 19, no. 11, pp. 780–782, 1994.

[74] S. W. Hell, "Far-field optical nanoscopy," *Science*, vol. 316, no. 5828, pp. 1153–1158, 2007.

[75] X. Hao, C. Kuang, Z. Gu, Y. Wang, S. Li, Y. Ku, Y. Li, J. Ge, and X. Liu, "From microscopy to nanoscopy via visible light," *Light: Science & Applications*, vol. 2, no. 10, e108, 2013.

[76] S. W. Hell, "Toward fluorescence nanoscopy," *Nature Biotechnology*, vol. 21, no. 11, pp. 1347–1355, 2003.

[77] R. Schmidt, C. A. Wurm, S. Jakobs, J. Engelhardt, A. Egner, and S. W. Hell, "Spherical nanosized focal spot unravels the interior of cells," *Nature Methods*, vol. 5, no. 6, pp. 539–544, 2008.

[78] K. Y. Han, S. K. Kim, C. Eggeling, and S. W. Hell, "Metastable dark states enable ground state depletion microscopy of nitrogen vacancy centers in diamond with diffraction-unlimited resolution," *Nano Letters*, vol. 10, no. 8, pp. 3199–3203, 2010.

[79] A. Chmyrov, J. Keller, T. Grotjohann, M. Ratz, E. d'Este, S. Jakobs, C. Eggeling, and S. W. Hell, "Nanoscopy with more than 100,000'doughnuts'," *Nature Methods*, vol. 10, no. 8, pp. 737–740, 2013.

[80] I. Testa, N. T. Urban, S. Jakobs, C. Eggeling, K. I. Willig, and S. W. Hell, "Nanoscopy of living brain slices with low light levels," *Neuron*, vol. 75, no. 6, pp. 992–1000, 2012.

[81] S.-J. Yu, M.-W. Kang, H.-C. Chang, K.-M. Chen, and Y.-C. Yu, "Bright fluorescent nanodiamonds: No photobleaching and low cytotoxicity," *Journal of the American Chemical Society*, vol. 127, no. 50, pp. 17 604–17 605, 2005.

[82] J. Huisken and D. Y. Stainier, "Selective plane illumination microscopy techniques in developmental biology," *Development*, vol. 136, no. 12, pp. 1963–1975, 2009.

[83] J. Huisken, J. Swoger, F. Del Bene, J. Wittbrodt, and E. H. Stelzer, "Optical sectioning deep inside live embryos by selective plane illumination microscopy," *Science*, vol. 305, no. 5686, pp. 1007–1009, 2004.

[84] F. C. Zanacchi, Z. Lavagnino, M. P. Donnorso, A. Del Bue, L. Furia, M. Faretta, and A. Diaspro, "Live-cell 3d super-resolution imaging in thick biological samples," *Nature Methods*, vol. 8, no. 12, pp. 1047–1049, 2011.

[85] J. C. M. Gebhardt, D. M. Suter, R. Roy, Z. W. Zhao, A. R. Chapman, S. Basu, T. Maniatis, and X. S. Xie, "Single-molecule imaging of transcription factor binding to dna in live mammalian cells," *Nature Methods*, vol. 10, no. 5, pp. 421–426, 2013.

[86] P. J. Keller, A. D. Schmidt, A. Santella, K. Khairy, Z. Bao, J. Wittbrodt, and E. H. Stelzer, "Fast, high-contrast imaging of animal development with scanned light sheet-based structured-illumination microscopy," *Nature Methods*, vol. 7, no. 8, pp. 637–642, 2010.

[87] J. Palero, S. I. Santos, D. Artigas, and P. Loza-Alvarez, "A simple scanless two-photon fluorescence microscope using selective plane illumination," *Optics Express*, vol. 18, no. 8, pp. 8491–8498, 2010.

[88] Y. S. Hu, Q. Zhu, K. Elkins, K. Tse, Y. Li, J. A. Fitzpatrick, I. M. Verma, and H. Cang, "Light-sheet bayesian microscopy enables deep-cell super-resolution imaging of heterochromatin in live human embryonic stem cells," *Optical Nanoscopy*, vol. 2, no. 1, p. 1, 2013.

[89] T. Vettenburg, H. I. Dalgarno, J. Nylk, C. Coll-Lladó, D. E. Ferrier, T. Čižmár, F. J. Gunn-Moore, and K. Dholakia, "Light-sheet microscopy using an airy beam," *Nature Methods*, vol. 11, no. 5, pp. 541–544, 2014.

[90] M. B. Ahrens, M. B. Orger, D. N. Robson, J. M. Li, and P. J. Keller, "Whole-brain functional imaging at cellular resolution using light-sheet microscopy," *Nature Methods*, vol. 10, no. 5, pp. 413–420, 2013.

[91] J. Jackson, *Classical Electrodynamics*. Wiley, 2007, ISBN: 9788126510948.

[92] M. Gu, *Advanced Pptical Imaging Theory*. Springer Science & Business Media, 2000, vol. 75.

[93] J. W. Goodman, *Introduction to Fourier optics*. Roberts and Company Publishers, 2005.

[94] B Richards and E Wolf, "Electromagnetic diffraction in optical systems. ii. structure of the image field in an aplanatic system," in *Proceedings of the Royal Society of London A: Mathematical, Physical and Engineering Sciences*, vol. 253, The Royal Society, 1959, pp. 358–379.

[95] E. Wolf, "Electromagnetic diffraction in optical systems. i. an integral representation of the image field," in *Proceedings of the Royal Society of London A: Mathematical, Physical and Engineering Sciences*, vol. 253, The Royal Society, 1959, pp. 349–357.

[96] H. Xie, Y. Liu, D. Jin, P. J. Santangelo, and P. Xi, "Analytical description of high-aperture sted resolution with 0c2 vortex phase modulation," *Journal of the Optical Society of America A*, vol. 30, no. 8, pp. 1640–1645, 2013.

[97] J. Keller, A. Sch, and S. W. Hell, "Efficient fluorescence inhibition patterns for resolft microscopy," *Optics Express*, vol. 15, no. 6, pp. 3361–3371, 2007.

[98] S. Deng, L. Liu, Y. Cheng, R. Li, and Z. Xu, "Effects of primary aberrations on the fluorescence depletion patterns of sted microscopy," *Optics Express*, vol. 18, no. 2, pp. 1657–1666, 2010.

[99] H. Voort and G. Brakenhoff, "3d image formation in high aperture fluorescence confocal microscopy: A numerical analysis," *Journal of Microscopy*, vol. 158, no. 1, pp. 43–54, 1990.

[100] K. I. Willig, B. Harke, R. Medda, and S. W. Hell, "Sted microscopy with continuous wave beams," *Nature Methods*, vol. 4, no. 11, pp. 915–918, 2007.

[101] B. Harke, J. Keller, C. K. Ullal, V. Westphal, A. Sch, and S. W. Hell, "Resolution scaling in sted microscopy," *Optics Express*, vol. 16, no. 6, pp. 4154–4162, 2008.

[102] S. Hell and E. H. Stelzer, "Properties of a 4pi confocal fluorescence microscope," *Journal of the Optical Society of America A*, vol. 9, no. 12, pp. 2159–2166, 1992.

[103] A. D. Rakić, A. B. Djurišić, J. M. Elazar, and M. L. Majewski, "Optical properties of metallic films for vertical-cavity optoelectronic devices," *Applied Optics*, vol. 37, no. 22, pp. 5271–5283, 1998.

[104] M. N. Polyanskiy, *Refractive index database*, `https://refractiveindex.info`, Accessed on 2016-04-01.

[105] X. Yang, H. Xie, E. Alonas, Y. Liu, X. Chen, P. J. Santangelo, Q. Ren, P. Xi, and D. Jin, "Mirror-enhanced super-resolution microscopy," *Light: Science & Applications*, vol. 5, no. 6, e16134, 2016.

[106] M. Orrit, "Nobel prize in chemistry: Celebrating optical nanoscopy," *Nature Photonics*, vol. 8, pp. 887–888, 2014.

[107] B. Bailey, D. L. Farkas, D. L. Taylor, and F. Lanni, "Enhancement of axial resolution in fluorescence microscopy by standing-wave excitation," *Nature*, vol. 366, no. 6450, pp. 44–48, 1993.

[108] A. K. Swan, L. A. Moiseev, C. Cantor, B. Davis, S. Ippolito, W. C. Karl, B. B. Goldberg, and M. Unlu, "Toward nanometer-scale resolution in fluorescence microscopy using spectral self-interference," *IEEE Journal of Selected Topics in Quantum Electronics*, vol. 9, no. 2, pp. 294–300, 2003.

[109] R. Amor, S. Mahajan, W. B. Amos, and G. McConnell, "Standing-wave-excited multiplanar fluorescence in a laser scanning microscope reveals 3d information on red blood cells," *Scientific Reports*, vol. 4, 2014.

[110] E. Mudry, E. Le Moal, P. Ferrand, P. C. Chaumet, and A. Sentenac, "Isotropic diffraction-limited focusing using a single objective lens," *Physical Review Letters*, vol. 105, no. 20, p. 203 903, 2010.

[111] T. Deguchi, S. Koho, T. Näreoja, and P. Hänninen, "Axial super-resolution by mirror-reflected stimulated emission depletion microscopy," *Optical Review*, vol. 21, no. 3, pp. 389–394, 2014.

[112] K. Elsayad, A. Urich, P. S. Tan, M. Nemethova, J. V. Small, K. Unterrainer, and K. G. Heinze, "Spectrally coded optical nanosectioning (specon) with biocompatible metalcdielectric-coated substrates," *Proceedings of the National Academy of Sciences of the United States of America*, vol. 110, no. 50, pp. 20 069–20 074, 2013.

[113] A. I. Chizhik, J. Rother, I. Gregor, A. Janshoff, and J. Enderlein, "Metal-induced energy transfer for live cell nanoscopy," *Nature Photonics*, vol. 8, no. 2, pp. 124–127, 2014.

[114] R. Rygiel, *Device and method for adjusting two objective lenses in 4pi-system*, US Patent 7,477,448, 2009.

[115] M. G. Gustafsson, D. A. Agard, and J. W. Sedat, "Sevenfold improvement of axial resolution in 3d wide-field microscopy using two objective lenses," in *IS&T/SPIE's*

Symposium on Electronic Imaging: Science & Technology, International Society for Optics and Photonics, 1995, pp. 147–156.

[116] J Bewersdorf, R Schmidt, and S. Hell, "Comparison of i5m and 4pi-microscopy," *Journal of Microscopy*, vol. 222, no. 2, pp. 105–117, 2006.

[117] L Moiseev, C. Cantor, M. Aksun, M Dogan, B. Goldberg, A. Swan, and M. Ünlü, "Spectral self-interference fluorescence microscopy," *Journal of Applied Physics*, vol. 96, no. 9, pp. 5311–5315, 2004.

[118] L. Moiseev, M. S. Ünlü, A. K. Swan, B. B. Goldberg, and C. R. Cantor, "Dna conformation on surfaces measured by fluorescence self-interference," *Proceedings of the National Academy of Sciences of the United States of America*, vol. 103, no. 8, pp. 2623–2628, 2006.

[119] D Wildanger, R Medda, L Kastrup, and S. Hell, "A compact sted microscope providing 3d nanoscale resolution," *Journal of Microscopy*, vol. 236, no. 1, pp. 35–43, 2009.

[120] D. O. Meredith, L. Eschbach, M. O. Riehle, A. S. Curtis, and R. G. Richards, "Microtopography of metal surfaces influence fibroblast growth by modifying cell shape, cytoskeleton, and adhesion," *Journal of Orthopaedic Research*, vol. 25, no. 11, pp. 1523–1533, 2007.

[121] C. A. Wurm, D. Neumann, R. Schmidt, A. Egner, and S. Jakobs, "Sample preparation for sted microscopy," *Live Cell Imaging: Methods and Protocols*, pp. 185–199, 2010.

[122] G. Vicidomini, G. Moneron, K. Y. Han, V. Westphal, H. Ta, M. Reuss, J. Engelhardt, C. Eggeling, and S. W. Hell, "Sharper low-power sted nanoscopy by time gating," *Nature Methods*, vol. 8, no. 7, pp. 571–573, 2011.

[123] V. Westphal and S. W. Hell, "Nanoscale resolution in the focal plane of an optical microscope," *Physical Review Letters*, vol. 94, no. 14, p. 143 903, 2005.

[124] T Guan, S Mller, G Klier, N Pante, J. Blevitt, M Haner, B Paschal, U Aebi, and L Gerace, "Structural analysis of the p62 complex, an assembly of o-linked glycoproteins that localizes near the central gated channel of the nuclear pore complex," *Molecular Biology of the Cell*, vol. 6, no. 11, pp. 1591–1603, 1995.

[125] K. Fujita, M. Kobayashi, S. Kawano, M. Yamanaka, and S. Kawata, "High-resolution confocal microscopy by saturated excitation of fluorescence," *Physical Review Letters*, vol. 99, no. 22, p. 228 105, 2007.

[126] Z. Gan, Y. Cao, R. A. Evans, and M. Gu, "Three-dimensional deep sub-diffraction optical beam lithography with 9 nm feature size," *Nature Communications*, vol. 4, 2013.

[127] R. Kolesov, R. Reuter, K. Xia, R. Stöhr, A. Zappe, and J. Wrachtrup, "Super-resolution upconversion microscopy of praseodymium-doped yttrium aluminum garnet nanoparticles," *Physical Review B*, vol. 84, no. 15, p. 153 413, 2011.

[128] X. Chen, C. Zou, Z. Gong, C. Dong, G. Guo, and F. Sun, "Subdiffraction optical manipulation of the charge state of nitrogen vacancy center in diamond," *Light: Science & Applications*, vol. 4, no. 1, e230, 2015.

[129] J Schnitzbauer, R McGorty, and B Huang, "4pi fluorescence detection and 3d particle localization with a single objective," *Optics Express*, vol. 21, no. 17, pp. 19 701–19 708, 2013.

[130] H. Xie, D. Jin, J. Yu, T. Peng, Y. Ding, C. Zhou, and P. Xi, "Schlieren confocal microscopy for phase-relief imaging," *Optics Letters*, vol. 39, no. 5, pp. 1238–1241, 2014.

[131] J. G. Dodd, "Interferometry with schlieren microscopy," *Applied Optics*, vol. 16, no. 2, pp. 470–472, 1977.

[132] D. Axelrod, "Zero-cost modification of bright field microscopes for imaging phase gradient on cells: Schlieren optics," *Cell Biophysics*, vol. 3, no. 2, pp. 167–173, 1981.

[133] R. Yi, K. K. Chu, and J. Mertz, "Graded-field microscopy with white light," *Optics Express*, vol. 14, no. 12, pp. 5191–5200, 2006.

[134] F. Zernike, "Phase contrast, a new method for the microscopic observation of transparent objects," *Physica*, vol. 9, no. 7, pp. 686–698, 1942.

[135] M. W. Davidson and M. Abramowitz, "Optical microscopy," *Encyclopedia of Imaging Science and Technology*, 2002.

[136] G Nomarski, "Differential microinterferometer with polarized waves," *J. Phys. Radium*, vol. 16, no. 9, 9S–11S, 1955.

[137] C. Preza, D. L. Snyder, and J.-A. Conchello, "Theoretical development and experimental evaluation of imaging models for differential-interference-contrast microscopy," *Journal of the Optical Society of America A*, vol. 16, no. 9, pp. 2185–2199, 1999.

[138] C. J. Cogswell and C. Sheppard, "Confocal differential interference contrast (dic) microscopy: Including a theoretical analysis of conventional and confocal dic imaging," *Journal of Microscopy*, vol. 165, no. 1, pp. 81–101, 1992.

[139] G. Popescu, T. Ikeda, R. R. Dasari, and M. S. Feld, "Diffraction phase microscopy for quantifying cell structure and dynamics," *Optics Letters*, vol. 31, no. 6, pp. 775–777, 2006.

[140] S. Fürhapter, A. Jesacher, S. Bernet, and M. Ritsch-Marte, "Spiral phase contrast imaging in microscopy," *Optics Express*, vol. 13, no. 3, pp. 689–694, 2005.

[141] T. Wilson and C. Sheppard, *Theory and Practice of Scanning Optical Microscopy*. London: Academic Press, 1984, vol. 180.

[142] J Beuthan, O Minet, J Helfmann, M Herrig, and G Mller, "The spatial variation of the refractive index in biological cells," *Physics in Medicine and Biology*, vol. 41, no. 3, p. 369, 1996.

[143] Y. Ding, H. Xie, T. Peng, Y. Lu, D. Jin, J. Teng, Q. Ren, and P. Xi, "Laser oblique scanning optical microscopy (losom) for phase relief imaging," *Optics Express*, vol. 20, no. 13, pp. 14 100–14 108, 2012.

[144] Y. Ding, Y. Zhang, T. Peng, Y. Lu, D. Jin, Q. Ren, Y. Liu, J. Han, and P. Xi, "Observation of mesenteric microcirculatory disturbance in rat by laser oblique scanning optical microscopy," *Scientific Reports*, vol. 3, p. 1762, 2013.

[145] M. Levoy, R. Ng, A. Adams, M. Footer, and M. Horowitz, "Light field microscopy," *ACM Transactions on Graphics (TOG)*, vol. 25, no. 3, pp. 924–934, 2006.

[146] R. Prevedel, Y.-G. Yoon, M. Hoffmann, N. Pak, G. Wetzstein, S. Kato, T. Schrödel, R. Raskar, M. Zimmer, E. S. Boyden, *et al.*, "Simultaneous whole-animal 3d imaging of neuronal activity using light-field microscopy," *Nature Methods*, vol. 11, no. 7, pp. 727–730, 2014.

[147] X. Lin, J. Wu, G. Zheng, and Q. Dai, "Camera array based light field microscopy," *Biomedical Optics Express*, vol. 6, no. 9, pp. 3179–3189, 2015.

[148] X. Lin, Y. Liu, J. Wu, and Q. Dai, "Spatial-spectral encoded compressive hyperspectral imaging," *ACM Transactions on Graphics (TOG)*, vol. 33, no. 6, p. 233, 2014.

[149] Z. Zhang, "A practical introduction to light field microscopy," pp. 01–15, 2010.

[150] R. Ng, M. Levoy, M. Brédif, G. Duval, M. Horowitz, and P. Hanrahan, "Light field photography with a hand-held plenoptic camera," *Computer Science Technical Report CSTR*, vol. 2, no. 11, pp. 1–11, 2005.

[151] R. Ng, "Digital light field photography," PhD thesis, stanford university, 2006.

[152] E. J. Botcherby, R Juškaitis, M. J. Booth, and T. Wilson, "An optical technique for remote focusing in microscopy," *Optics Communications*, vol. 281, no. 4, pp. 880–887, 2008.

[153] N. Stuurman, N. Amdodaj, and R. Vale, "Micro-manager: Open source software for light microscope imaging," *Microscopy Today*, vol. 15, no. 3, pp. 42–43, 2007.

[154] J. G. Ritter, J.-H. Spille, T. Kaminski, and U. Kubitscheck, "A cylindrical zoom lens unit for adjustable optical sectioning in light sheet microscopy," *Biomedical Optics Express*, vol. 2, no. 1, pp. 185–193, 2011.

[155] K. K. Chu and J. Mertz, "Single-exposure complementary aperture phase microscopy with polarization encoding," *Optics Letters*, vol. 37, no. 18, pp. 3798–3800, 2012.

[156] M. Leutenegger, C. Eggeling, and S. W. Hell, "Analytical description of sted microscopy performance," *Optics Express*, vol. 18, no. 25, pp. 26 417–26 429, 2010.

[157] G. Donnert, J. Keller, R. Medda, M. A. Andrei, S. O. Rizzoli, R. Lhrmann, R. Jahn, C. Eggeling, and S. W. Hell, "Macromolecular-scale resolution in biological fluorescence microscopy," *Proceedings of the National Academy of Sciences of the United States of America*, vol. 103, no. 31, pp. 11 440–11 445, 2006.

[158] T. Watanabe, Y. Igasaki, N. Fukuchi, M. Sakai, S.-i. Ishiuchi, M. Fujii, T. Omatsu, K. Yamamoto, and Y. Iketaki, "Formation of a doughnut laser beam for super-resolving microscopy using a phase spatial light modulator," *Optical Engineering*, vol. 43, no. 5, pp. 1136–1143, 2004.

[159] E. Rittweger, K. Y. Han, S. E. Irvine, C. Eggeling, and S. W. Hell, "Sted microscopy reveals crystal colour centres with nanometric resolution," *Nature Photonics*, vol. 3, no. 3, pp. 144–147, 2009.

VITA

Hao Xie was born in Hangzhou, China, on October 15th, 1988. After completing his work at Xuejun High School, Hanghozu, China, he entered Peking University in Beijing, China. In May of 2011 he completed a Bachelor of Science in Physics and a double Bachelor of Science in Mathematics. In September, 2011, he entered The Graduate School at Peking University. In August, 2012, he was enrolled in the Georgia Tech / Emory / Peking University BME Ph.D. Program.